8-23-2013 12:00 AM

Capacity Assessment of a Transmission Tower under Wind Loading

Thomas G. Mara
The University of Western Ontario

Supervisor
Dr. H.P. Hong
The University of Western Ontario

Graduate Program in Civil and Environmental Engineering
A thesis submitted in partial fulfillment of the requirements for the degree in Doctor of Philosophy

CAPACITY ASSESSMENT OF A TRANSMISSION TOWER UNDER WIND LOADING

(Thesis format: Integrated Article)

by

Thomas Goodwin Mara

Graduate Program in Civil and Environmental Engineering

A thesis submitted in partial fulfillment
of the requirements for the degree of
Doctor of Philosophy

The School of Graduate and Postdoctoral Studies
The University of Western Ontario
London, Ontario, Canada

Abstract

Transmission towers play a vital role in power distribution networks and are often subject to strong wind loads. Lattice tower design is often based on a linear elastic response to wind loading using methodology derived for atmospheric boundary layer (ABL) winds. A number of failures have been attributed to high intensity wind (HIW) events such as downbursts and tornadoes. This thesis investigates extreme winds on a self-supported lattice transmission tower and ultimately makes comparisons of the capacity under ABL and HIW. The force-deformation relation between the base shear and the displacement of the tip of the tower are used to represent the capacity curve of a structure under wind loading.

Wind tunnel testing is used to evaluate the aerodynamic behaviour of a typical tower cross-arm section, which serves as the basis for selection of wind loading expressions for the numerical model. Recommendations are made for further investigation of lattice aerodynamics, including a more robust definition of the drag coefficient. Capacity estimates obtained using the incremental dynamic analysis (IDA) and nonlinear static pushover (NSP) procedures are compared, which indicate good agreement for ABL winds. The analyses consider both geometric and material nonlinearity. The NSP analysis is used to estimate the capacity of the tower under various wind profiles for the transverse and longitudinal wind directions, and it is shown that the capacity curve obtained under typical downburst scenarios can be approximately enveloped by those obtained under rectangular and ABL wind profiles. An uncertainty propagation analysis is carried out using the simple Monte Carlo technique, which shows that the coefficient of variation of the tower capacity is small compared to that associated with extreme wind load effects. Oblique wind directions are considered for ABL, rectangular and downburst wind loading, which associate critical wind speeds with direction. The resulting capacity curves are used to develop the capacity surface of the tower. It is shown that a conservative approximation of the tower capacity curve, or surface, under downburst wind is made if a fully correlated ABL wind loading profile is used as the wind load distribution.

Keywords

Electric transmission structures, lattice towers, nonlinear analysis, capacity curve, inelastic system, downburst, wind forces, wind tunnel testing.

Co-Authorship Statement

This thesis has been prepared in Integrated Article format as specified by the School of Graduate and Post-doctoral Studies at the University of Western Ontario. Statements regarding the co-authorship of individual chapters are as follows:

Chapter 2: Experimental investigation of lattice section aerodynamics

All wind tunnel experiments were designed and carried out by T.G. Mara; the experiments involving the cross-arm section were carried out with the guidance of J.K. Galsworthy. The manuscripts comprising Chapter 2 were prepared by T.G. Mara. A paper co-authored by T.G. Mara and J.K. Galsworthy, which discusses the aerodynamics of cross-arm sections, will be submitted for potential publication in a peer-reviewed journal. A second paper, authored by T.G. Mara, which discusses the relationship between the drag coefficient and solidity ratio of lattice frames, has been accepted to the Journal of Engineering Mechanics.

Chapter 3: Comparison of capacity assessment methods for a lattice transmission tower

A numerical model of the tower was initially developed by C.-S. Lee; significant changes to the components, loading and output of the tower model were implemented by T.G. Mara. Analysis and interpretation was carried out by T.G. Mara under the supervision of H.P. Hong. The manuscript for Chapter 3 was prepared by T.G. Mara and modifications were completed under the supervision of H.P. Hong.

Chapter 4: Capacity of a transmission tower under ABL and downburst wind loading

Analysis and interpretation was carried out by T.G. Mara. Each component of this chapter was completed under the supervision of H.P. Hong, with input from T.C.E. Ho. The manuscript for Chapter 4 was prepared by T.G. Mara and modifications were completed under the supervision of H.P. Hong, and with the input of C.-S. Lee and T.C.E. Ho. A paper co-authored by T.G. Mara, H.P. Hong, C.-S. Lee and T.C.E. Ho has been submitted for potential publication in a peer-reviewed journal.

Chapter 5: Effect of relative orientation on the capacity of a transmission tower under downburst loading

Analysis and interpretation was carried out by T.G. Mara under the supervision of H.P. Hong. The manuscript for Chapter 5 was prepared by T.G. Mara and modifications were completed under the supervision of H.P. Hong. A paper co-authored by T.G. Mara and H.P. Hong is included in the Proceedings of the 3rd Specialty Conference on Disaster Prevention and Mitigation, 2013 CSCE Annual Conference.

Chapter 6: Effect of wind direction on the response and capacity surface of a transmission tower

Analysis and interpretation was carried out by T.G. Mara under the supervision of H.P. Hong. The manuscript for Chapter 6 was prepared by T.G. Mara and modifications were completed under the supervision of H.P. Hong. A paper co-authored by T.G. Mara and H.P. Hong has been submitted for potential publication in a peer-reviewed journal.

Acknowledgments

First and foremost, I would like to thank Dr. H.P. Hong, who has acted as a supervisor for this work as well as a mentor in the field of academia. His guidance, advice and patience throughout the completion of this thesis, as well as other endeavors, is much appreciated, and I am grateful to him for providing the opportunity to work on a variety of interesting engineering projects.

During my time at Western I have been lucky enough to be surrounded by great friends, colleagues, collaborators, and mentors. It would be near to impossible to compile a complete list of these important people in my life, but as I reflect on the previous four years, some names are worth particular mention. Dr. Eric Ho has acted as a mentor in the field of wind engineering for many years now, and I am grateful to him for discussion on research ideas, reading and offering feedback on my work, and providing the opportunity to get involved in various projects. The crew at the BLWTL, particularly Darren Garnham, Peter Case, Steve Farquhar, Gerry Dafoe and Anthony Burggraaf have assisted in various parts of my experimental work, in addition to being great friends. Conversations with Dr. Nicholas Isyumov, Dr. Jon Galsworthy and Dr. Barry Vickery have greatly contributed to my approach to research, and I am grateful for their input and willingness to get involved in various aspects of my work. Lastly, I'd like to acknowledge Dr. David Gatey for many great conversations on wind and everything else, whether over a coffee or single malt.

The financial support from the National Sciences and Engineering Research Council of Canada (NSERC) is gratefully acknowledged for supporting me personally, as well as a number of the projects with which I have been involved. I also acknowledge the financial support received from the University of Western Ontario throughout the duration of my program.

Finally, I am extremely thankful to my family for providing the moral (and occasionally financial) support to complete this degree. Their unwavering support throughout my life has been extraordinary, and I am grateful that they have provided the opportunity and means to pursue something I am passionate about.

Dedication

To my parents, who always instilled the freedom of learning and value of education.

Table of Contents

List of Tables

List of Figures

Nomenclature

The nomenclature used throughout the thesis is listed by chapter as follows (code specific values for Chapter 2 are indicated in parenthesis):

Chapter 2

A_{gross}	gross area of a lattice frame
A_{ml}	net area of the longitudinal face (ASCE-74)
A_{mt}	net area of the transverse face (ASCE-74)
A_{net}	net area of a lattice frame
A_p	projected area of a frame subject to wind load
A_t	total wind loading on the panel in the direction of the wind (N) (IEC-2003)
B	arbitrary constant ($B = \gamma_w Q K_z K_{zt} V^2 G_{t1}$) (ASCE-74)
C_d	drag coefficient of a lattice frame
C_{fl}	drag coefficient of the longitudinal face (ASCE-74)
C_{ft}	drag coefficient of the transverse face (ASCE-74)
C_{xt1}	drag coefficient of face 1 (IEC-2003)
C_{xt2}	drag coefficient of face 2 (IEC-2003)
D	arbitrary constant (D = $q_o G_{t2}$) (IEC-2003)
F_d	drag wind load
F_d'	vector resultant wind force (ASCE-74)
F_l	longitudinal wind force (ASCE-74)
F_l'	longitudinal component of vector resultant wind force (ASCE-74)
F_t	transverse wind force (ASCE-74)
F_t'	transverse component of vector resultant wind force (ASCE-74)
$F_L(\psi)$	longitudinal wind force at yaw angle ψ
$F_T(\psi)$	transverse wind force at yaw angle ψ
G_{t1}	gust response factor for the tower (ASCE-74)
G_{t2}	combined wind factor (IEC-2003)
K_z	wind pressure exposure factor (ASCE-74)
K_{zt}	wind pressure topographic factor (ASCE-74)
Q	numerical constant (ASCE-74)
S_{t1}	net member area of face 1 (IEC-2003)

S_{t2}	net member area of face 2 (IEC-2003)
V	wind speed at the height of a frame or panel
q_o	dynamic wind pressure at reference height (IEC-2003)
ϕ	solidity ratio of a lattice frame
θ	yaw angle of wind (measured from transverse face) (IEC-2003)
ρ	density of air
ψ	yaw angle of wind (measured from the transverse face) (ASCE-74)
γ_w	importance factor for wind load (ASCE-74)
C_dA_p	effective drag of a lattice frame (m^2)

Chapter 3

A_t	total wind loading on the panel in the direction of the wind (N)
A_c	total load on the line (N)
C_d	drag coefficient of a section
C_{xc}	drag coefficient of the line
C_{xti}	drag coefficient for the corresponding *i*-th face
C_z	exponential decay coefficient
$Co(z_i, z_j, f)$	Davenport coherence function
$F(z,t)$	fluctuating drag force at height *z* and time *t*
G_L	span factor based on the length of the span
G_c	combined wind factor for the line
G_t	combined wind factor for the tower panel
$I(z)$	longitudinal turbulence intensity at height *z*
L	wind span of the wires (m)
$S(f)$	power spectral density function of longitudinal turbulence (Kaimal)
$\overline{V_{10\mathrm{m}}}$	mean wind speed at 10 m height
$\overline{V(z)}$	mean wind speed at height *z*
V_{ref}	arbitrary reference mean wind speed
d	diameter of the line (m)
f	frequency of longitudinal turbulence (Hz)
Δt	time interval for ARMA algorithm
$v(z,t)$	fluctuating wind speed at height *z* and time *t*

Ω	angle between the wind direction and the wires
α	power law coefficient
β_i	moving average (MA) coefficient with order p
γ_i	autoregressive (AR) coefficient with order q
μ	density of air
$\kappa(z,t)$	normalized fluctuating wind speed (zero mean, unit variance)
θ	yaw angle of wind (measured from transverse direction)
ρ	density of air
τ	air density correction factor

Chapter 4

A_t	total wind loading on the panel in the direction of the wind (N)
A_c	total load on the line (N)
C_{xc}	drag coefficient of the line
C_{xti}	drag coefficient for the corresponding *i*-th face
D_{jet}	jet diameter of simulated downburst (m)
G_L	span factor based on the length of the span
G_c	combined wind factor for the line
G_t	combined wind factor for the tower panel
L	wind span of the wires (m)
V_{jet}	jet velocity of simulated downburst (m/s)
V_R	reference wind speed
$V_{3s,10m}$	3-second gust wind speed at height of 10 m
$V_{10\text{-min},10m}$	10-minute mean wind speed at height of 10 m
V_{hor}	horizontal wind speed resulting from downburst
d	diameter of the line (m)
r	distance from downburst to point of interest
t_s	downburst simulation time scale parameter
Ω	angle between the wind direction and the wires
α	power law coefficient
μ	density of air
θ	yaw angle of wind (measured from transverse direction)

τ	air density correction factor

Chapter 5

A_t	total wind loading on the panel in the direction of the wind (N)
A_c	total load on the line (N)
C_{xc}	drag coefficient of the line
C_{xti}	drag coefficient for the corresponding *i*-th face
D_{jet}	jet diameter of simulated downburst (m)
G_L	span factor based on the length of the span
G_c	combined wind factor for the line
G_t	combined wind factor for the tower panel
L	wind span of the wires (m)
S_{ti}	total surface area projected normally on the corresponding *i*-th face (m^2)
V_{hor}	horizontal wind speed resulting from downburst
V_{jet}	jet velocity of simulated downburst (m/s)
V_R	reference wind speed
d	diameter of the line (m)
i	any point along conductor span between towers
r	distance from downburst to point of interest
Ω	angle between the wind direction and the wires
α	power law coefficient
μ	density of air
θ	yaw angle of wind (measured from transverse direction)
τ	air density correction factor

Chapter 6

A_t	total wind loading on the panel in the direction of the wind (N)
A_c	total load on the line (N)
C_{xc}	drag coefficient of the line
C_{xti}	drag coefficient for the corresponding *i*-th face
D_{jet}	jet diameter of simulated downburst (m)
G_L	span factor based on the length of the span
G_c	combined wind factor for the line

G_t	combined wind factor for the tower panel
L	wind span of the wires (m)
S_{ti}	total surface area projected normally on the corresponding i-th face (m^2)
$V_{3s,10m}$	3-second gust wind speed at height of 10 m
$V_{10min,10m}$	10-minute mean wind speed at height of 10 m
$V_{10min,10m,MAX}$	10-minute mean wind speed at height of 10 m resulting in collapse
$V_{10min,10m,YLD}$	10-minute mean wind speed at height of 10 m resulting in yield
V_{hor}	horizontal wind speed resulting from downburst
V_{jet}	jet velocity of simulated downburst (m/s)
V_R	reference wind speed
d	diameter of the line (m)
r	distance from downburst to point of interest
z	height above ground (m)
Ω	angle between the wind direction and the wires
α	power law coefficient
μ	density of air
θ	yaw angle of wind (measured from transverse direction)
τ	air density correction factor

Preface

The portions of the experimental data presented in Chapter 2 dealing with cross-arm lattice sections were collected during the author's Masters degree at the University of Western Ontario. However, the focus of the thesis (Mara 2007) was not on the comparison of wind tunnel data to recommended wind loading equations, but rather the aerodynamics of the section under inclined winds (i.e., downbursts). The difference between accepted expressions for wind loads on cross-arm sections and those measured experimentally has recently become an interest of the author, primarily due to his involvement in the committee charged with the updating of ASCE Manual No. 74: Guidelines for Electrical Transmission Line Structural Loading (ASCE 2010). The comparisons and recommendations presented here have not yet appeared in publication and were not included in the author's Masters thesis. However, access and interpretation of the experimental data provided the grounds for selecting the analytical wind loads applied in Chapters 3 through 6, and are therefore included in this thesis. The experimental work comprising the second portion of Chapter 2 was carried out independently by the author in order to further investigate differences observed between experimental and codified drag coefficients. As a result, Chapter 2 is an amalgamation of two papers; the first addresses the drag coefficient of cross-arm lattice sections, while the second addresses the relationship between the drag coefficient and solidity ratio (Mara 2013).

References

ASCE. (2010). Guidelines for electrical transmission line structural loading. ASCE Manuals and Reports on Engineering Practice No. 74 (3rd edition), ASCE, New York, USA.

Mara, T.G. (2007). "The effects of multi-directional winds on lattice sections." M.E.Sc. Thesis, University of Western Ontario.

Mara, T.G. (2013). "Influence of solid area distribution on the drag of a 2-D lattice frame." *J. Eng. Mech.*, doi: 10.1061/(ASCE)EM.1943-7889.0000681.

Chapter 1

1 Introduction

Transmission towers play a vital role in society as components of electrical transmission networks and distribution systems. Specifications for wind loads on transmission structures are provided in the design codes Canadian Standards Association (CSA) C22.3 No. 60826-10 (referred to herein as CSA-2010) (CAN/CSA 2010) and the ANSI National Electric Safety Code (NESC) (ANSI 2006), as well as recommended in ASCE Manual No. 74: Guidelines for Electrical Transmission Line Structural Loading (referred to herein as ASCE-74) (ASCE 2010). Many transmission and distribution companies also have proprietary load and resistance criteria. CSA-2010 adopts the International Electrotechnical Commission (IEC) Standard 60826:2003 (IEC 2003) for design criteria of overhead transmission lines. These codes and guidelines assume a linear elastic response under wind loading and do not discuss the inelastic behavior of transmission structures. As a result, nonlinear inelastic analysis of transmission towers is not frequently carried out in design practice, but becomes necessary for the assessment of ultimate behavior and structural reliability of the tower under wind load.

A large number of transmission line failures throughout the world have been attributed to high intensity winds (HIW) (e.g., Dempsey and White 1996, McCarthy and Melsness 1996, Li 2000). The design methodology provided in current wind loading codes and guidelines is pertinent to, and has been developed based on, synoptic wind events characterized by typical atmospheric boundary layer (ABL) winds. That is, parameters which describe the wind profile with height and quantify effects of turbulence (i.e., gusts) may not provide a proper description of the wind loading conditions under HIW such as downburst, thunderstorm gust fronts or tornadoes. The assessment of tower designs under HIW loading is therefore of great interest for both new and existing structures.

This thesis investigates the nonlinear inelastic response of transmission towers under synoptic wind and HIW loading and provides a comparison of the tower capacities (i.e., yield and maximum) for ABL and downburst wind loading. A self-supported lattice

transmission tower design is modeled in the structural analysis software ANSYS® (ANSYS 2007), which is selected due to its handling of nonlinear material properties and 3-D numerical simulation capability. The analysis considers both material and geometric nonlinearity. A comparison is made between two methods for nonlinear inelastic analysis, the nonlinear static pushover (NSP) method and incremental dynamic analysis, and it is shown that an adequate approximation of the capacity curve of the tower can be obtained using the NSP method. Capacity curves for different wind loading conditions at many directions to the tower are obtained, and are used to develop the capacity surface of the tower.

1.1 Experimental and analytical techniques

As this thesis is prepared in Integrated Article format, detailed descriptions of the experimental and analytical techniques are provided in their corresponding chapters. Brief descriptions of the experimental and analytical techniques used in the thesis are provided in the following subsections.

1.1.1 Wind tunnel testing

Due to the complexity of wind flow through lattice sections, the majority of wind loading provisions in codes and guidelines have been derived from wind tunnel data. Through wind tunnel experimentation, the aerodynamic coefficients (i.e., drag and lift coefficients) can be properly assessed and used to assist in the design of prototype structures. One challenge that exists for reduced-scale experiments with lattice sections is the physical size of the members, which often prohibits testing of an entire structure (i.e., an entire transmission tower). As a result, wind tunnel tests are often limited to sections of the overall structure. The section model which is discussed in Chapter 2 corresponds to the cross-arm portion of a lattice transmission tower, and is carried out at a scale of 1:10. The choice of this scale allows for the details of the angled steel to be properly represented, which is an important feature for geometric similarity. The second experiment is parametric, and does not directly relate to a prototype structure. The wind tunnel testing components of the thesis were carried out in Tunnel I and Tunnel II at the Boundary Layer Wind Tunnel Laboratory at the University of Western Ontario.

1.1.2 Nonlinear static pushover analysis

The primary analysis procedure used in this thesis is the nonlinear static pushover (NSP) method, which has most commonly been used for the evaluation of the nonlinear inelastic response of structures to earthquake-induced ground motion (Krawinkler and Seneviratna 1998). The NSP method is used to evaluate the nonlinear force-deformation relation and identify the yield and maximum capacity of a structure by monotonically increasing the applied forces while maintaining a constant loading profile. The results are presented as capacity curves, which relate the total applied horizontal force on the structure (which is equal to the base shear if inertia forces are negligible) to the deflection of the tip of the tower. As the NSP method is an approximate method, a comparison is first carried out to the incremental dynamic analysis, which considers the time history of the response of a structure under dynamic loading.

1.1.3 Incremental dynamic analysis

The incremental dynamic analysis (IDA) method is commonly used in earthquake engineering to assess the inelastic behavior and capacity of structures under seismic excitation (Vamvatsikos and Cornell 2002). The application of IDA for wind loading differs slightly from its application for earthquake loading, and is described in detail by Banik et al. (2010). Through the IDA method for wind loading, time histories of the maximum total base shear force and corresponding tip displacement are obtained, and these values are used to develop the capacity curve of the tower under ABL wind loading. The resulting capacity curves are compared to those obtained using the NSP method described earlier.

1.2 Objective of thesis

As mentioned earlier, current design for transmission towers under wind loading is often carried out based on the elastic response to traditional ABL winds. This procedure has two shortcomings: i) that the inelastic behavior of transmission towers affects their capacity; and ii) that wind loads deviating from ABL winds likely result in different load effects. The former is of interest if reliability analysis of either point structures or distributed systems is to be carried out, while the latter is relevant to the design of new

towers and the assessment of existing towers for HIW loading. The objectives of the thesis are summarized as follows:

- Assess the relationship of drag load to angle of attack for unique lattice sections, and compare with existing wind loading expressions.
- Provide guidelines for the future investigation of lattice section aerodynamics which may expand the definition of the drag coefficient to include geometric characteristics in addition to the solidity ratio.
- Develop the capacity curve for the transmission tower under ABL wind loading for two nonlinear inelastic structural analysis methods and compare the results.
- Obtain the capacity curve, as well as identify the yield and maximum capacities, of the transmission tower under ABL and downburst wind loading.
- Quantify the uncertainty of the calculated capacities, based on the uncertainty of the structural materials, and compare it to that associated with extreme wind loads.
- Develop capacity surfaces of the transmission tower under different types of wind loading from various directions.

1.3 Organization of thesis

This thesis is prepared in Integrated Article format. A description of the impetus and objective for each chapter are provided in the following sections.

1.3.1 Experimental investigation of lattice section aerodynamics

Relatively little experimental work has been carried out on lattice towers in comparison to other structures such as tall buildings or bridges. Even fewer studies have been directed at unique sections, such as cross-arms or bridges of transmission towers, for which the definition of the drag coefficient (based on solidity ratio) in wind loading codes is less applicable. Wind tunnel data measured for a cross-arm section of a prototype

tower are used to illustrate the behavior of the drag coefficient with angle of attack (yaw angle), and differences are noted between the data and the loading expressions for yawed wind in ASCE-74 (ASCE 2010). The expressions for yawed wind in CSA-2010 are shown to provide a better estimate of the wind loads for the cross-arm section for yawed winds. Thus, the CSA-2010 expressions for wind loading are applied to the numerical transmission tower analysis carried out in subsequent chapters. A significant difference between the drag coefficient measured experimentally and those recommended by codes is observed for the longitudinal face, which is attributed to the non-uniform solid area distribution of the cross-arm geometry. To further investigate this aspect, wind tunnel tests are carried out for a parametric 2-D lattice frame which shows that the drag coefficient may not be fully described by the solidity ratio. While additional work needs to be carried out in this regard, the results of the study identify the important parameters and provide guidelines for the progression of research.

1.3.2 Comparison of capacity assessment methods for a lattice transmission tower

Through a comparison of the NSP and IDA methods for a 2-D numerical model of a transmission tower carried out by Banik et al. (2010), it was shown that the NSP method is sufficient for the estimation of the capacity curve of the tower. Moreover, it was shown that the capacity curves obtained through the NSP analysis are representative of the peak wind load effects on the structure. In this chapter, comparisons are made between the NSP and IDA methods for a 3-D numerical model of a transmission tower, which includes the effects due to vertical coherence in the wind. It is shown that the NSP method provides an adequate approximation of the capacity curve of the tower compared to the IDA method, and that the duration of the time history used for the IDA has little effect on the resulting capacity curve for the time intervals considered. The NSP method is employed for the estimation of the transmission tower capacity in the subsequent chapters due to its computational efficiency.

1.3.3 Capacity of a transmission tower under ABL and downburst wind loading

Current design codes for lattice transmission structures contain very limited advice on the treatment of HIW, and structural design is often carried out using wind load profiles and response factors derived for ABL winds. Due to the paucity of full-scale HIW data, the structural engineering community has turned to numerical simulations of these events to aid in the assessment and design of structures. Downburst configurations resulting in the peak wind speeds on the transmission tower are identified and extracted from a numerical simulation of a stationary downburst carried out by Hangan et al. (2003), and are used to assess the capacity curve of the transmission tower under downburst wind loading. The capacity curves obtained through the NSP analysis are compared to the time history response of the tower under a transient downburst passage, and are shown to agree well. The capacity curve of the tower under downburst wind loading is shown to remain relatively consistent under various downburst sizes, and the capacity curves for the transverse and longitudinal directions under various downburst scenarios are shown to be approximately bound by the capacity curves for a rectangular wind loading profile and an ABL wind loading profile. An uncertainty propagation analysis is carried out, based on the simple Monte Carlo technique considering material and geometric uncertainty, which indicates that the coefficient of variation of the tower yield capacity is small compared to those associated with extreme wind speeds.

1.3.4 Effect of relative orientation on the capacity of a transmission tower under downburst loading

The wind loads on a transmission tower vary significantly with wind direction due to both the geometry of the tower and the contribution of the wires. Based on the findings which indicate that the capacity curves in the transverse and longitudinal wind directions are approximately bound by the rectangular and ABL wind profiles on the upper and lower bound, respectively, the analysis is extended to consider wind at oblique directions. While this is relatively straightforward for the ABL and rectangular winds, the application of the downburst wind field to the tower model is more complex. The capacity curves for 11 wind directions under three downburst scenarios are obtained and

compared, and it is shown that the capacity of the tower varies with both wind direction and size of downburst. The methods used for the application of the simulated downburst wind field to the numerical tower model are discussed, and it is shown that the capacity curves obtained for downburst wind loading are similar in behavior with the exception of very small downburst events.

1.3.5 Effect of wind direction on the response and capacity surface of a transmission tower

The wind loads on a transmission tower vary significantly with wind direction due to both the geometry of the tower and the contribution of the wires. The NSP method is used to obtain the capacity curves for 11 wind directions under ABL and rectangular wind loading, and it is shown that the yield and maximum capacities of the tower vary with wind direction. The deformation trajectories are projected on the horizontal plan for each wind direction, and it is shown that they do not overlap for closely spaced directions (i.e., 10°). As the deformation trajectories are sufficiently smooth, it is suggested that the capacity curves obtained for the individual wind directions can be used to form the capacity surface of the transmission tower. Capacity surfaces for the tower are developed for the ABL and rectangular wind profiles, and it is shown that they do not intersect. It was previously shown that the capacity curves for the transverse and longitudinal wind directions under ABL and rectangular wind profiles can provide approximate bounds to the capacity curves obtained for downburst wind loading. To confirm that this conjecture holds for oblique wind directions, the capacity surfaces for three downburst scenarios are developed and compared to those for ABL and rectangular wind profile. Except in the case of very small downbursts, the capacity surfaces developed for the rectangular and ABL wind profiles are shown to envelope those for the downburst wind profiles.

1.4 Research highlights

Contributions to the field of design and analysis of transmission towers are summarized below:

- Experimental data describing the relationship of drag force to angle of attack for a typical transmission tower cross-arm section are presented, which indicate better

agreement with the wind load expressions in CSA-2010 (CSA 2010) than for those in ASCE-74 (ASCE 2010).

- Experimental data which shows the relationship between solid area distribution and the drag coefficient of a 2-D lattice frame are presented, which suggests that current definitions of the drag coefficient (which are purely based on the solidity ratio) should be further developed for use with unique lattice sections such as cross-arms and bridges.

- A comparison of the IDA and NSP methods for obtaining the force-deformation relationship of a structure is carried out, which shows that the capacity curves obtained by the NSP analysis provide an adequate approximation of those obtained by the IDA method.

- The NSP method is used to develop the capacity curve of a transmission tower under ABL, rectangular and downburst wind loading, which indicates that the capacity curve under downburst is approximately enveloped by those obtained for ABL and rectangular winds.

- The NSP method is used to develop the capacity curves of a transmission tower for many wind loading directions, and the curves are used to develop the capacity surface for the tower.

- The capacity surfaces resulting for ABL and rectangular wind load profiles are shown to approximately envelope that for downbursts of typical size.

1.5 References

ANSYS® (2007). ANSYS Multiphysics, Release 9.0. ANSYS Inc., Canonsburg, PA.

ANSI. (2006). National Electrical Safety Code. ANSI C2. IEEE, Piscataway, NJ.

ASCE. (2010). Guidelines for electrical transmission line structural loading. ASCE Manuals and Reports on Engineering Practice No. 74 (3rd edition), ASCE, New York, USA.

Banik, S.S., Hong, H.P. and Kopp, G.A. (2010). "Assessment of capacity curves for transmission line towers under wind loading." *Wind Struct*., 13(1), 1-20.

Canadian Standards Association (CSA) (2010). Design criteria of overhead transmission lines. CAN/CSA-C22.3 No. 60826-10, CSA, Toronto, Canada.

Dempsey, D. and White, H.B. (1996). "The cause of most transmission structure outages in the world is high intensity winds." *Transmission and Distribution World*, 48(6), 32-42.

Hangan, H., Roberts, D., Xu, Z. and Kim, J.-D. (2003). "Downburst simulations. Experimental and numerical challenges." *Proc. of the 11th International Conference on Wind Engineering*, Lubbock, TX, USA.

International Electrotechnical Commission (IEC) (2003). Design criteria of overhead transmission lines. IEC Standard 60826:2003, 3rd edition.

Krawinkler, H. and Seneviratna, G.D.P.K. (1998). "Pros and cons of a pushover analysis of seismic performance evaluation." *Eng. Struct*., 20(4-6), 452-464.

Li, C.Q. (2000). "A stochastic model of severe thunderstorms for transmission line design." *Prob. Eng. Mech*., 15(4), 359-364.

McCarthy, P. and Melsness, M. (1996). "Severe weather elements associated with September 5, 1996 hydro tower failures near Grosse Isle, Manitoba, Canada." Environment Canada, Winnipeg, Canada.

Vamvatsikos, D. and Cornell, C.A. (2002). "Incremental dynamic analysis." *Earthquake Engng Struct. Dyn.*, 31, 491-514.

Chapter 2

2 Experimental investigation of lattice section aerodynamics

The drag coefficient of a lattice frame is a fundamental parameter for the calculation of the resulting wind loads. While values for the drag coefficient of most bluff bodies have been well-established in the literature, those for lattice frames have been less examined. One of the primary reasons for this is that the interaction of wind with lattice sections is more complex than that for a bluff body. A 3-D lattice frame is often considered to have a windward face and a leeward face; the interaction of the wind as it passes through the windward face significantly affects the drag force on the leeward face. This mechanism is referred to as shielding, and is, for all intents and purposes, impossible to assess analytically. As a result, wind tunnel testing has played a large role in the development of expressions for the drag coefficient of 3-D lattice frames. In wind design codes, the specified drag coefficient is based solely on the solidity ratio, although different expressions are provided for sections comprised of flat-sided or round members; this is the case for both 2-D and 3-D frames.

The following sections describe the findings of wind tunnel tests carried out on two different models. The first model is a 3-D lattice frame, which represents the cross-arm section of a guyed transmission tower, and is used to illustrate the behavior of the drag force with yaw angle (angle of attack of the wind). The second model is a basic 2-D frame, and is used to illustrate that the commonly-used definition for the drag coefficient should likely be refined to consider characteristics in addition to solidity ratio. The findings of the experimental work suggest that the existing equations in ASCE Manual No. 74: Guidelines for Electrical Transmission Line Structural Loading (ASCE 2010a) for yawed wind should be used with caution for the calculation of wind loads on lattice towers, and that the drag coefficient of lattice sections should be expressed as a function which considers characteristics in addition to the solidity ratio.

2.1 Aerodynamics of cross-arm sections

Lattice transmission towers play a crucial role in the efficient transmission of electricity and are used throughout the world. Guyed and self-supported lattice transmission towers are typically comprised of two unique geometries: the vertical tower body and the horizontal conductor support cross-arm. A great deal of research has been directed at the evaluation of aerodynamic coefficients of the compact and symmetric form often seen in the vertical portion of the tower, however much less information is available for cross-arm sections. Wind tunnel tests carried out on a typical cross-arm design indicate that the drag loads vary significantly with wind direction, and exhibit a relationship which differs from the design procedure provided in ASCE Manual No. 74: Guidelines for Electrical Transmission Tower Structural Loading (herein referred to as ASCE-74) (ASCE 2010a). The wind tunnel data suggest that ASCE-74 does not provide a conservative design estimate of the transverse tower loads for skewed wind directions. This is a result of the orthogonal approach taken in ASCE-74, which calculates the transverse and longitudinal wind loads independently. A recommendation for an alternative to the current wind load calculation procedure in ASCE-74 is made, which is most pertinent to portions of the tower with significantly different geometric and aerodynamic characteristics in the transverse and longitudinal planes. While the design wind loads for the transverse direction are quite dependent on the contributions of the wires, the wind loads on the tower structure remain important.

2.1.1 Background

Power distribution and utility companies around the world rely on networks of towers and conductors to efficiently transmit and distribute electrical power. Many codes, regulations and guidelines are currently in use throughout the world. Documents commonly referenced in North America include: ANSI National Electric Safety Code (NESC-2006); ASCE Manual No. 74 (ASCE-74); CAN/CSA C22.3 No. 60826-10 (CSA-2010); and International Electrotechnical Commission Standard 60826:2003 (IEC-2003). Note that CSA-2010 adopts IEC-2003 and therefore contains an identical treatment of aerodynamics. It is acknowledged that ASCE-74 is not explicitly a code, however it is widely referenced throughout the United States and elsewhere. For brevity, the above

documents are herein referred to as codes. The design of transmission towers, lines and components depend on a large number of variables including: system demand; local geography, topography and obstacles; local wind climate; local potential for ice accretion; geometric design options for the tower structure; and political boundaries. Many of these variables are clearly beyond the control of the designer due to environmental or political reasons. The discussion in this chapter is limited to the wind loads on the tower structure, with particular focus on the aerodynamics of the cross-arm section used for the support of conductors in guyed or self-supported lattice transmission towers.

The wind loads on transmission towers are often interpreted as loads in the transverse (perpendicular to the conductors) and longitudinal (parallel to the conductors) directions. While no wires, conductors or otherwise, are considered in this section, the wind loading of the tower is referenced using this terminology. The angle of the wind with respect to the tower is referred to as the yaw angle, which is taken as 0° for wind in the transverse direction and 90° for wind in the longitudinal direction. This sign convention is shown in Figure 2.1 and is consistent with that used in ASCE-74.

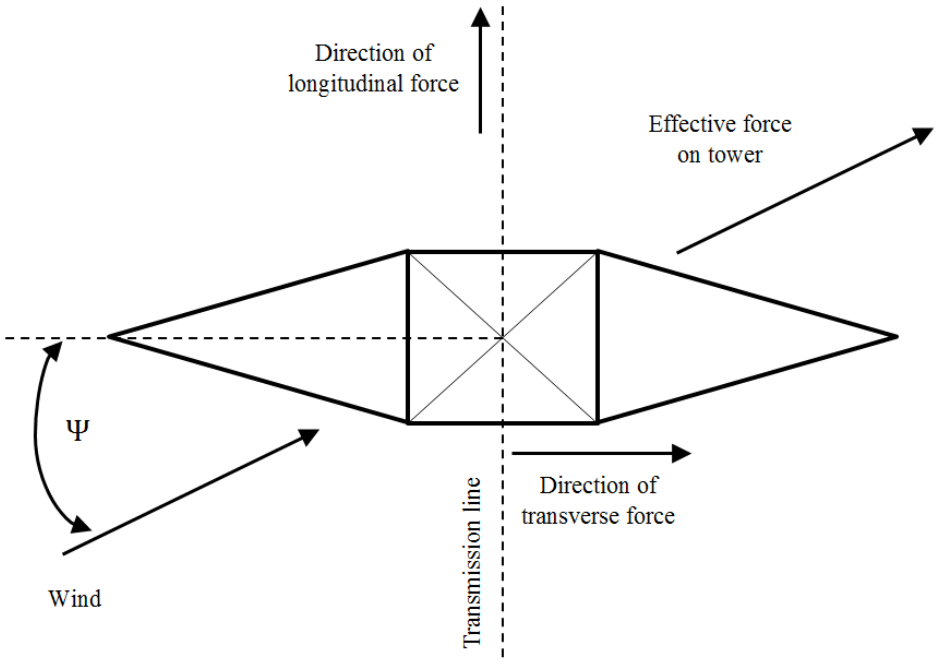

Figure 2.1. Sign convention for lattice transmission towers.

The variation of wind loads on the tower structure with respect to yaw angle, with particular focus on the contribution of the cross-arm section, are discussed in this chapter. While a great deal of research has been directed at the evaluation of the aerodynamic coefficients (i.e., drag coefficient) of 3-D lattice frames which are either square or triangular in plan, very few studies involving other geometries commonly used in tower design (i.e., cross-arms, bridges) have been carried out. In the case of guyed or self-supported towers, these are the cross-arms used for conductor support. In delta configurations, these types of configurations are found in the bridge of the tower. The application of code-specified drag coefficients for these types of sections may not be appropriate, as the provided drag coefficients, and their implied use in the codes, are based on the notion that: i) the sections have similar geometric and aerodynamic parameters in the transverse and longitudinal planes; ii) the sections have similar aspect ratios (about the plan view) in the transverse and longitudinal planes; and iii) that the distribution of member area within a representative section is relatively uniform. While the latter is often true for bridge sections of a delta configuration, neither cross-arms nor bridges conform to the former two criteria. As it will be seen, this has implications on the calculation of the wind load in the transverse and longitudinal directions, the extent of which vary depending on the design approach taken.

Wind tunnel tests were carried out to assess the drag coefficient of the cross-arm section of a prototype tower design as a component of a larger research initiative (see Hangan et al. 2008). Very little aerodynamic data pertaining solely to the assessment of the drag coefficient for a cross-arm section are available in the literature. Only two studies involving unique lattice sections could be found in the literature: de Oliveira e Silva et al. (2006) presents wind tunnel data for various sections of delta towers, and Mara et al. (2010) presents experimental data for a tower cross-arm under inclined winds. It was concluded by de Oliveira e Silva et al. (2006) that the IEC-2003 expression was sufficient for the description of wind loads on the investigated sections. In the following chapter, experimental data are expressed as the net drag on the cross-arm, as well as decomposed into drag in the transverse and longitudinal directions. The results are compared to the relationship of wind load with yaw angle in ASCE-74 and IEC-2003. It is shown that the behavior of the drag force of the cross-arm section is much better estimated using the

procedure in IEC-2003, which accounts for wind loads arising from differences in the transverse and longitudinal aspect ratios. It is recommended that the IEC-2003 method, or a modified procedure of the calculation of wind loads using existing expressions in ASCE-74, be used for the calculation of wind loads on these types of sections (or preferably for the entire tower). It is acknowledged that for some tower designs the wind load contribution from the cross-arm section may be small in relation to the overall loads on the tower, although this ratio will vary among tower designs (Mara and Ho 2011).

2.1.2 Aerodynamics of lattice sections

The basic calculation of the drag wind load, F_d, on a lattice section is

$$F_d = 0.5\,\rho V^2 C_d A_p \tag{2.1}$$

where ρ is the density of air, V is the wind speed at the height of the section, C_d is the drag coefficient and A_p is the projected area subject to wind load. In most wind design codes, the drag coefficient for a lattice frame or tower section is specified as a function of solidity ratio, ϕ,

$$\phi = A_{net} / A_{gross} \tag{2.2}$$

where A_{net} and A_{gross} are the net and gross areas of the face of a frame or tower section.

Early investigations of the force coefficients of lattice frames were focussed on the assessment of wind loads on bridge trusses or girders (Flachsbart 1932, Biggs 1954, Pagon 1958). At the time of these experiments, it was generally accepted that a relationship existed between the solidity ratio and the drag coefficient, and drag force data were often obtained at full scale. The relationship between the drag coefficient and solidity ratio for single trusses proposed by Pagon (1958) remained in the ANSI Standard until 1982 (ANSI 1982), although much of the design work for lattice towers remained on an *ad hoc* basis. As accessibility to wind tunnel laboratories increased and more experiments could be carried out at reduced scales, studies which extend beyond a single or double truss emerge in the literature. Sykes (1981) and Bayar (1986) found similar relationships to Pagon's over a limited range of solidity ratio. Whitbread (1977), Clow

(1978), Sykes (1981) and Bayar (1986) carried out wind tunnel tests on 3-D lattice trusses and towers, investigating aerodynamic coefficients, shielding and turbulence effects. de Oliveira e Silva et al. (2006) tested multiple delta configurations to assess the IEC-2003 expression for yawed winds on complex sections; the findings indicated that the IEC-2003 expression was adequate. The effect of shielding for lattice frames was also assessed via building frames by Georgiou and Vickery (1979), Whitbread (1979) and Kopp et al. (2010). Mara et al. (2010) investigated the behaviour of the drag coefficient of 3-D frames under winds having significant vertical components (i.e., downbursts, thunderstorm gust fronts). Comparison between model-scale and full-scale wind tunnel test data for a triangular 3-D lattice tower section was made by Mara and Galsworthy (2011), which showed good agreement between measurements of the drag coefficient at model- and full-scale.

The majority of these experiments, as well as others in the literature, have focussed on sections which are relatively symmetric about both planes of loading (i.e., similar geometric and aerodynamic characteristics, as well as aspect ratio, in the transverse and longitudinal planes), and have a relatively uniform distribution of solid area throughout the section. These conditions are indeed representative of the majority of sections comprising most lattice tower designs, however they are not applicable to cross-arm or bridge geometries. In the following sections, the differences which arise between the wind tunnel data for the cross-arm model and the wind loads calculated using ASCE-74 and IEC-2003 are discussed.

2.1.3 Wind tunnel experiment

Many challenges exist when attempting model-scale experimentation on lattice sections, primarily due to the physical size and detailing of the members. This aspect has contributed to a relatively small amount of wind tunnel data for lattice sections available in the literature when compared to those available for buildings and other structures. The scarcity of published data may also be attributed to the proprietary nature of the utility industry for security or financial reasons.

Following a series of transmission tower failures under high intensity winds (see McCarthy and Melsness 1996), a research initiative was commenced by Manitoba Hydro (MH) to better understand the wind effects on transmission structures (Hangan et al. 2008). For the wind tunnel testing component, static models were built for the evaluation of the drag coefficient of a cross-arm section under inclined winds (Mara 2007). A model of a MH Type A402 HVDC guyed tower cross-arm was constructed using angled brass sections at a scale of 1:10. An elevation view of the entire tower is shown in Figure 2.2, in which the modeled cross-arm corresponds to Panel 6. The geometric and aerodynamic parameters for each panel are listed in Table 2.1. All member connections were soldered and rigid. Cross-section widths of the angle members ranged from 5.5 mm to 9.5 mm, and were scaled directly from the prototype design. The particular tower design considered has two cross-arms; the cross-arm which was modeled represents the major cross-arm that supports the weight of the conductors, rather than the minor cross-arm used for the guy connections. The model was mounted on a strut in order to elevate the cross-arm above the boundary layer on the tunnel floor. The wind load accumulated by the strut was consistent among all test configurations, and was treated as a tare subtraction from the overall measurement of the drag force. The cross-arm model is shown installed in the wind tunnel at yaw angles 0°, 45° and 90° in Figure 2.3.

Table 2.1. Geometric and aerodynamic parameters for MH Type A402 HVDC guyed tower for the a) transverse plane and b) longitudinal plane. The parameters for the major cross-arm (Panel 6) appear in bold.

a)

Panel	Total Area (m^2)	Net Area (m^2)	Height (m)	Solidity	C_d (ASCE)	C_d (IEC)
1	5.12	1.15	3.05	0.23	2.90	2.77
2	14.95	1.93	10.55	0.13	3.42	3.23
3	14.72	2.3	19.38	0.16	3.27	3.08
4	14.03	2.52	27.95	0.18	3.16	2.99
5	5.04	1.51	33.36	0.30	2.54	2.50
6	**3.84**	**2.07**	**36.25**	**0.54**	**1.80**	**1.88**
7	5.17	0.77	39.31	0.15	3.32	3.13

b)

Panel	Total Area (m^2)	Net Area (m^2)	Height (m)	Solidity	C_d (ASCE)	C_d (IEC)
1	3.47	1.26	3.05	0.36	2.23	2.30
2	10.77	1.74	10.55	0.16	3.27	3.08
3	12.09	2.17	19.38	0.18	3.16	2.99
4	13.19	2.65	27.95	0.20	3.06	2.90
5	5.04	1.76	33.36	0.35	2.28	2.33
6	**17.24**	**3.62**	**36.25**	**0.21**	**3.01**	**2.85**
7	10.35	1.04	39.31	0.10	3.58	3.38

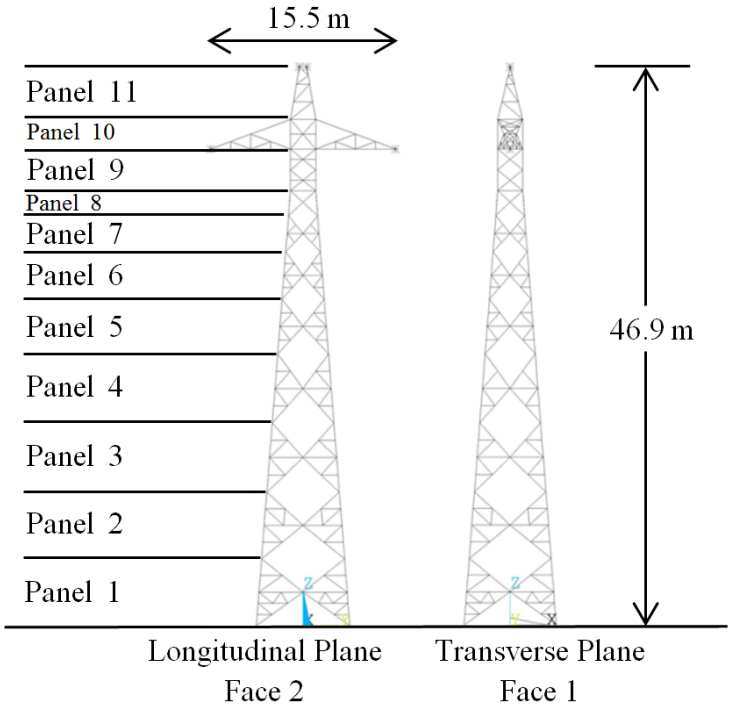

Figure 2.2. Elevation views of MH Type A402 HVDC guyed tower showing each design plane.

All wind tunnel testing was carried out in Tunnel I at the Boundary Layer Wind Tunnel Laboratory at the University of Western Ontario. The dimensions of the tunnel at the test section are 2.4 m by 2.1 m in width and height, respectively. The wind profile was uniform over the dimensions of the model, and all testing was carried out at a wind speed of approximately 7.6 m/s. This speed, coupled with the smallest member size, resulted in a Reynolds number of approximately 4 x 10^3 for the data presented here, although

a) 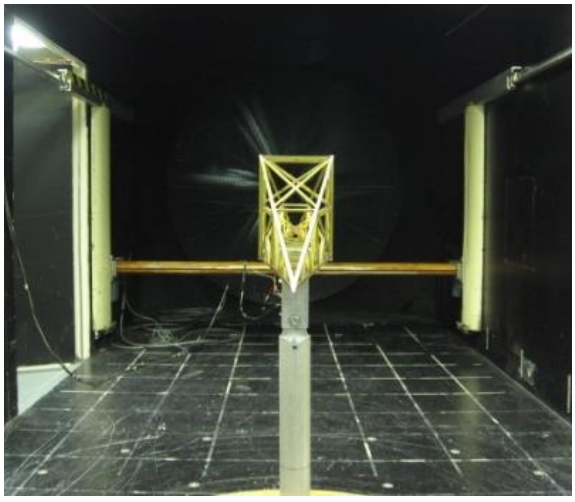

b) 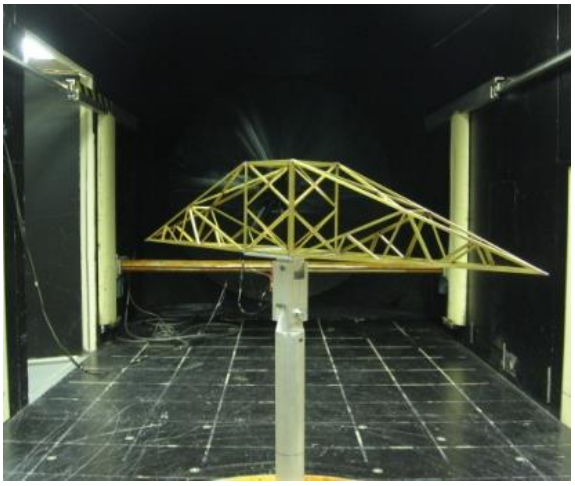

c) 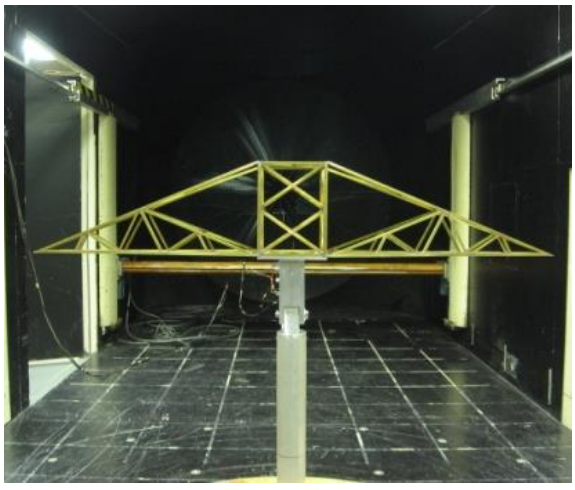

Figure 2.3. Cross-arm model shown in wind tunnel at a) 0° (transverse), b) 45°, and c) 90° (longitudinal).

additional tests were carried out at Reynolds numbers ranging from 2.3×10^3 to 6.9×10^3. No effects due to Reynolds number were observed. The longitudinal turbulence intensity of the wind was approximately 7%. The range of Reynolds number and level of turbulence intensity is consistent with previous work carried out on lattice sections of similar scale (Sykes 1981, Bayar 1986, Carril Jr. et al. 2003) and provides an accurate estimate of the drag coefficient. Any effects due to support interference were found to be negligible and the total model and strut blockage was less than 5%, therefore no correction for blockage was applied. Measurements of the mean drag force were taken for wind directions at 10° intervals over a range of 180°. The drag force was measured using a robust load cell at the base of the strut, which was necessary to support the weight of the model.

2.1.4 Wind tunnel test results and discussion

The drag coefficients were first compared to the values suggested by codes for the transverse and longitudinal wind directions. The solidity ratios of the cross-arm section in the transverse and longitudinal planes are 0.54 and 0.21, respectively. The experimental drag coefficients, as well as relationships developed through previous work (Bayar 1986) and codes (ASCE-74 and IEC-2003), are shown in Figure 2.4. The experimental drag coefficient for the cross-arm at 0° is in good agreement with the expected values. However, the experimental drag coefficient for the cross-arm at 90° (when the face of the cross-arm is fully exposed) is noticeably lower than would be estimated using the codes. The difference may be attributed to the fact that the expressions for drag coefficients provided in the codes are not intended for this type of geometry, and that the distribution of solid area within the frame is not uniform. The latter is investigated further in the second half of this chapter (Mara 2013). The drag coefficients in codes are based on experimental work performed on sections having uniform geometry and solidity over the section length, thereby giving appropriate estimates for a given solidity ratio over a section having uniform spacing. The geometry of the cross-arm, most notably the spaces with no members in the upper portion and tapers in the plan view, results in varying drag across the body of the cross-arm. As well, the definition of solidity ratio often implies a relatively uniform spacing of solid area

(A_{net}) within the enclosed area (A_{gross}), which is not representative of this particular cross-arm.

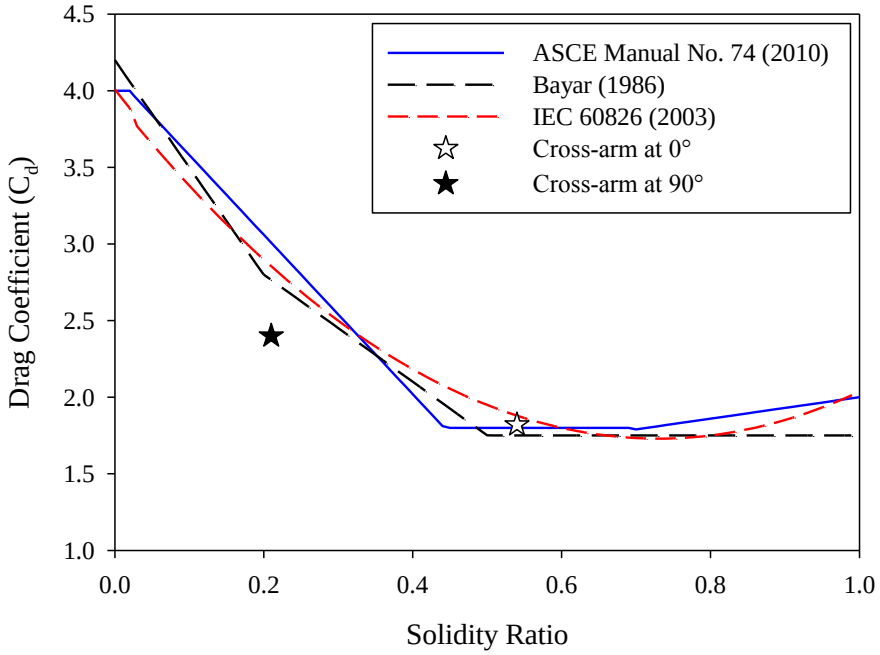

Figure 2.4. Experimental drag coefficients for cross-arm at orthogonal directions compared to previous work and code values.

The expression for drag force given in Eq. (2.1) implies that A_p is representative of the area subject to wind load. At this point, it is necessary to emphasize the difference between the true projected area, A_p, and the definition of area used in lattice tower design codes. For solid bodies, the calculation of A_p at wind directions other than the normal directions (i.e., wind normal to each face) is straightforward; this is not the case for lattice sections. For bluff bodies, the geometric dimensions are simply projected on the planes normal to a skewed wind to yield a representative projected area. However, due to the porosity of lattice sections, additional area becomes exposed or shielded with change in the yaw angle. In the case of 3-D frames, this affects the load on the windward face (due to the orientation), as well as the load on the leeward face (due to orientation, area exposure, and shielding effects). These characteristics complicate the calculation of the projected area, and pose a significant challenge to a proper assessment of the effects due to shielding. This is clearly inconvenient for design purposes. As a result, the calculation

of wind loads on lattice sections at skewed wind directions in most wind design codes are functions of the geometric and aerodynamic parameters of each of the faces (i.e., the transverse and longitudinal faces) of the 3-D frame. The use of wind tunnel testing to evaluate the drag loads on a 3-D frame circumvents both the estimation of projected area and a quantification of shielding mechanisms, as these are inherently included in the experiment. Thus, to present meaningful results, as well as to facilitate comparison with code-calculated values, the drag coefficient and projected area are left as a coupled term referred to as effective drag, C_dA_p. By doing so, the differences in the calculations of the basic aerodynamics between codes can be compared. This terminology is similar to the effective projected area (EPA) approach taken by ANSI/TIA 222-G (ANSI 2006), and facilitates comparison of the drag load at different yaw angles as the change in projected area is implicitly included in the measurement. Note that the term C_dA_p is associated with the unit m^2, and thus must be scaled from model-scale to full-scale; this scaling factor has been included in the plots of the wind tunnel data. Bayar (1986), who carried out an assessment of the drag force relationship with yaw angle for the vertical span of two towers, also presents results in this fashion.

The mean drag force at yaw angle ψ, $F_d(\psi)$, can be decomposed into vector components aligned with the transverse and longitudinal axes of the model as shown in Eq. (2.3).

$$F_d(\psi) = 0.5\rho V^2(C_dA_p(\psi)) \tag{2.3a}$$

where the term C_dA_p varies with yaw angle ψ, and can be calculated directly from the experimental data by normalizing the net drag force by the dynamic pressure $0.5\rho V^2$. The drag forces and effective drag in the transverse and longitudinal directions are then calculated as

$$F_T(\psi) = F_d\cos(\psi) \qquad \text{and} \qquad (C_dA_p(\psi))_{\mathrm{T}} = (C_dA_p(\psi))\cos(\psi) \tag{2.3b}$$

$$F_L(\psi) = F_d\sin(\psi) \qquad \text{and} \qquad (C_dA_p(\psi))_{\mathrm{L}} = (C_dA_p(\psi))\sin(\psi) \tag{2.3c}$$

where $F_T(\psi)$ and $F_L(\psi)$ are the transverse and longitudinal forces at yaw angle ψ, respectively. $(C_dA_p(\psi))_{\mathrm{T}}$ and $(C_dA_p(\psi))_{\mathrm{L}}$ are the effective drag in the transverse and longitudinal directions at yaw angle ψ, respectively. Note that the effective drag is

calculated by normalizing the drag force by the dynamic pressure, which is also the case for the transverse and longitudinal drag forces. When interpreting the meaning of the effective drag for a 3-D frame, it is important to appreciate that the effects of shielding are included. The effective drag measurements for the cross-arm section are shown for the net, transverse and longitudinal directions in Figure 2.5. A smooth relationship exists for the net effective drag with yaw angle, as well as for the transverse and longitudinal effective drag. Note that the maximum transverse effective drag occurs at a yaw angle of 40°, and is approximately 45% greater than that for a yaw angle of 0°. In the following section, comparisons are made between the net, transverse and longitudinal effective drag as measured experimentally and as calculated using ASCE-74 and IEC-2003.

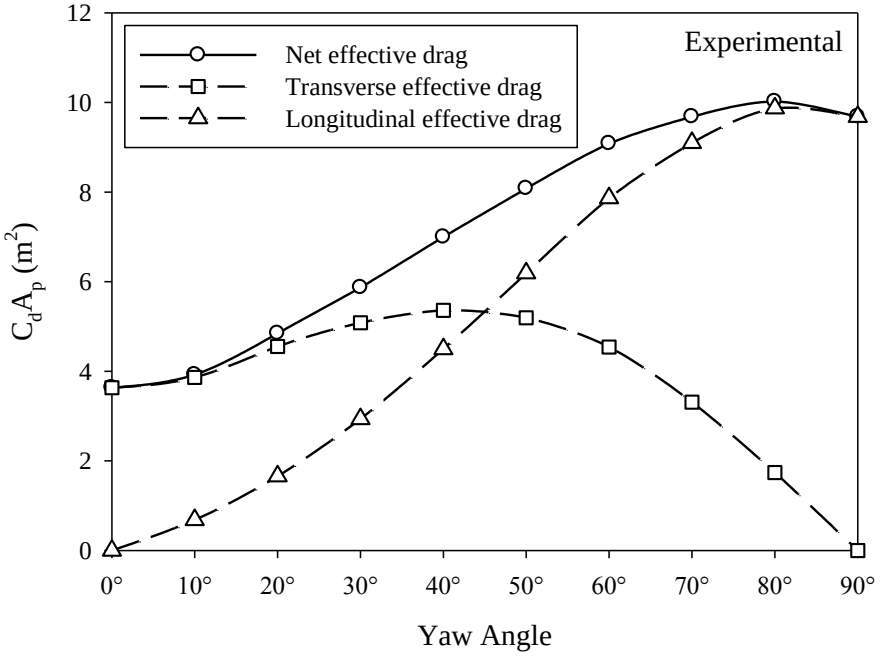

Figure 2.5. Experimental effective drag decomposed into the transverse and longitudinal directions.

2.1.5 Comparison of experimental data to design criteria

2.1.5.1 Existing equations in ASCE-74 and IEC-2003

In order to facilitate comparison with the referenced codes and guidelines, the nomenclature of the referenced codes is retained in the following equations. This

excludes the nomenclature used for constants and factors unrelated to the tower itself, which are arbitrary.

In ASCE-74, it is recommended to calculate the transverse force, F_t, and longitudinal force, F_l, independently, based on the geometric and aerodynamic parameters of each corresponding face. These expressions are shown in Eq. (2.4).

$$F_t = BC_{ft}A_{mt}\cos(\psi) \tag{2.4a}$$

$$F_l = BC_{fl}A_{ml}\sin(\psi) \tag{2.4b}$$

where $B = \gamma_w Q K_z K_{zt} V^2 G_{t1}$, C_{ft} and C_{fl} are the drag coefficients of the transverse and longitudinal faces respectively, and A_{mt} and A_{ml} are the net areas of the transverse and longitudinal faces respectively. Thus, the equation is based on vector components of wind passing through each of the orthogonal faces. This technique makes the assumption that there is no difference between the vector decomposition of the resultant drag force (in the ψ direction) and the orthogonal drag forces calculated independently by Eq. (2.4). This assumption holds for the transverse and longitudinal wind directions (i.e., 0° and 90°), and is relatively valid providing there is little difference in the aerodynamic parameters and aspect ratio of the section under consideration (i.e., the vertical portion of the tower). However, as it will be shown, the calculation of drag forces on the cross-arm for skewed wind directions, and thus for the complete tower, are affected by this assumption. The use of Eq. (2.4) results in the following: i) the relationship of the drag force with yaw angle for the cross-arm is significantly different than if the resultant wind load is considered, and; ii) the maximum transverse drag force attributed to the cross-arm occurs at a yaw angle of 0°.

In IEC-2003 (and therefore CSA-2010), it is recommended to calculate the resultant drag force, A_t, in the direction of the wind using a combination of the aerodynamic parameters from each face, along with an additional magnification factor dependent on yaw angle. For the design of the transverse and longitudinal planes, the resultant force would be decomposed into forces in the transverse and longitudinal directions, respectively. The IEC-2003 expression is shown in Eq. (2.5).

$$A_t = D\,(1 + 0.2\,\sin^2(2\theta))(C_{xt1}S_{t1}\cos^2\theta + C_{xt2}S_{t2}\sin^2\theta) \quad (2.5)$$

where $D = q_o G_{t2}$, θ is the yaw angle of the wind (taken as 0° for the transverse direction), C_{xt1} and C_{xt2} are the drag coefficients of the transverse and longitudinal faces respectively, and S_{t1} and S_{t2} are the net member areas of the transverse and longitudinal faces respectively. It should be noted that Eq. (2.5) appeared as an option in the 2nd edition of ASCE-74 (ASCE 1991), but was removed for the 3rd edition (ASCE 2010a).

NESC-2006 suggests using a force coefficient of 3.2 on the sum of the projected area of the members in the face (for flat surfaces), with an upper bound imposed that it need not exceed the load that would occur on a solid structure of the same dimensions. It is noted that this may be amended if wind tunnel testing or a qualified engineering study justifies a reduction. The aerodynamic behaviour as described by NESC-2006 is not included in the following comparisons.

As the constants B and D are related to oncoming wind characteristics only, the difference in the aerodynamic behaviour among codes and experiments can be directly compared through the respective values of effective drag ($C_d A_p$). Note that slight differences exist between the drag coefficients suggested by each of the codes, and that the impact of these can be observed by comparing the values of effective drag at 0° and 90°. In the case of each code, the drag coefficients used in the calculation of effective drag, as well as the corresponding areas, are provided in Table 2.1.

The net effective drag is shown for ASCE-74, IEC-2003 and the wind tunnel data at various yaw angles in Figure 2.6, and shows that the relationship is relatively similar in shape between the codes and the experiment. However, the magnitude of the experimental effective drag gradually becomes lower than the codes as the broad face of the cross-arm becomes more exposed. This is explained by the lower drag coefficient measured for these wind directions, as discussed in the previous section. More significant differences appear if the transverse and longitudinal effective drags are compared, which are plotted in Figures 2.7 and 2.8, respectively. For the transverse effective drag, there is a substantial difference in the shape with yaw angle between ASCE-74 and those for IEC-2003 and the experimental data. The greatest transverse

effective drag as calculated by ASCE-74 occurs for wind at 0°, for IEC-2003 it occurs (by definition) for wind at 45°, and for the experimental data it occurs for wind at 40°. For the longitudinal effective drag, differences in the shape of the effective drag with yaw angle are again shown, although in this case ASCE-74 results in a higher estimate compared to IEC-2003 and the experimental data. The differences between the IEC-2003 curve and the experimental data are again attributed to the lower drag coefficient measured in the wind tunnel tests. In each case, the IEC-2003 expression results in a relationship between effective drag and yaw angle which is closer to that observed in the wind tunnel tests.

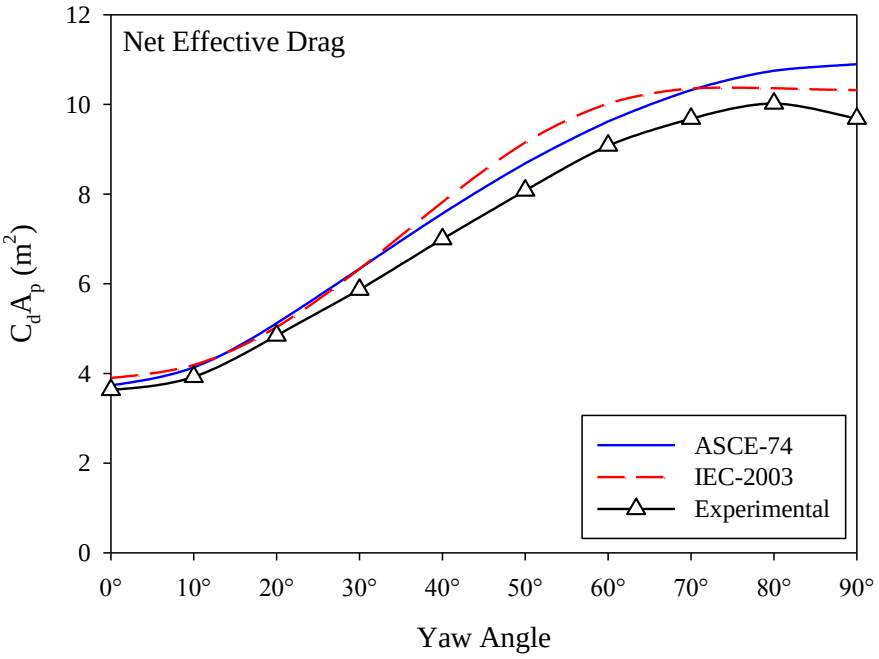

Figure 2.6. Net effective drag for the cross-arm based on parameters in Table 2.1 using codes and experimental data.

Based on the experimental data, it is shown that Eq. (2.5), while capturing the shape of the transverse effective drag, yields a conservative estimate of the magnitude. However, this is preferable to the use of the ASCE-74 expressions, where the maximum transverse effective drag occurs at a yaw angle of 0°. This difference is not as severe for cross-sections which are relatively symmetric about the transverse and longitudinal planes, which is the intended use of the force coefficients (drag coefficients) in ASCE-74.

However, in the worked example provided in ASCE-74, the wind loads are calculated for a hanger section having significant differences between the design planes using Eq. (2.4).

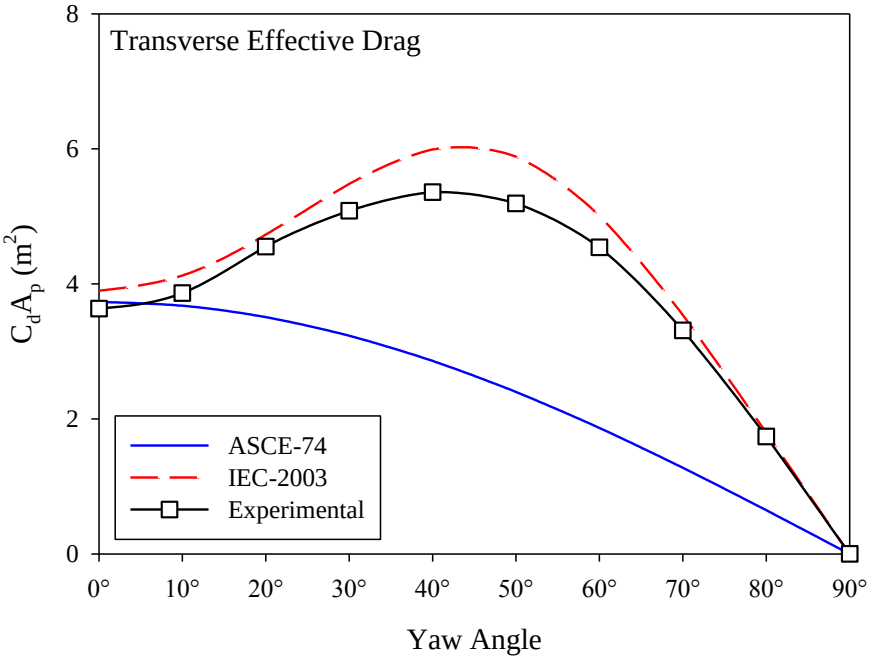

Figure 2.7. Transverse effective drag for the cross-arm based on parameters in Table 2.1 using codes and experimental data.

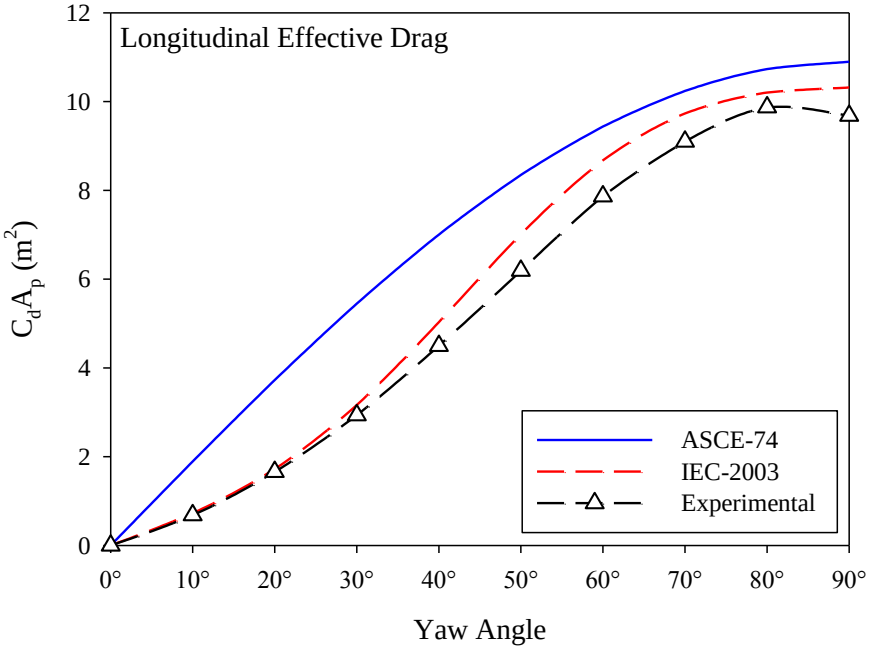

Figure 2.8. Longitudinal effective drag for the cross-arm based on parameters in Table 2.1 using codes and experimental data.

It is recommended that the IEC-2003 equation be referenced in ASCE-74, at the very least for portions of the tower which are characterized by significant differences between the transverse and longitudinal planes (i.e., different geometric and aerodynamic parameters or aspect ratio). The calculated wind loads for the pure transverse and longitudinal directions are unaffected by this recommendation, as they are based wholly on the geometric and aerodynamic parameters of the transverse and longitudinal faces, respectively. However, the calculation of wind loads for skewed wind directions is affected by this recommendation, and better estimates of the overall aerodynamic behaviour due to differences between the transverse and longitudinal faces are made through the use of the IEC-2003 equation (Eq. (2.5)).

2.1.5.2 IEC-2003 equation without magnification factor

The experimental results were also compared to a modified version of Eq. (2.5) in which the magnification factor dependent on yaw angle, $(1+0.2\sin^2(2\theta))$, was removed. This relationship is plotted in Figure 2.9 with the experimental data, and it is shown to match quite well. The modified IEC equation is given in Eq. (2.6), where all variables are as described for Eq. (2.5).

$$A_t = D\,(C_{xt1}S_{t1}\cos^2\theta + C_{xt2}S_{t2}\sin^2\theta) \tag{2.6}$$

While Eq. (2.6) appears to match the wind tunnel data quite well for this particular cross-arm geometry, this is partially due to the lower drag coefficient measured for wind onto the broad face of the cross-arm than was used in the code calculations. This difference likely varies depending on cross-arm geometry, and should be investigated through further wind tunnel testing on numerous cross-arm sections to assess whether there is a significant trend.

2.1.5.3 Alternative to the IEC-2003 approach

Rather than referencing the IEC-2003 approach for the calculation of wind loads on lattice structures, the transverse and longitudinal force expressions in ASCE-74 could be used to form a vector resultant wind load prior to decomposition into the transverse and longitudinal directions. This method, while similar to the IEC-2003 approach, does not

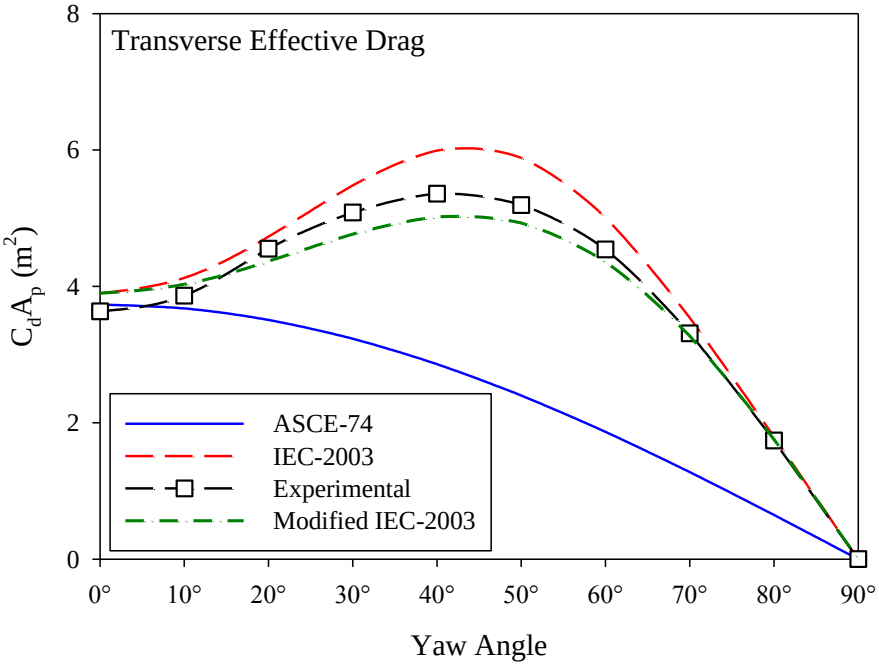

Figure 2.9. Transverse effective drag for the cross-arm showing modified IEC calculation of wind loads.

include the magnification factor at the beginning of Eq. (2.5) and is based purely on the vector addition of wind loads. The effective drag in the net, transverse and longitudinal directions based on this method (referred to as ASCE vector resultant) and the existing ASCE-74 method (referred to as ASCE orthogonal) are compared in Figure 2.10, which shows that the transverse and longitudinal effective drag calculated using the ASCE vector resultant is very similar to that calculated using IEC-2003. The corresponding set of equations is given in Eq. (2.7) for the drag forces on a tower, where all variables are described for Eqs. (2.4a) and (2.4b).

$$F_d' = B\left((C_{ft}A_{mt}\cos(\psi))^2 + (C_{fl}A_{ml}\sin(\psi))^2\right)^{1/2} \quad (2.7a)$$

$$F_t' = BF_d'\cos(\psi) \quad (2.7b)$$

$$F_l' = BF_d'\sin(\psi) \quad (2.7c)$$

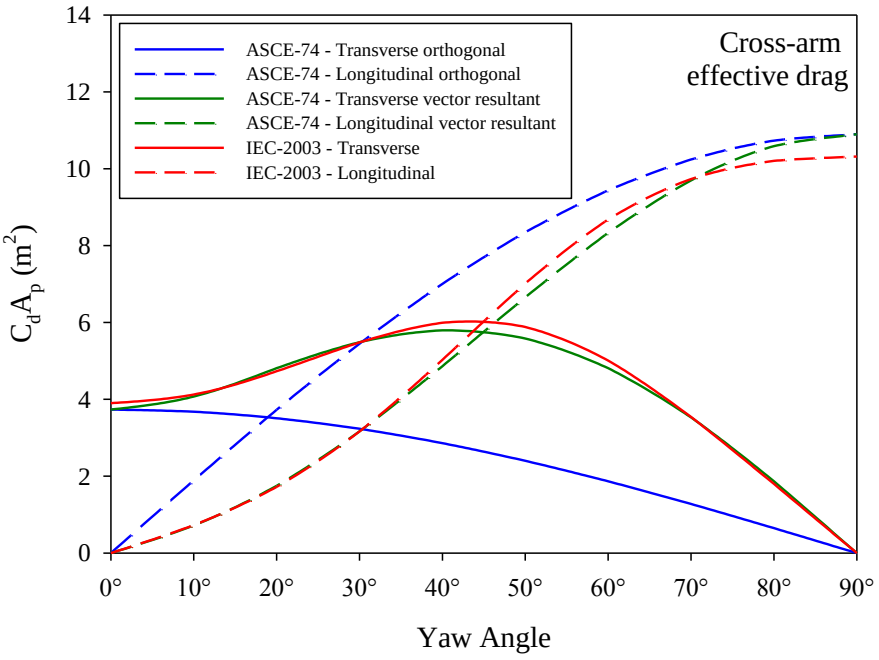

Figure 2.10. Comparison of the ASCE vector resultant approach to the existing (orthogonal) ASCE-74 approach.

2.1.5.4 Implication on complete tower loading

Up to this point, the cross-arm has been the only portion of the tower considered. It is acknowledged that while improved methods are suggested for the assessment of the cross-arm wind loads (and for other sections characterized by unique shapes and aspect ratios), this may have little impact on either the overall loads on a complete tower or the design case (i.e., when heavily-loaded lines are included in the calculation). However, this will vary with tower design (i.e., cross-arm to total tower area ratio) and deserves further investigation. The effective drag in the transverse and longitudinal directions for the entire tower structure were calculated using the geometric and aerodynamic parameters in Table 2.1 for ASCE-74 and IEC-2003, and the results are plotted in Figure 2.11. If the wind tunnel data for the cross-arm were included in this comparison, the resulting plots would fall between the curves for ASCE-74 and those for IEC-2003, as was illustrated by the comparison of the cross-arm only. A method which incorporates wind tunnel test data with the wind loading equations in codes is discussed by Mara and Ho (2011).

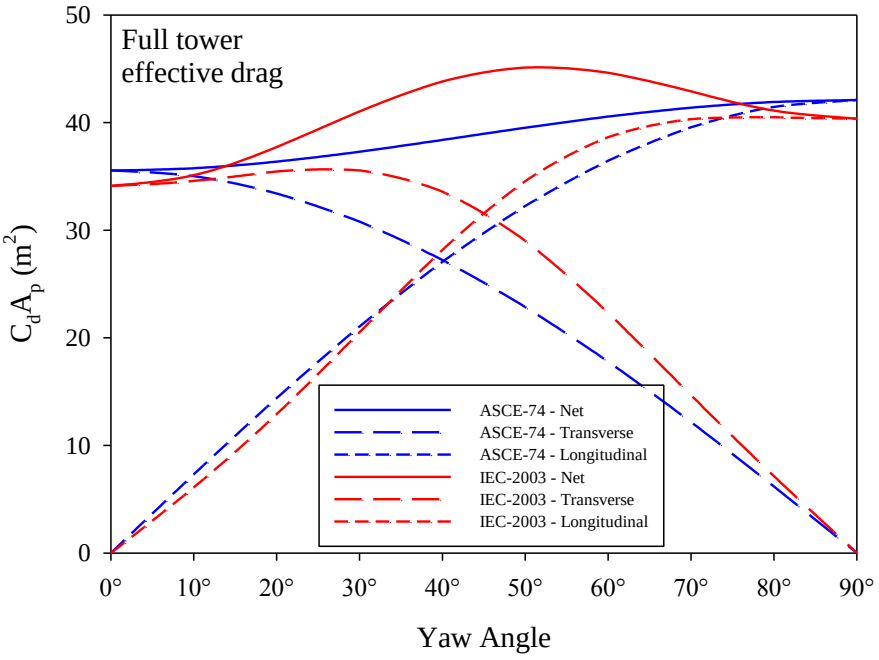

Figure 2.11. Effective drag as calculated using ASCE-74 (blue) and IEC-2003 (red).

The effective drag in the transverse direction is clearly influenced by the number of lines involved, and includes both conductors and ground wires. However, depending on the span between towers and the number of cross-arms in the particular design, the overall effect may not be appreciated until the calculations are carried out. It is prudent to carry out the analysis of the wind loads on the tower structure as accurately as possible, before it is assumed that the differences between the calculation procedures presented earlier are negligible. It is therefore suggested that an alternative approach for the calculation of wind loads on the tower structure be used in favor of the current procedure in ASCE-74.

2.1.6 Conclusions and recommendations

Wind tunnel test data for a cross-arm section model of a prototype guyed transmission tower was used to assess the relationship of the drag wind loads to yaw angle. The experimental data were compared to the calculations for the section based on ASCE-74 and IEC-2003. Recommendations regarding the use of an alternative method of wind load calculation, especially for sections which are notably different in the transverse and longitudinal planes, were made. The following conclusions are drawn from the study:

1. Good agreement was found between the experimental data for the cross-arm section and the recommended values in the codes for the drag coefficient in the transverse direction. However, for the longitudinal direction (i.e., when the broad face of the cross-arm is fully exposed), the experimental values indicate a lower drag coefficient than suggested by both ASCE-74 and IEC-2003. This difference is expected to vary among cross-arm geometries, and is likely related to the non-uniform distribution of members. Note that the recommended drag coefficients in ASCE-74 are not intended to be used for portions of towers such as cross-arms or bridges.

2. The procedure used to calculate the transverse wind load in ASCE-74 results in a lower value for oblique wind directions than suggested by the wind tunnel data. This is due to the maximum transverse wind load occurring at a yaw angle of 0° in ASCE-74, while at a yaw angle of approximately 40° for the wind tunnel data. The shape of the experimental effective drag to yaw angle relationship is similar to that suggested by IEC-2003, although the magnitude of the measured drag is lower. This aspect is related to the difference in the drag coefficient for the longitudinal face noted in the above conclusion.

3. It is recommended to use an alternative method in place of the existing ASCE-74 method for the calculation of wind loads on lattice towers, which is especially pertinent to sections such as cross-arms or bridges. The following alternatives are suggested based on the comparison between wind tunnel data for the cross-arm section and the considered design procedures. Ideally, the same approach would be used for all components of the tower for consistency.

i) The IEC-2003 method of calculation of wind loads for lattice frames be reinstated in ASCE-74, at least for the calculation of wind loads on sections which have significantly different geometric and aerodynamic parameters, or aspect ratios, in the transverse and longitudinal directions. These types of sections include cross-arms and bridges.

ii) The calculation of the vector resultant wind load (as calculated from the existing expressions for transverse and longitudinal forces in ASCE-74) on each section is carried out prior to decomposition into transverse and longitudinal

forces. This accounts for differences that may exist between the transverse and longitudinal planes in a more correct fashion, while maintaining the load calculations currently specified in ASCE-74.

2.2 Influence of solid area distribution on the drag coefficient of lattice frames

Many wind design codes provide recommended values of the drag coefficient for lattice frame geometries based on solidity ratio. The solidity ratio of a lattice structure often varies along its length or height, resulting in a piecewise treatment in design. An example of this is the tower described in Table 2.1. By definition, the solidity ratio is only dependent on the amount of solid area to total enclosed area of a frame and therefore does not account for member spacing or the arrangement of members within the frame. This has implications for some non-uniform sections used in lattice tower design. Drag coefficients for many geometric configurations of a 2-D frame were measured in a wind tunnel with the focus placed on configurations having an identical solidity ratio but different member spacing ratios. It was observed that the drag coefficient varied with member spacing ratio as well as the number of members in the frame. The results suggest that solidity ratio alone may not be sufficient for describing the drag coefficient of a lattice frame having non-uniform solid area distribution. Recommendations are made for future research in this area, which may lead to a better estimate of the drag coefficient for non-uniform lattice sections.

2.2.1 Background

Many wind design codes provide recommended values for the drag coefficient of generic 2-D and 3-D lattice frames under various angles of attack; these values are based on a vast array of experimental work investigating the aerodynamics of 2-D and 3-D lattice frames. Most experiments focus on two key parameters: the section geometry and the solidity ratio. Section geometries which have been commonly investigated include a wide range of 2-D frame designs, as well as square and triangular 3-D truss configurations. Single lattice frames and trusses are used for structures such as support framework (i.e., traffic signs), advertising billboard supports, and exposed bridge trusses.

The latter is the focus of many early studies which contributed to the understanding of the relationship between the solidity ratio and drag coefficient for 2-D frames and trusses (Flachsbart 1935, Biggs 1954, Pagon 1958). 3-D lattice frames are primarily used for communication and transmission towers, and many studies have been directed at assessing the design parameters relevant to these utilities (e.g., Cohen 1957, Clow 1978, Whitbread 1979, Bayar 1986, Carril Jr. et al. 2003, Mara et al. 2010). Aerodynamic characteristics (i.e., drag coefficient, shielding) of 3-D frames have also been studied via experiments on open-frame buildings (Georgiou and Vickery 1979, Kopp et al. 2010).

The force coefficients for open signboards and 2-D frames having flat-sided members specified in ASCE 7-10 (ASCE 2010b) are based on refinements to the work of Pagon (1958) and have remained unchanged since ASCE 7-88 (ASCE 1990). The corresponding force coefficients specified in NBCC 2010 (NRCC 2010) are based on the findings of the Swiss Association of Engineers and Architects (SIA 1956), which is also referenced in more recent versions of ASCE 7. While the SIA document comprises some of the most thorough work performed on configurations of lattice frames, it is noted in both ASCE 7 and NBCC that the results should be used with caution, as the experimental work was carried out under mean velocity and turbulence characteristics which were not representative of wind conditions in the lower atmospheric boundary layer. The drag coefficients specified in codes for 2-D and 3-D lattice frames would benefit from further investigation, including configurations characterized by non-uniform member spacing.

The solidity ratio is an important aerodynamic parameter which indicates the ratio of total solid area (net area) to total enclosed area (gross area) of a lattice frame. The drag force on a lattice frame is controlled by the size of the members and their spacing, which is conveniently expressed as a solidity ratio to circumvent the many combinations of geometry found in various designs. The solidity ratio of a lattice frame is defined in Eq. (2.2). As the solidity of a frame is increased, more of the wind flow is deflected due to the presence of additional member area. If the members become more tightly spaced, the wind is forced to accelerate between the members; this contributes to an increase in the drag load on the structure. In the case of 3-D lattice frames, the drag coefficient and

corresponding net area for each face are often used to calculate the wind loads on the section (ASCE 2010a).

Experiments in the literature have traditionally been conducted in a systematic manner to evaluate the drag coefficient for various member geometries over a range of solidity ratios; these have provided empirical expressions for the drag coefficient as a function of solidity ratio for generic lattice frame and tower configurations (e.g., SIA 1956). Continuous relationships for the drag coefficient as a function of solidity ratio are available in many wind loading codes (e.g., ASCE 7-10, NBCC 2010, AS/NZS 1170.2) and technical provisions (ASCE-74, ESDU Data Item No. 81027). However, there are two underlying assumptions inherent to the recommended drag coefficients in the above references: i) that the frame geometry is consistent over a sufficient span; and ii) that the solidity ratio is independent of member spacing ratio. These assumptions are a product of most experiments being carried out on section models in order to establish mean aerodynamic coefficients without involving end effects. As a result, the provisions in most wind loading codes and guidelines are likely to be quite representative of most typical frames (i.e., truss configurations) having a consistent distribution of solid area and uniform member spacing ratio. The calculation of solidity ratio does not reflect whether the solid area is acting as a single member or multiple independent members.

In reality, structures are often comprised of many sections having varying geometry over their length or height. Codes and guidelines on the assessment of wind loads on tower structures (ASCE-74, AS/NZS 1170.2, CSA-2010) recommend a piecewise approach in which the tower is partitioned into a number of sections, typically referred to as panels (see Figure 2.2). Each panel ideally has a reasonably consistent geometry along its span, and therefore reasonably consistent aerodynamic coefficients. However, the distance between members at lower levels of frames or towers tends to be much greater than at upper levels due to efficient design techniques. These geometric characteristics result in some panels of the frame or tower having very few members over a very large total enclosed area. This also results in a much greater number of members in a relatively small enclosed area in the upper levels of most towers, or sections where there are

significant differences in member spacing (i.e., the cross-arm of a lattice transmission tower).

The objective of the work presented in this portion of the chapter is to assess whether the solidity ratio is an appropriate sole parameter for estimating the drag coefficient of a frame based on the approach taken by most codes, and to provide recommendations for future research regarding lattice structures having a non-uniform distribution of solid area. That is, to determine whether the distribution (with respect to member spacing ratio and number of members) of solid area within a frame has an influence on the behavior of the drag coefficient. This has a direct impact on the methods which are currently in use for the estimation of wind loads on lattice structures having geometries with non-uniform member spacing, such as the cross-arm and bridge sections of some transmission tower designs.

It is acknowledged that the member arrangements and spacing ratios investigated in the current set of experiments differ from the member arrangements in typical frame design. The basic member geometry considered in this chapter was selected in order to illustrate the important parameters associated with assessing the drag coefficient in terms of solidity ratio for sections having non-uniform member spacing, before proceeding with experiments on sections characterized by complex 3-D geometry such as those in lattice transmission towers. Recommendations are made later for the progression of research towards a better estimate of the drag coefficient for more complex geometries.

2.2.2 Wind tunnel experiment

Wind tunnel testing was used to assess the influence of solid area distribution (via member spacing ratio) on the drag coefficient of a 2-D frame. A model was constructed which allowed for an efficient placement and removal of solid members within the enclosure of the frame. Different model configurations having the same solidity ratio are shown in Figure 2.12, and the experimental configurations are listed in Table 2.2. The solidity ratio of the frame is calculated as it would be if typical wind design codes were used; that is, the outer boundaries of the frame are used to define the gross area. The empty frame is characterized by a solidity ratio of 9.3% based on the area enclosed by the

outside dimensions (0.4572 m by 0.4572 m). Each member used to adjust the solidity of the model was a flat rectangular piece of brass having dimensions of 0.0254 m by 0.4572 m exposed to the wind and a thickness of 2 mm. The addition of each member to the frame results in an increase in solidity ratio of 5.4% based on the outside dimensions of the frame. The member spacing ratios investigated were related to the width of the members, such that *w* represents 0.0254 m. Member spacing ratios of *w*, 3*w* and 4*w* were considered, as well as the case where there was no spacing between members. The latter case, when the entire frame is populated, represents a flat plate and provides an upper bound comparison with experimental data in the literature.

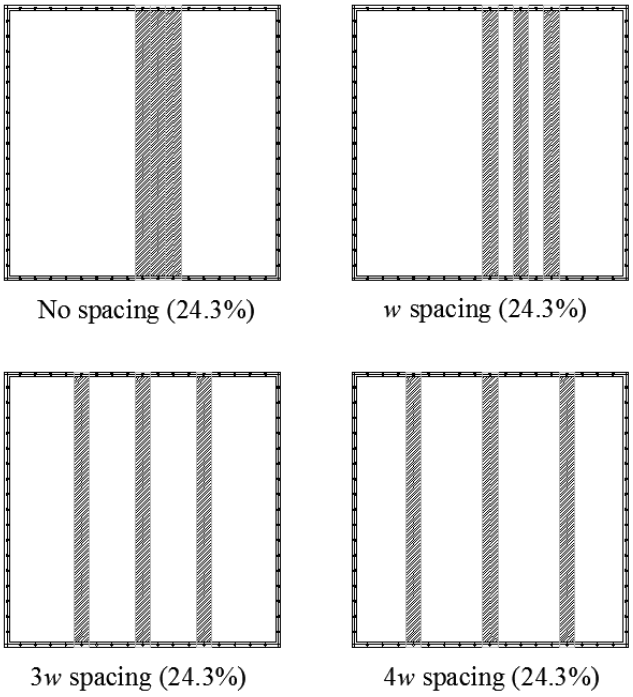

Figure 2.12. Examples of configurations with consistent solidity ratio of 24.3% (clockwise from top left: configurations 3, 19, 35, 31).

Table 2.2. List of experimental configurations for the 2-D frame.

Spacing	Configuration	Solidity (%)	Spacing	Configuration	Solidity (%)
Frame	0	9.3			
	1	14.3		19	24.3
	2	19.3		20	29.4
	3	24.3		21	29.4
	4	29.4		22	34.4
	5	34.4		23	34.4
	6	39.4	***w***	24	39.4
	7	44.4	**spacing**	25	39.4
	8	49.4		26	44.4
No	9	54.5		27	44.4
spacing	10	59.5		28	49.4
	11	64.5		29	54.5
	12	69.5		30	59.5
	13	74.5		31	24.3
	14	79.6	**3*w***	32	29.4
	15	84.6	**spacing**	33	34.4
	16	89.6		34	39.4
	17	94.6	**4*w***	35	24.3
	18	100	**spacing**	36	29.4

The wind tunnel experiments were conducted in Tunnel II at the Boundary Layer Wind Tunnel Laboratory at the University of Western Ontario. A photo of the experimental set-up showing the model, support strut and pitot tube arrangement is shown in Figure 2.13. The tunnel dimensions at the test section are 3.5 m by 2.5 m, which resulted in a maximum blockage ratio of approximately 2.5%; no correction for blockage was applied. The frame was supported in uniform turbulent flow by a strut housing a force balance load cell located at the center of the base of the frame, and the turbulence intensity was approximately 10% over the dimensions of the model. The mean wind speed was approximately 6.1 m/s (as measured by the model height pitot), which resulted in a Reynolds number of approximately 10^4 based on the smallest dimensions of the model. The Reynolds number satisfies the criterion in ASCE 49-12 (ASCE 2012) for wind tunnel testing of sharp-edged bodies. Moreover, the drag coefficient for flat plates has been shown to be consistent for Reynolds numbers exceeding 10^3 (Hoerner 1965). Drag force measurements were averaged over a sample time of 90 seconds at 100 Hz, and each

configuration was tested twice to assess repeatability and accuracy. The differences between repeated experiments were found to be negligible for all configurations.

Figure 2.13. Photo of 2-D frame in the wind tunnel (configuration 30 shown).

2.2.3 Results and discussion

The mean drag force is plotted as a function of solidity ratio for each configuration in Figure 2.14. The measurement of the drag on the empty frame is indicated as the first point on the plot (9.3% solidity). It is clear that the drag force increases linearly with increasing solid area; this behavior was expected. In the case of solidity ratios which were tested more than once (e.g., configurations 20 and 21), the mean drag force was found to agree within 2%. The slope of the mean drag force with solidity ratio increases as the member spacing ratio increases from no spacing to *w* spacing; this is likely explained by the increased drag force on the frame due to the acceleration of the wind through the gaps between members. There is again an increase in the slope of the drag force with solidity as the member spacing ratio increases from *w* to 3*w*. The differences between the 3*w* and 4*w* member spacing arrangements are negligible over the range of solidity ratio tested, which suggests that at spacing ratios greater than 3*w* there is little

interaction of the wind flow around each of the members. In other words, the gaps have reached a size where the flow can pass through relatively unaffected by the flow around the adjacent member. The mean drag force is greater for configurations where there are a greater number of members acting independently.

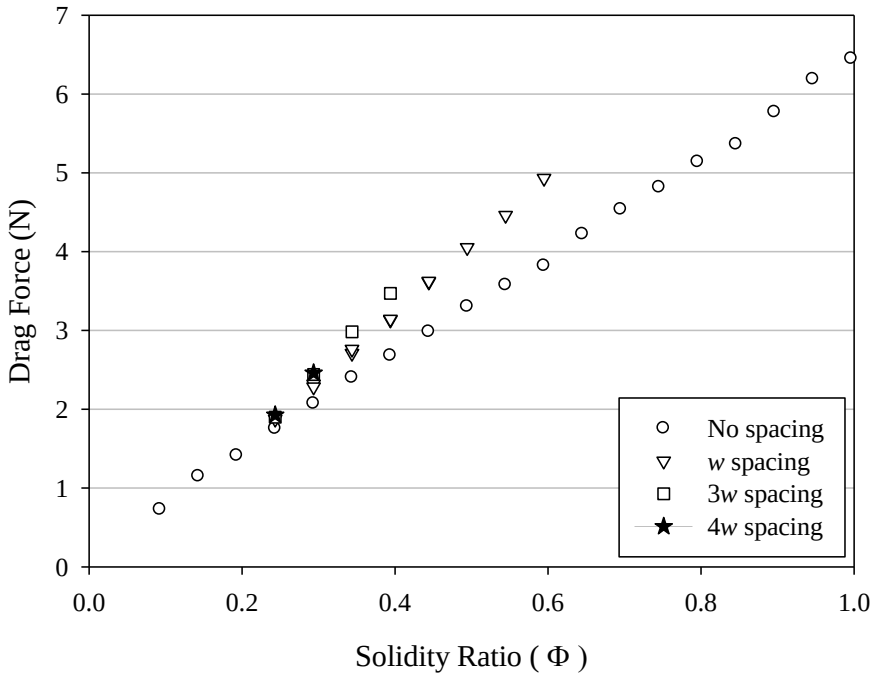

Figure 2.14. Mean drag force as a function of solidity ratio for various member spacing ratios.

The variation of the drag coefficient with respect to solidity ratio is plotted for each member spacing ratio in Figure 2.15. In each case, the solidity ratio was calculated based on the total enclosed area of the frame. Recommendations of the drag coefficient for open signs and lattice framework based on ASCE 7-10 (ASCE 2010b) are indicated by the dashed lines, and the ASCE 7-10 recommendation for a solid freestanding sign having aspect and clearance ratios consistent with the experiment is also included. ASCE 7 had previously recommended a drag coefficient of 1.2 (up to ASCE 7-02 (ASCE 2002)) for solid freestanding walls and signs, however this was based on experimental data measured under smooth flow conditions (e.g., Bearman 1971). As of ASCE 7-05, the recommendations for freestanding walls and signs were adjusted based on experiments carried out by Holmes (1986) and Letchford (2001) in boundary layer wind tunnels,

which better represented the turbulence characteristics of the atmospheric boundary layer close to ground level. The drag coefficient measured by Letchford (2001) for a similar experimental setup is also included in the plot, and shows good agreement with the solid configuration (fully populated frame with no member spacing). The recommended drag coefficient for the ASCE 7-10 solid sign is significantly greater than that measured in the experiment. This may be due to the expectation of a higher level of turbulence intensity at full-scale (as opposed to the experimental value of approximately 10%), which would lower the base pressure on the leeward face of the wall or signboard due to additional fluid entrainment. As a result, the drag coefficient of the structure is increased; this effect is shown for a flat plate by Bearman (1971).

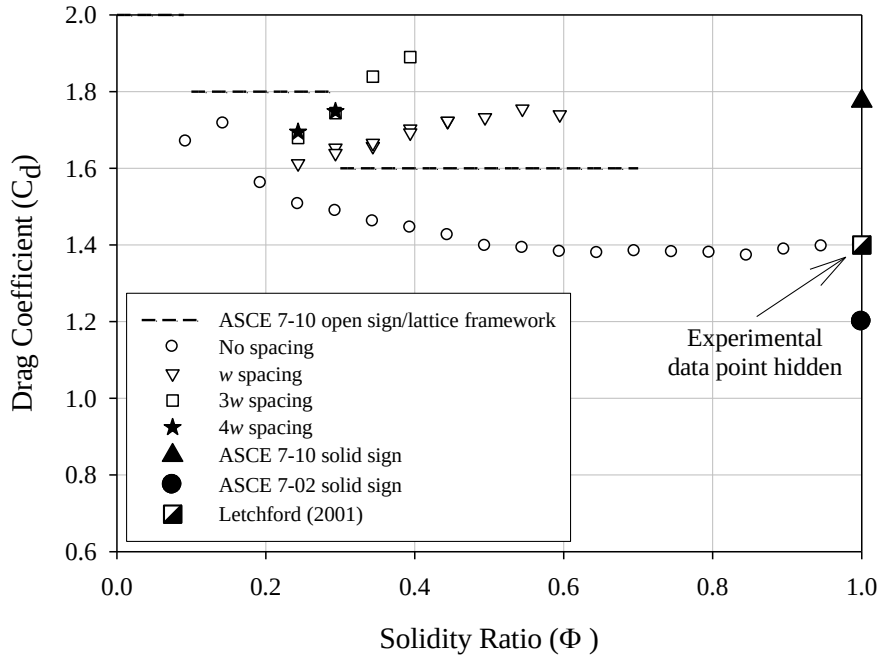

Figure 2.15. Drag coefficient as a function of solidity ratio for various member spacing ratios.

For configurations 3, 19, 31 and 35 (shown in Figure 2.12), the experimental drag coefficients are 1.51, 1.61, 1.68 and 1.69, respectively. Each configuration has an identical solidity ratio as calculated using the traditional definition of gross area. The solid area in configuration 3 is clearly acting as a single member, while interaction in the flow is likely minimal for configurations 31 and 35. For the latter two configurations, the

presence of additional independent members results in approximately a 12% increase in drag coefficient. This deviation from a single member increases with the number of additional members. This suggests that multiple members in the same enclosed area can increase the drag coefficient from that characterized by a section with only a single member. The drag coefficients obtained through the wind tunnel tests suggest that while the coefficients specified in ASCE 7-10 are conservative for sections characterized by a single member, in the case a relatively compact section has many members, the drag coefficient may be under estimated. The greatest increase in the drag coefficient from the no spacing case was observed for a spacing ratio of 3*w* at a solidity ratio of 39.4%, and resulted in approximately a 30% increase in drag.

To this point, the calculation of solidity ratio has been based on the solid area within an enclosed gross area defined by the boundaries of the frame, which reflects the basic approach taken by wind design codes. This approach disregards the spacing between members, or the fact that there may be unpopulated regions within the enclosed area of the frame. The recommended values for drag coefficients in codes are provided for sections which are 'infinitely continuous'; that is, their geometric and aerodynamic properties do not vary along the span of the frame. This implies that the drag coefficient of a frame should be calculated based on a section having sufficient span to provide a stable estimate of the drag coefficient through Eq. (2.1). Figure 2.16 shows the experimental data plotted as a function of number of adjacent members, with the solidity ratio defined entirely by the member spacing such that: 4*w* spacing corresponds to 20% solidity; 3*w* spacing corresponds to 25% solidity; *w* spacing corresponds to 50% solidity; and no spacing corresponds to 100% solidity. Through this approach, the solidity ratio is calculated based on the populated area of the frame, rather than the area defined by the enclosed boundary. It is shown that the drag coefficients for the configurations having 100% and 50% solidity (no spacing and *w* spacing, respectively) approximately converge for 8-10 adjacent members. Convergence for the 25% solidity and 20% solidity configurations (3*w* and 4*w* spacing, respectively) are not observed within the range of the experimental data collected. Most notably, Figure 2.16 shows that the drag coefficient is dependent on the number of adjacent members to a certain point, beyond which the section can likely be considered representative of an infinitely continuous section. These

findings indicate that recommended values for the drag coefficient based on the solidity ratio for infinitely continuous frames (as typically calculated using wind design codes) may not be representative of the drag coefficient of geometries characterized by non-uniform distributions of solid area. This has implications to the design loads for structures containing these types of geometries (i.e., lattice transmission tower cross-arms).

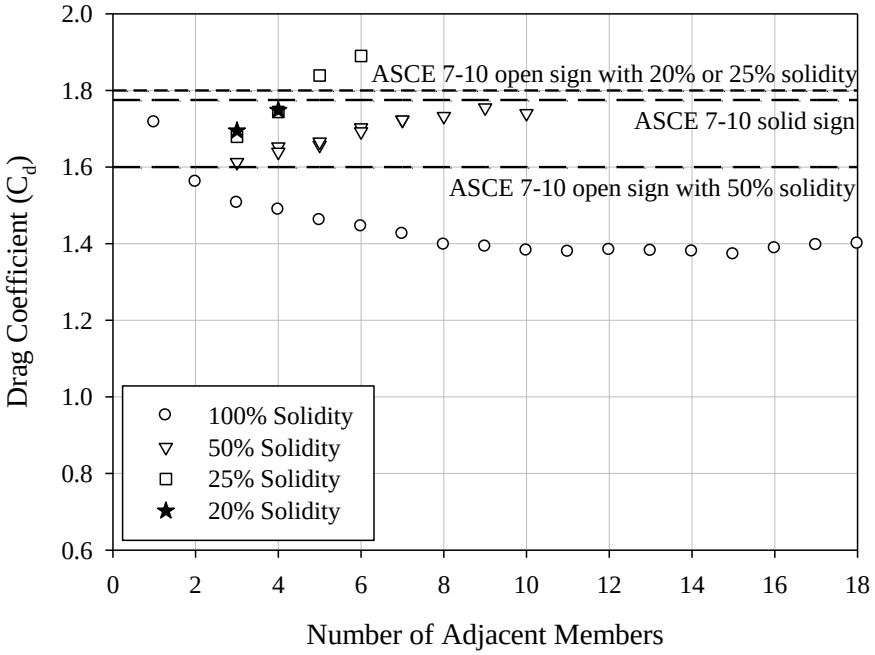

Figure 2.16. Drag coefficient as a function of number of adjacent members for various member spacing ratios.

Results have been presented which indicate that the drag coefficient of a 2-D lattice frame is sensitive to the spacing of the members which populate the interior of the frame. However, the data from this particular experiment may not be entirely representative of common geometries found in frames and towers (i.e. truss configurations). More common geometries should be explored in future work. Nevertheless, differences in the drag force on frames having the same solidity ratio, but different member spacing ratios, were observed. This suggests interaction of the deflected flow passing through the gaps between the members has an effect of the drag coefficient, primarily when the members are close together. The implication of this is that the member spacing ratio is important

for the flow through lattice frames or porous structures, but more work must be carried out to assess the extent of these effects. The results also suggest that a more representative solidity ratio may be calculated if the gross area is not taken as the area enclosed by the outer boundaries of the frame; this is discussed later.

The experimental data indicate differences between member spacing ratios for which the members of the frame act independently rather than as an overall assembly. The aerodynamic coefficients recommended in most wind design codes and provisions are intended to be applied to infinitely continuous frames, and perhaps combined with a factor to account for aspect ratio. Unique lattice geometries, such as those found in cross-arm sections or at the bottom of support frames or self-supported towers, should be treated in a different fashion than for lattice sections comprised of infinitely continuous truss patterns.

2.2.4 Conclusions and recommendations

The mean drag coefficient of a 2-D lattice frame was evaluated for a range of solidity and member spacing ratios. The results for configurations having no spacing indicate that as the solidity ratio increases, the drag coefficient converges to a value of 1.4. This upper bound is in agreement with work carried out by Letchford (2001). The drag coefficient specified in ASCE 7-10 appears to be conservative for configurations where the area acts as a single member. However, for configurations having multiple members with spacing, the experimental drag coefficient exceeds that specified in ASCE 7-10. This effect increases with solidity ratio. The drag coefficient measured for the 3*w* and 4*w* member spacing ratios are quite similar, although they exceed the values measured for the *w* member spacing ratio by 5-11% depending on solidity ratio. The solidity ratios common in lattice frame and tower design range from 10% to 35%, depending on geometry and construction. Differences in the drag coefficient were observed over this range of solidity ratio among various member spacing ratios and number of members; this effect warrants further investigation. It is possible that these differences partially result from the member arrangement in the current experiment when compared to more of a truss-like geometry.

It was observed that the drag coefficient of a 2-D lattice frame varies with member spacing ratio and number of members; this reflects the dependence of the drag coefficient of the frame on a solidity ratio characterized by uniform member spacing. In reality, lattice frames and towers exhibit varying member spacing ratios along their span or height, or include geometries where the member spacing ratio is non-uniform (i.e., cross-arm sections in transmission towers). However, recommendations for the drag coefficient in wind design codes are a function of solidity ratio only. This approach is suitable for sections having uniform member spacing, and thus a uniform distribution of solid area and drag coefficient. However, if the solid area is not evenly distributed throughout the enclosed area, the drag coefficient will not be consistent for the section. Therefore, current expressions for the drag coefficient based solely on solidity ratio, and how they are applied in wind design codes, over-simplify the problem. While the solidity ratio is unquestionably a primary indicator of drag, an appropriate technique for calculation of the solidity ratio for geometries having non-uniform solid area distribution is not clearly defined. The assessment of the following aerodynamic characteristics of lattice frames would lead to an appropriate technique, and thus a better estimation of the drag coefficient:

1. Identification of the number of members at a defined member spacing ratio that is required to achieve a consistent drag coefficient. This results in a uniform solid area distribution and solidity ratio, and implies that the gross area should be calculated based on the dimensions of the uniform portion of a frame. This is opposed to the gross area defined by the outer boundaries of the frame, as is commonly used when considering geometries having non-uniform member spacing.

2. A relationship describing the difference between: i) the drag coefficient of a geometry based on a fully uniform member spacing (as suggested by Point 1), and ii) the drag coefficient of a geometry meeting the criteria suggested by Point 1, but having additional members spaced at varying ratios (i.e., percent of original spacing). Aerodynamic data would provide a measure of the difference in the drag based on i) and ii), which shows the impact of member spacing on the drag coefficient.

3. The results from Point 2 could be used to adjust the definition of gross area used in the calculation of the solidity ratio to a more appropriate value than would be arrived at using the outer boundaries of the frame. For transmission tower cross-arm geometries, this would lower the considered gross-area, thereby increasing the solidity ratio. If the recommended values of the drag coefficient in codes were then to be used, the selected value would be more representative of a section having a uniform solid area distribution and solidity ratio.

While the experimental work presented here illustrates the issues associated with defining the drag coefficient solely on the solidity ratio, more aerodynamic data needs to be collected to arrive at a better technique for assigning a drag coefficient to geometries characterized by non-uniform distribution of solid area. The points described above may lead to such an improved technique.

2.3 Summary of experimental work

Wind tunnel testing was used to assess the drag wind loads on a cross-arm section as a function of yaw angle, and the results were compared to the expressions in ASCE-74 and IEC-2003 (and therefore also CAN/CSA 2010). Based on the comparison of the experimental data for the cross-arm to the ASCE-74 equations for calculation of the transverse and longitudinal wind loads, it was decided to adopt the IEC-2003 equation for the application of wind loads to the analytical model presented in the remainder of this thesis. The IEC-2003 expression captures a more realistic relationship of drag wind load with yaw angle for all types of lattice sections, while the ASCE-74 equations are more appropriate for sections which are symmetric about both planes. It would appear that any analysis carried out based on the ASCE-74 equations should be regarded with caution.

Differences were observed between the IEC-2003 equation and the experimental drag loads on the cross-arm, which were attributed to a lower experimental drag coefficient being measured for the longitudinal face compared to that specified in IEC-2003. This illustrates a problem associated with defining the drag coefficient by the solidity ratio only. To further understand this issue, wind tunnel tests were carried out on a basic 2-D frame for many configurations with the same solidity ratio but different member spacing

ratios. It was shown that the drag coefficient, as it is defined and applied in wind loading codes, is sensitive to the distribution of solid area. This is an important consideration for portions of the tower which do not have a consistent solidity ratio over the span of the section. Recommendations were made for future experimental work that should be carried out to better define the drag coefficient for this class of tower sections.

2.4 Acknowledgements

The author is grateful for the financial support received from the National Sciences and Engineering Research Council of Canada (NSERC). Acknowledgement is given to Manitoba Hydro, NSERC, CEA Technologies Inc. (CEATI), and the Institute for Catastrophic Loss Reduction (ICLR) for providing financial support towards the wind tunnel testing component of the cross-arm study. The author is appreciative to Mr. R.T. Edey for supporting and making resources available for the 2-D frame experiments. Many useful discussions with Drs. J.K. Galsworthy, T.C.E. Ho, G.A. Kopp and R. Behncke were of great benefit to the author. Constructive feedback received from the ASCE Task Committee on Electrical Transmission Line Structural Loading (of which the author is a member) is also appreciated.

2.5 References

American National Standards Institute (ANSI). (1982). Minimum design loads for buildings and other structures. ANSI Standard A58.1-1982, New York, USA.

ANSI. (2006). Structural standard for antenna supporting structures and antennas. ANSI Standard TIA-222-G, Telecommunications Industry Association, Arlington, VA, USA.

American Society of Civil Engineers (ASCE). (1990). "Minimum design loads for buildings and other structures." ASCE Standard 7-88. ASCE, New York, USA.

ASCE. (1991). Guidelines for electrical transmission line structural loading. ASCE Manuals and Reports on Engineering Practice No. 74 (2nd edition), ASCE, New York, USA.

ASCE. (2002). "Minimum design loads for buildings and other structures." ASCE Standard 7-02. ASCE, New York, USA.

ASCE. (2010a). Guidelines for electrical transmission line structural loading. ASCE Manuals and Reports on Engineering Practice No. 74 (3rd edition), ASCE, New York, USA.

ASCE. (2010b). "Minimum design loads for buildings and other structures." ASCE/SEI Standard 7-10. ASCE, New York, USA.

ASCE. (2012). "Wind tunnel testing for buildings and other structures." ASCE/SEI Standard 49-12. ASCE, New York, USA.

Bayar, D.C. (1986). "Drag coefficients of lattice structures". *J. Struct. Eng*., 112(2), 417-430.

Bearman, P.W. (1971). "An investigation of the forces on flat plates normal to a turbulent flow." *J. Fluid Mech*., 46(1), 177-198.

Biggs, J.M. (1954). "Wind loads on truss bridges." *Trans. Am. Soc. Civil Eng*., 119, Paper No. 2702, 879-898.

Canadian Standards Association (CSA) (2010). Design criteria of overhead transmission lines. CAN/CSA-C22.3 No. 60826-10, CSA, Toronto, Canada.

Carril Jr., C.F., Isyumov, N. and Brasil, R.M.L.R.F. (2003). "Experimental study of the wind forces on rectangular latticed communication towers with antennas." *J. Wind Eng. Ind. Aerodyn*.,91(8), 1007-1022.

Clow, D.G. (1978). "Loads on open lattice structures: a comparative study." *Proc. 3rd Coll. Wind Eng*., Aachen, Germany, 1, 165-177.

Cohen, E. (1957). "Design of multi-level guyed towers: wind loading." *J. Struct. Div*., 83, Paper No. 1355.

de Oliveira e Silva, A., de Medeiros, J.C.P., Loredo-Souza, A.M., Rocha, M.M., Rippel, L.I., Carpeggiani, E.A. and Núñez, G.J.Z. (2006). "Wind loads on metallic latticed transmission line towers." CIGRÉ 2006 Proceedings, Paris, France.

Engineering Science Data Unit (ESDU). (1982). "Lattice structures, Part 1: Mean fluid forces on single and multiple plane frames." ESDU Data Item No. 81027, ESDU, London.

International Electrotechnical Commission (IEC) (2003). Design criteria of overhead transmission lines. IEC Standard 60826:2003, 3rd edition.

Flachsbart, O. (1935). "Winddruck auf vollwandige bauwerke und gitterfachwerke." *Publ. Int. Assoc. Bridge Struc. Eng*., 1, 153-172.

Georgiou, P.N. and Vickery, B.J. (1979). "Wind loads on building frames." *Proc. 5th Int. Conf. Wind Eng*., Fort Collins, CO.

Hangan, H., Savory, E., El Damatty, A., Galsworthy, J. and Miller, C. (2008). "Modeling and prediction of failure of transmission lines due to high intensity winds." *Proc. 2008 Structures Congress (ASCE)*, Vancouver, BC, Canada.

Hoerner, S.F. (1965). "Fluid-dynamic drag." Hoerner Fluid Dynamics, Vancouver, WA, USA.

Holmes, J.D. (1986). "Wind tunnel tests on free-standing walls at CSIRO." CSIRO Division of Building Research, Internal Rep. 86/47.

Kopp, G.A., Galsworthy, J.K. and Oh, J.H. (2010). "Horizontal wind loads on open-frame, low-rise buildings." *J. Struct. Eng.*, 136(1), 98-105.

Letchford, C.W. (2001). "Wind loads on rectangular signboards and hoardings." *J. Wind Eng. Ind. Aerodyn*., 89(1), 135-151.

Mara, T.G. (2007). "The effects of multi-directional winds on lattice sections." M.E.Sc. Thesis, University of Western Ontario.

Mara, T.G. (2013). "Influence of solid area distribution on the drag of a 2-D lattice frame." *J. Eng. Mech.*, doi: 10.1061/(ASCE)EM.1943-7889.0000681.

Mara, T.G. and Galsworthy, J.K. (2011). "Comparison of model-scale and full-scale wind tunnel test results for a typical 3-dimensional lattice frame". *Proc. 13th International Conference on Wind Engineering*, IAWE, Amsterdam, the Netherlands.

Mara, T.G. and Ho, T.C.E. (2011). "Design loads for transmission towers under skewed wind loading." *Proc. 2011 Structures Congress*, ASCE, Las Vegas, NV.

Mara, T.G., Galsworthy, J.K. and Savory, E. (2010). “Assessment of vertical wind loads on lattice framework with application to thunderstorm winds.” *Wind Struct*., 13(5), 413-431.

McCarthy, P. and Melsness, M. (1996). “Severe weather elements associated with September 5, 1996 hydro tower failures near Grosse Isle, Manitoba, Canada.” Environment Canada, Winnipeg, Canada.

NESC. (2006). National Electrical Safety Code. ANSI C2. IEEE, Piscataway, NJ.

National Research Council Canada (NRCC).(2010). National Building Code of Canada 2010, Canadian Commission of Building and Fire Codes, Ottawa, ON.

Pagon, W.W. (1958). “Wind forces on plate girders and trusses.” *J. Struct. Div*., 84, Paper No. 1711, 1-27.

Schweizerischer Ingenieur und Architekten Verein (Swiss Association of Engineers and Architects) (SIA). (1956). “Normen fur die Belastungsannahmen, die Inbetriebnahme und die Uberwachung der Bauten (Standards for load assumptions, acceptance and inspection of structures).” SIA Technische Normen No. 160, Zurich, Switzerland.

Standards Australia (2011). “Structural design actions Part 2: Wind actions.” Australian/New Zealand Standard, AS/NZS 1170.2:2011.

Sykes, D.M. (1981). “Lattice frames in turbulent airflow”. *J. Wind Eng. Ind. Aerodyn*., 7(2), 203-214.

Whitbread, R.E. (1977). “Wind loading on lattice towers.” Report on Project Number P352003, National Maritime Institute, UK.

Whitbread, R.E. (1979). “The influence of shielding on the wind forces experienced by arrays of lattice frames.” *Proc. 5th International Conference on Wind Engineering*, IAWE, Fort Collins, CO.

Chapter 3

3 Comparison of capacity assessment methods for a lattice transmission tower

The nonlinear inelastic force-deformation relationship, or capacity curve, for a structure can be used to identify the incipient of yield (yield capacity) and incipient of collapse (maximum or ultimate capacity). Two commonly-used techniques for the assessment of capacity through nonlinear inelastic response are the incremental dynamic analysis (IDA) and nonlinear static pushover (NSP) methods. Estimates of the maximum capacity, typically including the effects of material uncertainty, are important for the calculation of structural reliability. Previous work has been carried out which assesses the capacity curve of a 2-D self-supported transmission tower under various types of wind loading, and compares the results from the IDA and NSP methods. The NSP method was found to approximate the IDA results, for which the capacity estimates vary depending on the stochastic time history of the wind applied to the structure. However, the NSP method applies a constant wind loading profile with time, and assumes a fully coherent loading profile; that is, the NSP method does not account for the effect of fluctuations about the mean wind speed or the coherent structure of the wind. In this chapter, fluctuating time histories of the wind speed over the height of the tower are developed using the auto-regressive moving average (ARMA) technique, incorporating the Kaimal spectrum and Davenport coherence function to describe the characteristics of longitudinal turbulence. The fluctuating time histories of the wind are applied to a 3-D numerical model of a self-supported lattice transmission tower, and the analysis considers nonlinear inelastic geometric and material properties. The effects of different samples of wind time histories on the capacity curve are examined for three wind directions. A comparison between the capacity curve obtained using a 1-minute time history and that obtained using a 5-minute time history is presented to show the effects of duration on the capacity curve of the tower. The resulting capacity curves obtained using the IDA method are compared to that developed using the NSP method, which indicates good agreement between the methods for this type of structure.

3.1 Introduction

Overhead electrical transmission systems are critical infrastructure for the transmission and distribution of electrical power. The primary environmental load considered in the design of transmission structures is the wind load, although the ice loads may govern design for cold regions. The discussion in this thesis is limited to wind loading. Requirements for wind loading on overhead transmission lines are specified in CSA C22.3 No. 60826-10 (CSA 2010), which adopts the International Electrotechnical Commission (IEC) Standard 60826:2003 (IEC 2003). The codes and guidelines assume a linear elastic response under wind loading and do not discuss the inelastic behavior of transmission towers. As a result, nonlinear inelastic analysis for transmission towers is not frequently carried out in design practice, but is necessary for the assessment of ultimate behavior and the estimation of structural reliability.

The nonlinear inelastic responses can be used to establish the force-deformation relationship of a structure, often referred to as the capacity curve, as well as to identify the incipient of yield and of collapse. The capacity curve of the tower represents the relationship between the total base shear force (which is equivalent to the applied horizontal wind force if inertia forces are negligible) and the displacement of the tip of the tower. In the following sections, two commonly-used nonlinear analysis techniques, namely the incremental dynamic analysis (e.g., Vamvatsikos and Cornell 2002) and the nonlinear static pushover analysis (e.g., Krawinkler and Seneviratna 1998), are explained in the context of responses to wind load. The techniques are used to estimate the capacity curve and the incipient of yield and of collapse of a self-supported lattice transmission tower, and the resulting capacity curves are compared. For the structural analysis of the tower, the transverse direction (perpendicular to the wires), the longitudinal direction (parallel to the wires), and an oblique wind direction (wind at 45° to the tower) are considered, and the choice of ordinates which comprise the capacity curves is discussed. Analyses are carried out for 1-minute and 5-minute samples of fluctuating wind in order to assess the effect of duration on the capacity curve.

.

3.2 Analysis procedure, modeling and wind load

3.2.1 Nonlinear static pushover analysis

The nonlinear static pushover (NSP) analysis method is a commonly-used technique to evaluate the structural capacity of a structure under earthquake loading (e.g., Krawinkler and Seneviratna 1998). The procedure is used to evaluate the nonlinear force-deformation relationship and identify the yield and maximum capacity of a structure by monotonically increasing the applied forces while maintaining a constant loading profile. However, the NSP method is an approximate method and relies on the assumption that the response of a multi-degree-of-freedom (MDOF) system is dominated by its first mode of vibration. In other words, the response of a MDOF system can be adequately approximated by a generalized equivalent single-degree-of-freedom (SDOF) system. Many studies have indicated that the NSP method results in a good approximation of the yield and maximum capacities of MDOF systems (Fajfar and Fischinger 1988, Lawson et al. 1994, Krawinkler and Seneviratna 1998). More recently, the NSP method has been applied to steel lattice towers considering point loading representative of prototype pushover tests (Lee and McClure 2007), wind loading for transmission towers (Banik et al. 2010) and woodframe structures (Lee and Rosowsky 2006), and roof panel uplift under wind load (He and Hong 2012).

In the NSP procedure, the force-deformation relationship of the structure, known as the capacity curve, and the yield and maximum capacities are estimated. An illustration of the capacity curve and the maximum (ultimate) capacity that can be obtained is presented in Figure 3.1. The yield capacity is identified by using the bilinear approximation to the obtained capacity curve.

For the analytical results presented in the current work, the force represents the total (maximum) reacting base shear force. This reacting force equals the total applied horizontal wind load if the NSP is used. If the incremental dynamic analysis (IDA) method, which is described below, is applied, the total maximum base shear force differs from the maximum applied load because of the inertial force. Banik et al. (2010) showed that the capacity curves of a transmission tower estimated using the IDA and

NSP methods are in good agreement if the wind loading profile defined by a typical atmospheric boundary layer is applied in the NSP analysis.

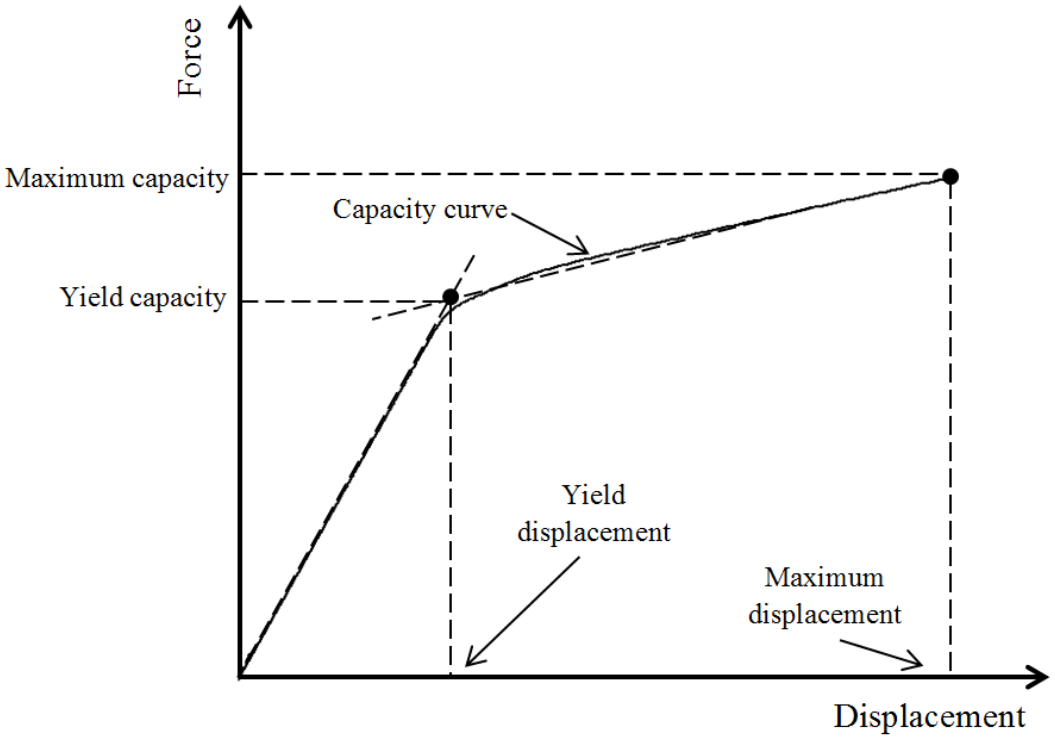

Figure 3.1. Force-deformation or capacity curve for an inelastic system.

3.2.2 Incremental dynamic analysis

The IDA method is commonly used in earthquake engineering to assess the inelastic behavior and capacity of structures under seismic excitations (e.g., Vamvatsikos and Cornell 2002). In the IDA, the ground motion records are scaled and applied to a structure in calculating the elastic and inelastic responses, and to identify the yield and collapse capacities. While historically used for estimation of structural capacity under earthquake, the IDA method was applied to wind loading on a transmission tower by Banik et al. (2010). Important differences which exist between earthquake and wind loading are the presence of the mean wind load and the variation of the wind load along the height of a structure. The application of the IDA for wind loading differs slightly from its application for earthquake loading, and is described in detail by Banik et al. (2010). Through the IDA approach for wind loading, time histories of the total maximum base shear forces and corresponding tip displacements are obtained. The time histories of

the responses are used to establish the capacity curve, and therefore the capacities at incipient of yield and of collapse.

3.2.3 Model of a transmission tower

A self-supported lattice transmission tower design was provided by Manitoba Hydro and modeled in ANSYS® Multiphysics 9.0 (ANSYS 2007). The tower members are modeled using 2-node nonlinear 3-D frame elements, assuming that the multi-bolted moment-resisting connections are rigid in behavior. The masses of the conductors and ground wire are applied as lumped masses to the structure at the nodes corresponding to the wire-structure connections. A 3-D view of the numerical tower model is shown in Figure 3.2. The material nonlinearity of the tower members is modeled using bilinear elastoplastic material properties, and the geometric nonlinearities (e.g., buckling effects) are accounted for through the use of a large deformation analysis. The section properties of the structural members of the tower and wires, along with the nominal dimensions of the structural steel and distribution by panel, are shown in Table 3.1. A total of 959 elements and 405 nodes are used in the modeling of the tower. A modal analysis was carried out on the numerical model, which indicates that the first and second modes of vibration correspond to sway in the transverse and longitudinal directions, respectively. The fundamental frequencies of vibration for the transverse and longitudinal directions are 1.167 Hz and 1.232 Hz, respectively. The third mode of vibration is torsion, having a fundamental frequency of 1.556 Hz. Plots of the first three modes of vibration are shown in Figure 3.3.

3.2.4 Modeling and application of wind loads

Time histories of the fluctuating wind are simulated and used in the IDA to develop the capacity curve for the tower. It was shown in Banik et al. (2010) that the IDA method can be applied to structures under wind loading if the time history scaling takes into account that the wind load spectrum varies with mean wind speed.

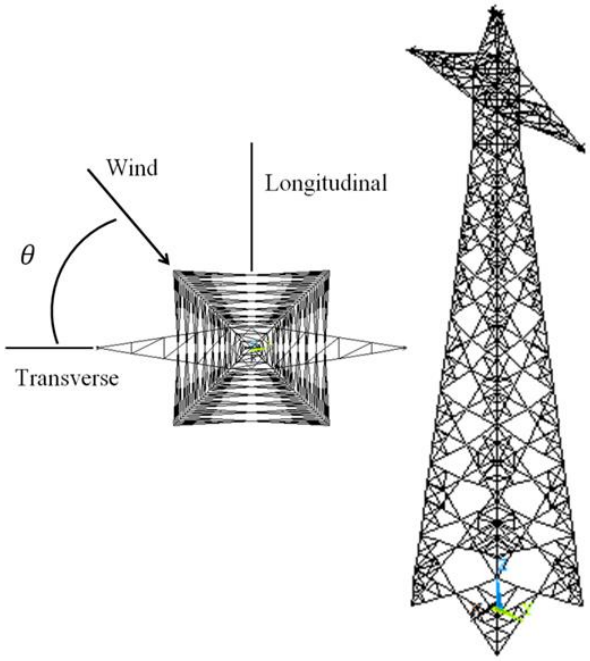

a)

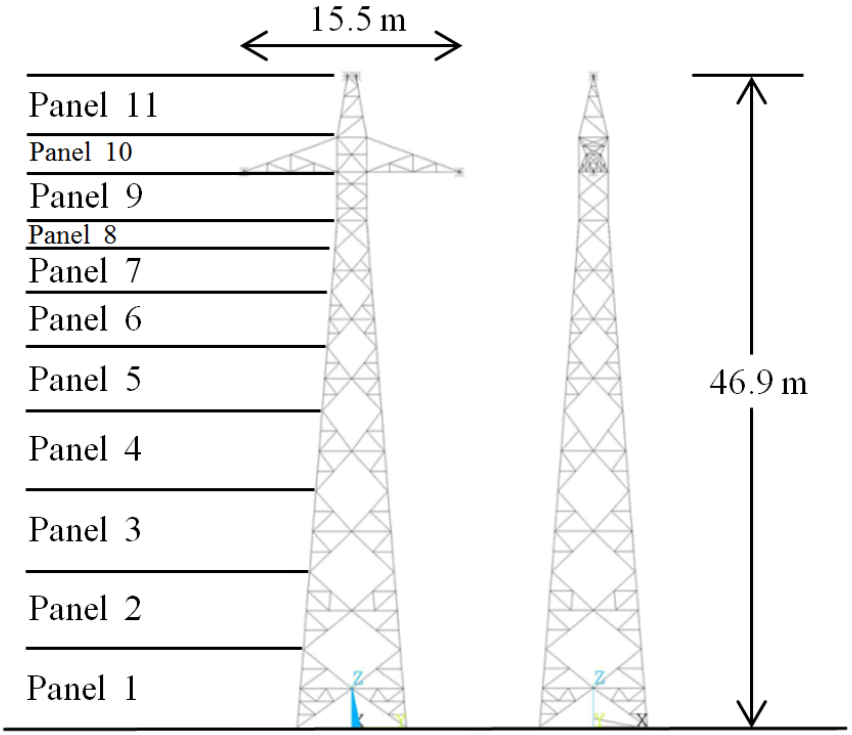

b)

Figure 3.2. Self-supported transmission tower: a) 3-D isometric and plan view, and b) definition of panels for application of wind loads.

Table 3.1. a) Nominal section properties of the structural members of the tower and wires and b) structural steel distribution by panel.

a)

	SI Units (m)		Customary Units (in)		
	Angle	Thickness	Angle	Thickness	Member Key
Chords and Horizontals	0.0445 x .0445	0.125	(1 3/4)" x (1 3/4)"	(1/8)"	a
	0.0445 x .0445	0.375	(1 3/4)" x (1 3/4)"	(3/8)"	b
	0.0508 x 0.0508	0.125	2" x 2"	(1/8)"	c
	0.0508 x 0.0508	0.1875	2" x 2"	(3/16)"	d
	0.0635 x 0.0635	0.1875	(2 1/2)" x (2 1/2)"	(3/16)"	e
	0.0762 x 0.0762	0.1875	3" x 3"	(3/16)"	f
Diagonals and Legs	0.0762 x 0.0762	0.125	3" x 3"	(1/4)"	D1
	0.0889 x 0.0635	0.125	(3 1/2)" x (2 1/2)"	(1/4)"	D2
	0.0889 x 0.0889	0.125	(3 1/2)" x (3 1/2)"	(1/4)"	D3
	0.1016 x 0.1016	0.1875	4" x 4"	(3/16)"	D4
	0.127 x 0.127	0.3125	5" x 5"	(5/16)"	L1
	0.127 x 0.127	0.375	5" x 5"	(3/8)"	L2

b)

	Members in Resisting Direction		Support
Panel	Longitudinal	Transverse	Plan
1	L2, D2, a, c, d	L2, D1, a, c, d	
2	L2, D2, a, b, d	L2, D2, a, b, d	
3	L2, D3, c, e	L2, D2, c, e	
4	L2, D3, a, e	L2, D2, a, e	
5	L1, D3, a, d	L1, D2, a, d	
6	L1, D3, a, b	L1, D2, a, b	
7	L1, D3, a, c	L1, D3, a, c	
8	L1, D4, d	L1, D3, d	
9	D3	D3, a	a
10	D3, e	D3, D4, a, d, f	L1, D1, a, b, d, e
11	a, e	D1, a, b, c	

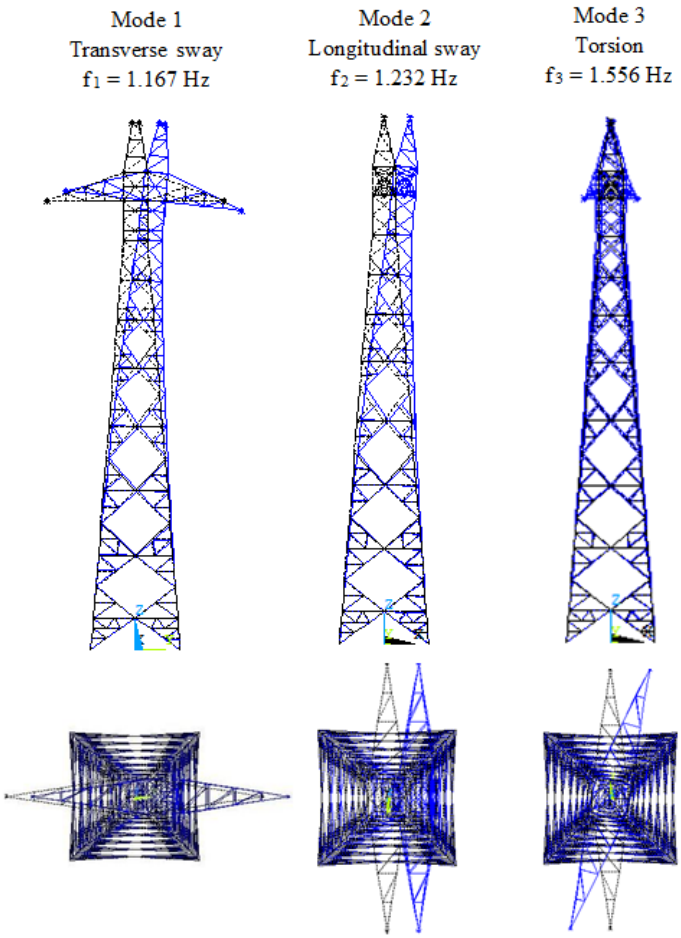

Figure 3.3. Mode shapes and frequencies of the numerical tower model (carried out in ANSYS®).

Assuming the wind speed in the horizontal plane are fully correlated, the drag force at height z and time t, $F(z,t)$, is defined by

$$F(z,t) = 0.5\rho C_d A\overline{V(z)^2}\left(1+\frac{v(z,t)}{\overline{V(z)}}\right)^2 = 0.5\rho C_d A\overline{V(z)^2}(1+I(z)\kappa(z,t))^2 \quad (3.1)$$

where ρ is the density of air (taken as 1.225 kg/m^3 for Canadian sites (CSA 2010)), C_d is the drag coefficient, A is the projected area (at height z) in the plane of the wind, $\overline{V(z)}$ is the mean wind speed at height z, $I(z)$ is the longitudinal turbulence intensity, and $\kappa(z,t) = \frac{v(z,t)}{\overline{V(z)}}$ is the normalized fluctuating wind speed with zero mean and unit variance. The mean wind speed at any height above ground, $\overline{V(z)}$, is defined by the power law for an atmospheric boundary layer (ABL) (Davenport 1964) as

$$\overline{V(z)} = \overline{V_{10\mathrm{m}}} \times (z/10)^{\alpha} \tag{3.2}$$

where z is the height above the ground, $\overline{V_{10\mathrm{m}}}$ is the mean wind speed at 10 m height, and α is the power law coefficient depending on upstream terrain. As all the work was carried out based on open country terrain defined in CSA-2010, α was taken equal to 0.16 (CSA 2010). Note that the loading profile for the NSP method is constant with time, and the loading profile equals the square of the mean wind speed given in Eq. (3.2).

The fluctuating wind speed, $v(z,t)$, is assumed to be a Gaussian stochastic process, which implies $\kappa(z,t)$ is also a Gaussian stochastic process. $\kappa(z,t)$ can therefore be characterized by its power spectral density function, $S(f)$, where f is the frequency in Hz. The power spectral density function of $\kappa(z,t)$ is expressed using Kaimal spectrum with unit variance (Kaimal et al. 1972), defined as

$$S(f) = \frac{22z/\overline{V(z)}}{\left(1+\frac{33fz}{\overline{V(z)}}\right)^{5/3}} \tag{3.3}$$

The coherence function considering the fluctuating wind over height alone, Co, is given as

$$Co\left(z_i, z_j, f\right) = \exp\left(-\frac{fC_z|z_i - z_j|}{0.5\left(\overline{V(z_i)}+\overline{V(z_j)}\right)}\right) \tag{3.4}$$

where C_z is the exponential decay coefficient describing the relative effect of separation in the z direction (over the height), and z_i and z_j are the height of two points (Davenport 1967).

The ARMA algorithm can be applied to fluctuating wind speeds at various heights along a structure (Samaras et al. 1985, Chay et al. 2006, Banik et al. 2010). According to the ARMA algorithm, the normalized fluctuating wind speed at height z and time t is given as

$$\{\kappa(z,t)\} = \sum_{i=1}^{p}[\gamma_i]\{\kappa(z, t - i\Delta t)\} + \sum_{i=0}^{q}[\beta_i]\{\varepsilon_i\} \tag{3.5}$$

where $\{\kappa(z,t)\}$ is an *n*-variate vector of normalized fluctuating wind speed at *n* different heights of the tower for which the fluctuating wind speeds are generated, $[\gamma_i]$ and $[\beta_i]$ are *n* x *n* autoregressive (AR) and moving average (MA) ARMA coefficients, respectively, for the *i*-th time step, Δt is the time interval, p and q are the orders of the AR and MA components, respectively, and $\{\varepsilon_i\}$ is the *n*-variate Gaussian white noise series. For the simulated time histories used in the current work, the time interval (Δt) equal to 0.05 s is considered for a (reference) mean hourly wind speed at 10 m height of 27.8 m/s (100 km/h). As well, equal orders ($p = q = 5$) of the AR and MA components were used. This choice of values for p and q has been shown to produce fluctuating wind time histories to the frequency resolution required for structures in this frequency range (Banik et al. 2010).

Examples of simulated fluctuating wind speed at 10 m reference height, as well as at the tip of the tower (46.9 m) are shown in Figure 3.4a. The variation between different 1-minute time histories at a height of 10 m is shown in Figure 3.4b. The spectrum of the fluctuating wind is shown plotted against the target spectrum (Kaimal et al. 1972) at a height of 10 m in Figure 3.5, which indicates a satisfactory match. Time histories are generated at 45 locations along the height of the tower, which correspond to the heights of the nodes in the numerical model, and are scaled for time interval (Δt) according to the relationship $\Delta t = 0.05 \times (V_{ref} / 27.8)$ m/s, where V_{ref} is an arbitrary reference mean wind speed at 10 m height.

The prototype tower was divided into 11 representative sections, referred to as loading panels, along its height as shown in Figure 3.2b. In accordance with CSA-2010, the wind loads on a single panel are calculated by

$$A_t = 0.5\tau\mu V_R^2 G_t \,(1 + 0.2\sin^2(2\theta))\,(S_{t1}C_{xt1}\cos^2\theta + S_{t2}C_{xt2}\sin^2\theta) \tag{3.6}$$

where A_t (N) is the total wind loading on the panel in the direction of the wind; τ is an air density correction factor taken to be 1; μ is the density of air taken to be 1.225 kg/m^3; V_R (m/s) is the reference wind speed based on a 10-minute averaging period at 10 m height in open country terrain; θ is the angle of attack (yaw angle) illustrated in Figure 3.2a; S_{ti} (m^2) is the total surface area projected normally on the corresponding *i*-th face, $i = 1$ and

2 (see Figure 3.2); C_{xti} is the drag coefficient for the corresponding *i*-th face; and G_t is a combined wind factor accounting for roughness of terrain and height of the panel. In this case, faces 1 and 2 correspond to the transverse and longitudinal faces of the tower, respectively.

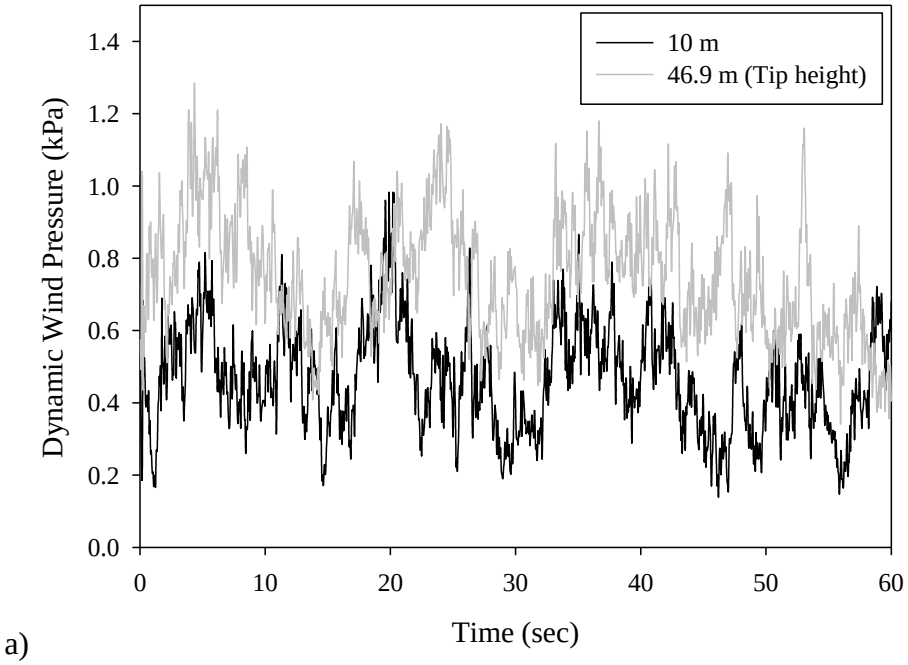

a)

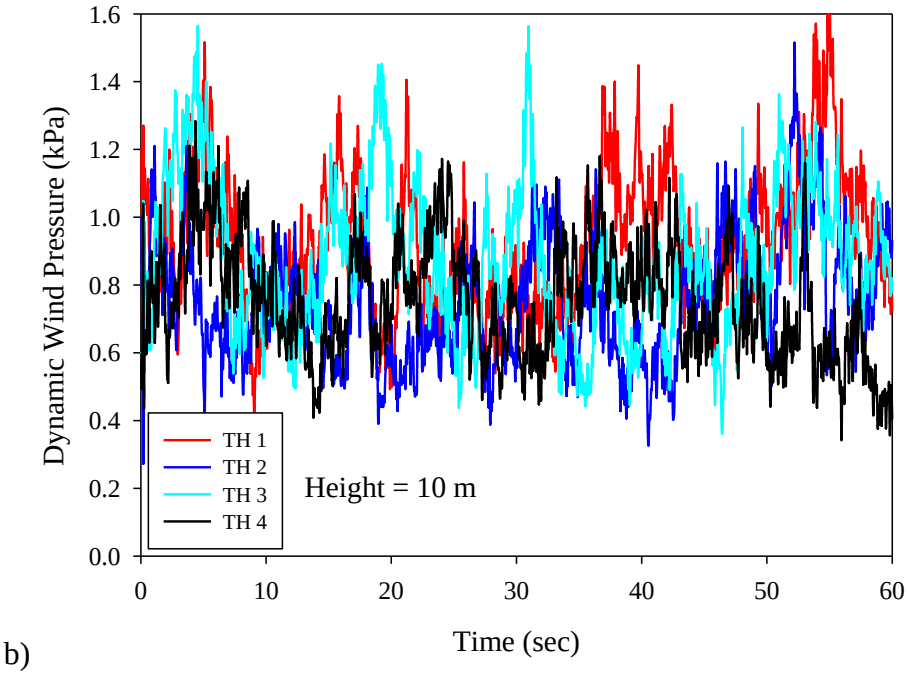

b)

Figure 3.4. Simulated time histories for a) wind at 10 m and 46.9 m (tip of tower) heights for the same time history and b) four 1-minute samples at 10 m height.

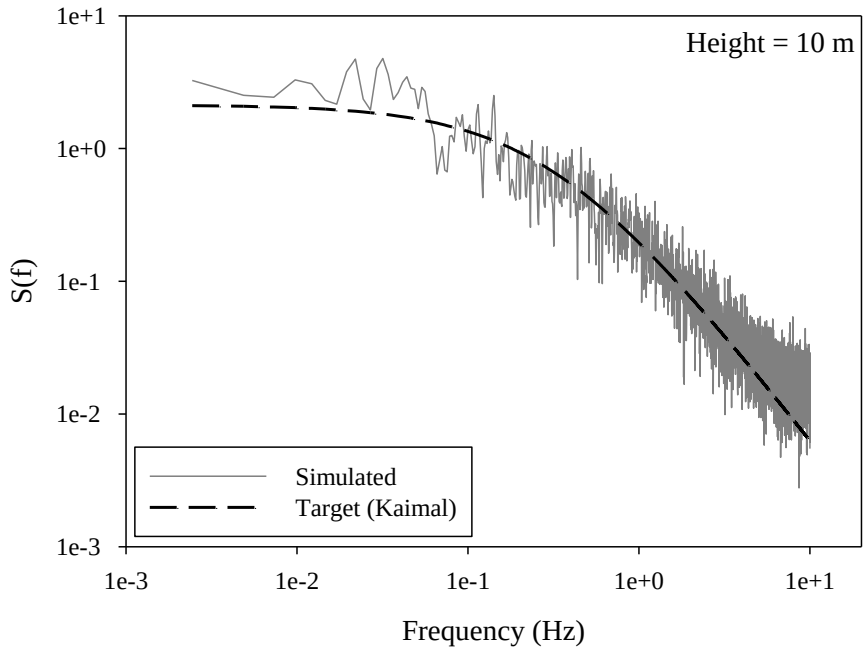

Figure 3.5. Spectrum of fluctuating wind speed at 10 m height.

The wind loads on the conductors and ground wire are calculated by

$$A_c = 0.5\tau\mu V_R^2 G_c G_L d L C_{xc} \sin^2\Omega \tag{3.7}$$

where A_c (N) is the total load on the line; C_{xc} is the drag coefficient of the line taken to be 1.0; G_c is the combined wind factor for the line (which accounts for exposure and gust response); G_L is the span factor based on the length of the span; d (m) is the diameter of the line; L (m) is the wind span of the wires; and Ω is the angle of attack (yaw angle) between the wind direction and the wires. If there is no line angle between consecutive towers, Ω equals (90-θ). The values of each parameter for each of the panels and wires are listed in Table 3.2, along with the calculation of the wind load on each panel, wire, and overall structure.

For the application of wind loads using IDA, the wind load is calculated using Eq. (3.6) and (3.7) with the terms $V_R^2 G_t$ (for the tower structure) and $V_R^2 G_c$ (for the wires) replaced with the simulated dynamic wind load at each corresponding height. For the NSP analysis, the wind load on each component of the tower is calculated based on the wind

speed at the height of the corresponding node and the parameters listed in Table 3.2 using Eq. (3.6) and (3.7). For the application of wind loads to the model, the height dependent values of G_t and G_c used in Eq. (3.6) and (3.7) are set equal to unity as the variation of wind speed with height is accounted for in the simulated wind speeds (IDA) and mean wind profile (NSP). For the tower structure, the wind load on the entire loading panel is calculated and distributed evenly among the nodes comprising each panel. That is, while aerodynamic properties are only considered for 11 unique loading panels, the wind speed is calculated at 45 heights (corresponding to the node heights in the numerical model) along the tower to account for intra-panel variation in wind speed. The wind loads on the conductors and ground wire are based on half the wind span of the wires on each side of the tower, resulting in a total loading span of 488 m (2 x 244 m) for each wire. These loads are transferred to the tower as point loads at the nodes representing the wire-structure connections.

Table 3.2. Tabulation of values for use of CSA-2010 for the transmission tower.

		Transverse (Face 1)		Longitudinal (Face 2)		
Panel	Height (m)	S_{xt1} (m^2)	C_{xt1}	S_{xt2} (m^2)	C_{xt2}	G_t
1	2.8	4.51	3.39	4.51	3.39	1.76
2	8.5	3.88	3.42	3.88	3.42	1.90
3	14.3	3.74	3.36	3.74	3.36	2.03
4	20.1	3.46	3.29	3.46	3.29	2.15
5	25.3	2.75	3.16	2.75	3.16	2.25
6	29.6	2.27	3.05	2.27	3.05	2.32
7	33.1	1.76	2.85	1.76	2.85	2.37
8	35.65	1.1	2.8	1.1	2.8	2.40
9	38.45	1.52	2.91	1.7	2.8	2.44
10	41.45	0.89	3.08	4.73	2.89	2.47
11	44.9	1.17	2.71	1.17	2.71	2.51
	Height (m)	C_{xc}	G_c	G_L	d (m)	L (m)
Conductor	35.65	1.0	2.31	0.919	0.076	488
Ground wire	44.9	1.0	2.40	0.919	0.0184	488

Note: There are 2 conductors, and 1 ground wire in the assembly.

3.3 Comparison IDA and NSP capacity curves

The NSP analysis was carried out for three wind directions: the transverse direction (0°); the longitudinal direction (90°); and for wind at 45° to the tower. The resulting capacity curves and the trajectories of the tip displacement in plan view are shown in Figures 3.6a and 3.6b, respectively. It is shown that the yield capacity is the lowest for wind at 45° to the tower, and that the stiffness of the tower is greater for the longitudinal direction. As well, the amount of deformation that the tower undergoes in the post-yield range is greater for wind directions where the wires are loaded (i.e., 0° and 45°), although the maximum capacity is lower. The ratio of tip displacement at yield to tower height shown in Figure 3.6a is in a similar range as those reported by Lee and McClure (2007) and Banik et al. (2010) for NSP analysis of steel lattice towers. In Figure 3.6b it is shown that the trajectory of the tip displacement is parallel to the direction of applied wind load for the transverse and longitudinal directions. However, for the case where wind at 45° is applied to the tower, the direction of the resultant tip displacement changes after yield occurs. For this particular case, the direction of the resultant displacement in the elastic range is closer to the transverse direction, while in the post-yield range it converges towards the direction of the applied wind load. This similarity in the elastic range between the transverse direction and wind at 45° is also observed in the capacity curves.

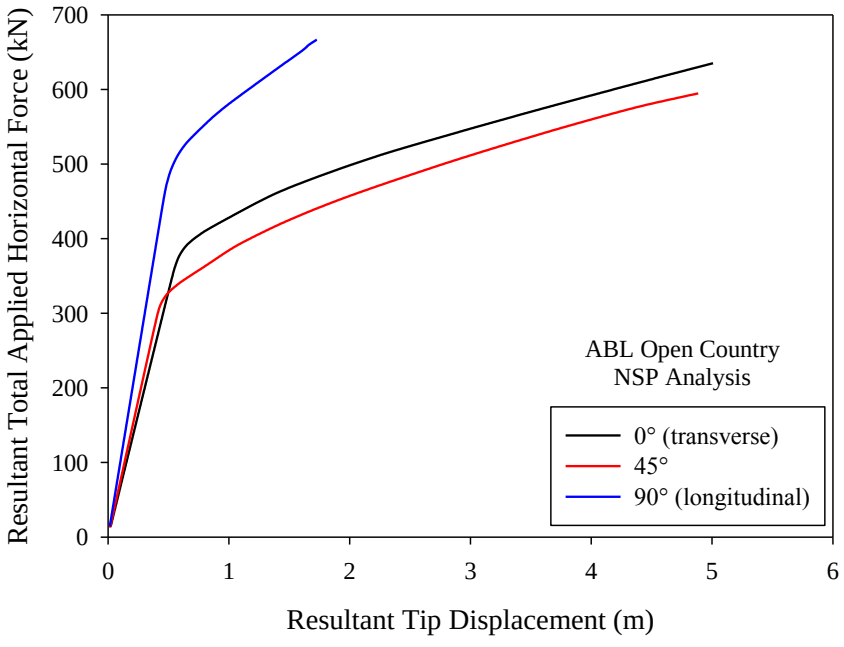

a)

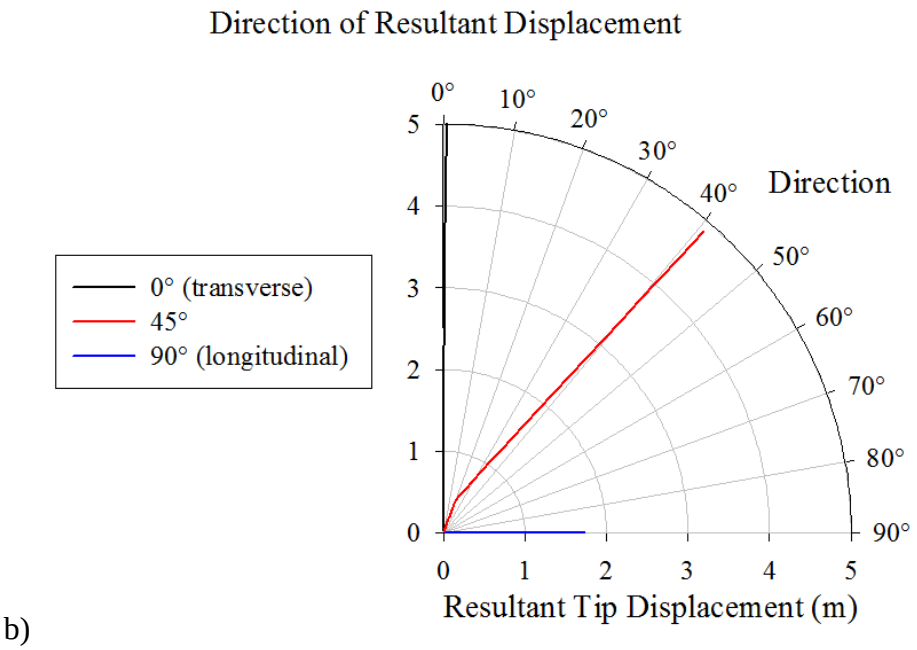

b)

Figure 3.6. Results of the NSP analysis showing a) capacity curves for each wind direction and b) trajectory of tip displacement for each wind direction.

Using the procedure described in the previous section to obtain a sampled wind speed time history (i.e., $\kappa(z,t)$), the IDA is carried out for the transverse direction and time histories of the tip displacement and base shear force are extracted from the analysis results. The time histories are used to develop the relation between the total base shear force versus the tip displacement based on: a) the maximum base shear force and corresponding tip displacement; b) the maximum tip displacement and corresponding base shear force, and; c) the maximum base shear force and the maximum tip displacement. These capacity curves, referred to as Option-a, Option-b, and Option-c, are shown in Figures 3.7a, 3.7b, and 3.7c, respectively. In all cases absolute values of the total base shear force and the tip displacement are used for plotting. The plots indicate that very similar capacity curves are developed by Option-a and Option-c, and that the NSP approximates the elastic and yield behavior quite well for this wind direction. However, after yield occurs, the use of Option-a or Option-c for the IDA capacity curve tends to reflect higher capacities than those obtained for the NSP analysis. For a specified tip displacement, Option-b, which is dictated by the maximum tip displacement, tends to correspond to a lower structural capacity as compared to the other two options.

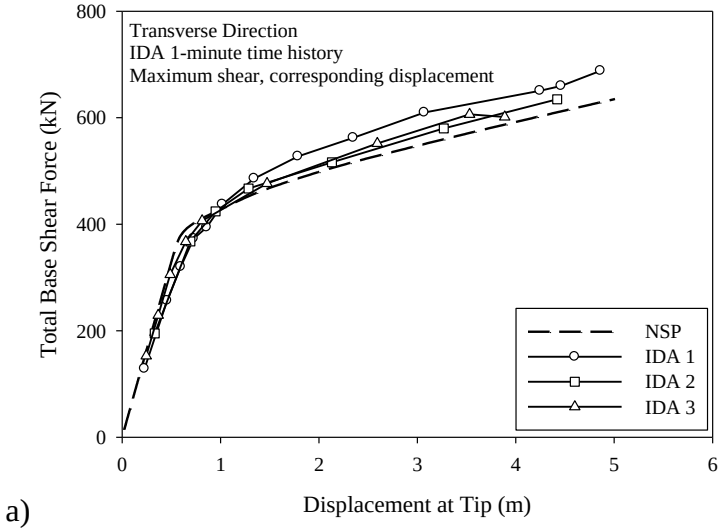

a)

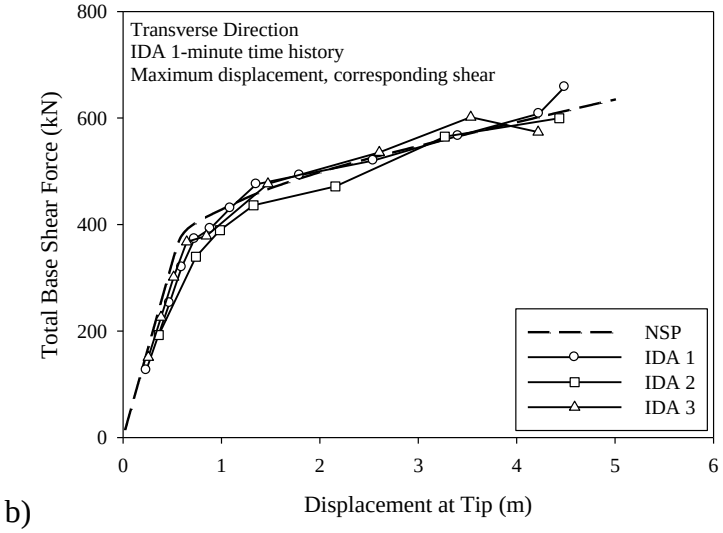

b)

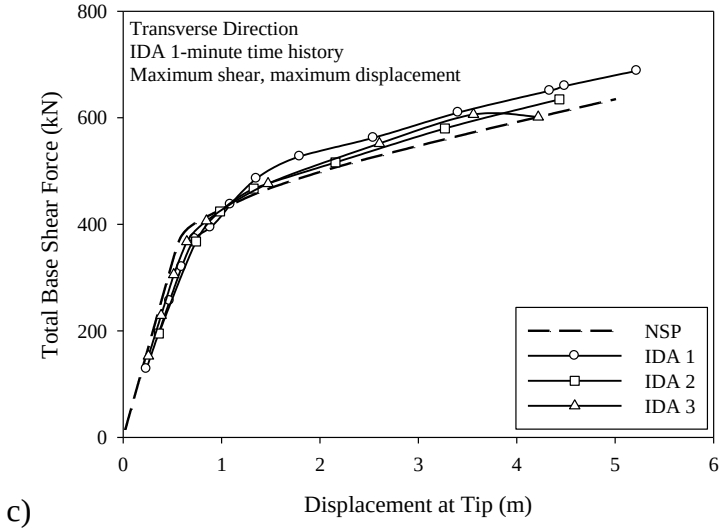

c)

Figure 3.7. Comparison of IDA and NSP capacity curves for transverse direction.

This is expected, and can be attributed to the relatively large deflections occurring in the transverse direction due to the load concentration (wind on the wires) in the upper portion of the tower.

The above analysis is repeated for two additional sets of sampled wind speed time histories. The capacity curves obtained for this analysis are also shown in Figure 3.7. The results indicate that the capacity curves are much smoother and consistent than those usually observed from IDA analyses for seismic excitations (e.g., Hong et al. 2010). This conclusion, which is consistent with that made by Banik et al. (2010), indicates that the variability of the capacity curve is not very sensitive to the simulated stationary wind speed. The curves shown in Figure 3.7 are much smoother than those given by Banik et al. (2010), which practically represent a bilinear relationship. This difference can be explained by noting that two different structural analysis software products were used between the studies.

The analysis carried out for the transverse direction is repeated for the longitudinal direction and for wind at 45° to the tower (i.e., θ = 45° in Figure 3.2a). The obtained capacity curves are shown in Figures 3.8 and 3.9 for the longitudinal direction and wind at 45° to the tower, respectively. In general, the observations drawn for the analysis results obtained for the transverse direction are also applicable for the other two directions. However, more variability in the capacity curves resulting from different time histories is shown for the longitudinal direction, as well as a greater difference in the elastic range between the IDA and NSP capacity curves. This difference is attributed to the wind load distribution occurring at the times corresponding to the greatest overall loading being dominated by gust structures near the top of the tower, which results in similar load effects as for the transverse direction. The capacity curves for wind at 45° to the tower again show the best agreement for Option-a and Option-c, and result in very similar estimates of the yield and maximum capacities between the IDA and NSP method. Note that for wind at 45° to the tower, the projections of the displacements on the horizontal plan do not remain in a straight line due to torsional responses. However, they closely follow those obtained based on the NSP method. Similar differences

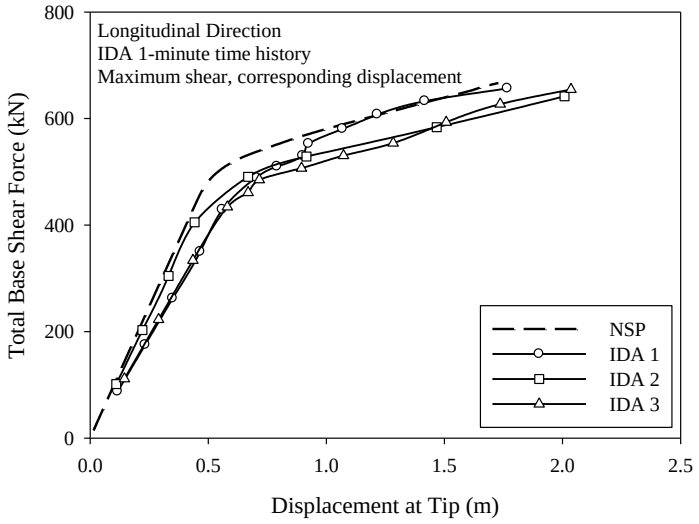

a)

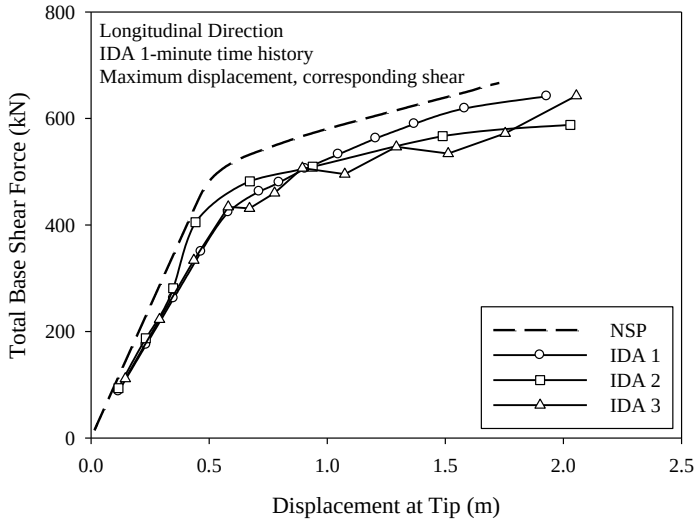

b)

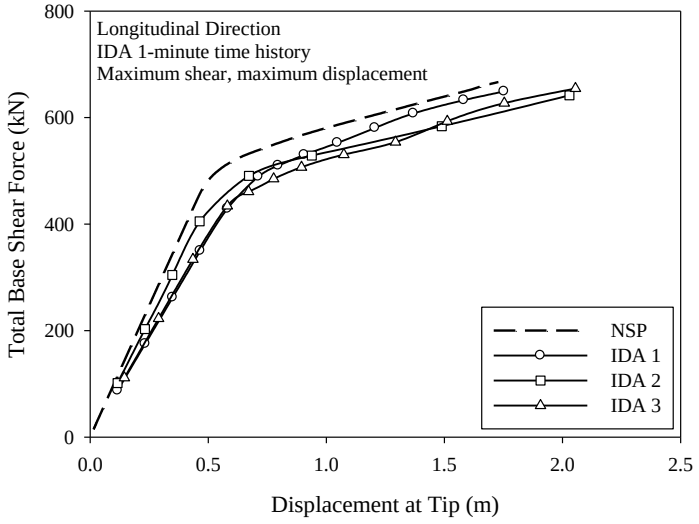

c)

Figure 3.8. Comparison of IDA and NSP capacity curves for longitudinal direction.

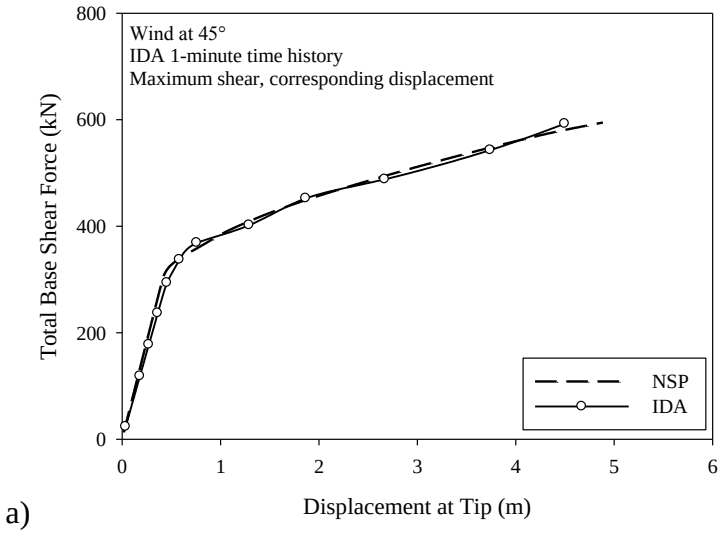

a)

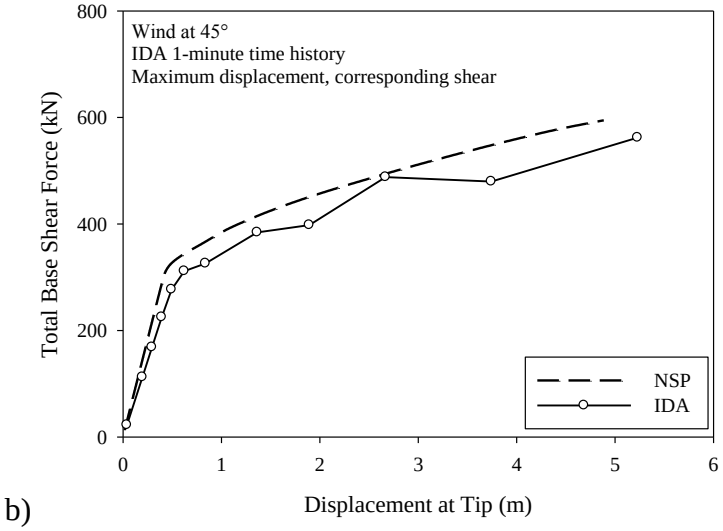

b)

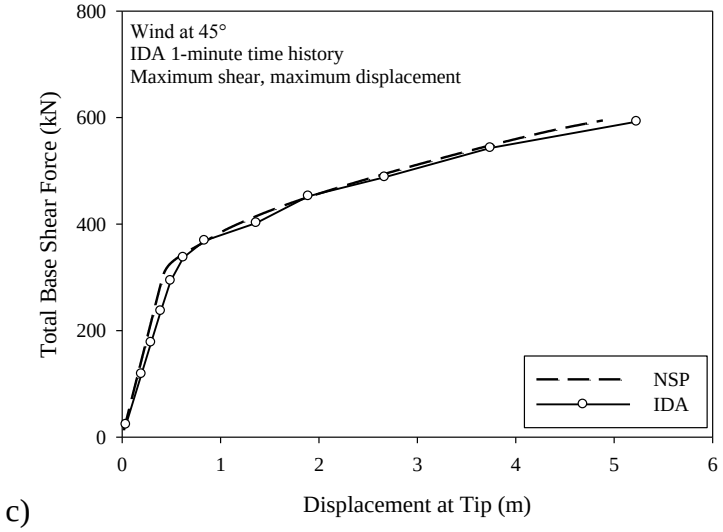

c)

Figure 3.9. Comparison of IDA and NSP capacity curves for wind at 45°.

between the elastic range of IDA and NSP capacity curves for a 2-D transmission tower (loaded in the longitudinal direction only) were found by Banik et al. (2010).

The difference in the estimated yield displacement between the IDA and NSP capacity curves is worthy of further discussion. It is shown that the estimation of yield capacity and displacement is very similar for the IDA and NSP methods for wind directions where the wires are loaded, while the use of the IDA capacity curves for the longitudinal direction results in a lower value. For wind directions where the wires are loaded, the load effects on the tower will consistently reflect high wind loads in the upper portion of the tower. Thus, the overall loads on the tower are less sensitive to spatial fluctuations in wind along the height of the tower. For the longitudinal direction, the wires are not loaded and it is shown that more variation exists among the capacity curves based on different time histories. That is, for this wind direction, the load effects are sensitive to the wind load distribution over the height of the tower. This is supported by the good agreement between IDA and NSP capacity curves for wind at 45°, where there is still a significant loading contribution from the wind on the wires. The variability of capacity curves resulting from different time histories of dynamic wind is illustrated in Figure 3.10, which compares 9 IDA capacity curves and the NSP capacity curve.

Based on the examination of each capacity curve and choice of ordinates, it is suggested that either Option-a or Option-c is preferred to define the capacity curve and to estimate the yield and maximum capacities. The fact that the differences between the capacities obtained by the IDA and NSP method, and that the capacity curves are insensitive to along height fluctuating wind speed, indicates that the use of NSP to define the capacity curve of the tower under wind load is adequate. This recommendation is considered in the subsequent chapters of this thesis.

The IDA capacity curves shown in Figures 3.7 through 3.10 are obtained through the application of a simulated 1-minute time history to the tower model. To investigate whether the capacity curves are representative of those corresponding to longer durations of wind loading, a similar analysis as described earlier was carried out for a 5-minute time history. A 5-minute time history of fluctuating wind was simulated using the

methodology described earlier. A corresponding 1-minute time history was obtained by using only the first minute of the 5-minute simulation; that is, the 1-minute sample is present in the 5-minute sample. Both time histories were then applied to the numerical model in ANSYS®, and the dynamic responses corresponding to each wind loading duration were obtained. The resulting capacity curves are shown in Figure 3.11, which show very little difference between the capacity curves obtained for 1-minute and 5-minute wind loading. The capacity curves plotted in Figure 3.11 are based on the maximum base shear and corresponding tip displacement observed during the application of the wind load.

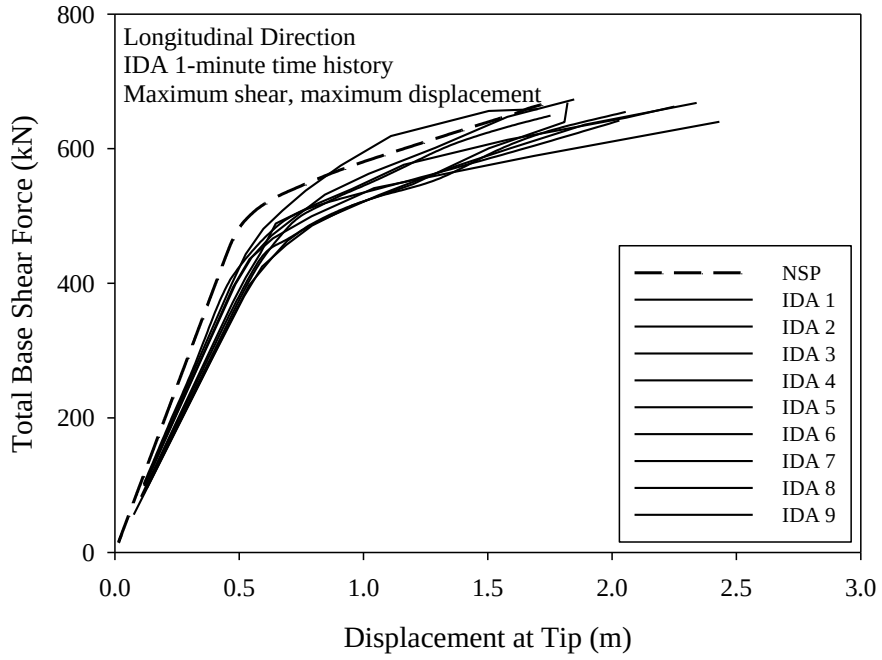

Figure 3.10. Capacity curves for 9 IDA and the NSP method for the longitudinal direction.

It should be noted that there are at least three limitations to the presented results which should be explored in the future. The first is that the fluctuating time history considered vertical coherence only; that is, the wind loads along the length of the wires are considered to be fully correlated in time. This assumption may result in a conservative estimate of the capacity of the tower, as the actual loading of the tower would benefit from the lack of correlation in the spanwise direction. The influence of torsion induced by asymmetric conductor loading on the capacity curve remains to be investigated. The

second is that strength and stiffness degradation of the structural elements is not considered in the comparison between the 1-minute and 5-minute time histories. While these effects may be negligible over the time intervals presented here, they may be of importance if strong winds of longer duration (i.e., sustained winds during hurricane passage) are of interest. Also, cyclic degradation of components or weakening due to fatigue should be considered.

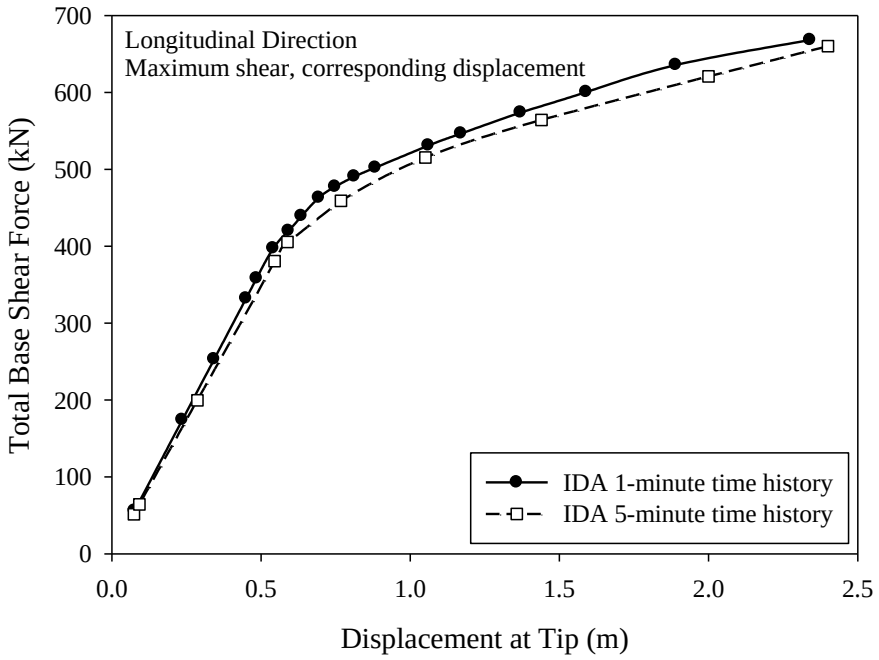

Figure 3.11. Comparison of IDA capacity curves based on 1-minute and 5-minute time histories.

3.4 Conclusions

Two popular nonlinear inelastic structural analysis for seismic loading, the IDA and NSP methods, are applied to wind loading on a 3-D model of a self-supported lattice transmission tower. The force-deformation relationship, or capacity curve, of the tower is obtained based on the IDA and NSP methods for three wind directions: the transverse and longitudinal directions, as well as for wind at 45° to the tower. It is concluded that the capacity curves from the NSP method can be used to approximate those developed by the more robust IDA, and capacity curves obtained using IDA are not significantly affected by the duration of fluctuating wind. More specifically:

1. For each wind direction considered, the capacity curves obtained by the NSP method are similar to those from the IDA, especially if those for the IDA are defined based on the maximum total reacting base shear force and the corresponding tip deflection. The agreement of curves was better for directions where the wind load on the wires is significant (i.e., transverse direction, wind at 45° to the tower).

2. No appreciable difference was observed for IDA capacity curves resulting from using wind histories of different durations (i.e., 1-minute, 5-minute). This suggests that the capacity curves based on a 1-minute fluctuating time history provide an appropriate description of the force-deformation relation of the structure.

3. If approximate results for the capacity curve of the tower are sought, it is therefore reasonable to use the capacity curve obtained using the NSP analysis. This greatly reduces the computing effort for analysis, which is important if uncertainty propagation analysis is of interest.

3.5 References

ANSYS® (2007). ANSYS Multiphysics, Release 9.0. ANSYS Inc., Canonsburg, PA.

Banik, S.S., Hong, H.P. and Kopp, G.A. (2010). "Assessment of capacity curves for transmission line towers under wind loading." *Wind Struct.*, 13(1), 1-20.

Chay, M.T., Albermani, F. and Wilson, R. (2006). "Numerical and analytical simulation of downburst wind loads." *Eng. Struct.*, 28(2), 240-254.

Canadian Standards Association (CSA) (2010). Design criteria of overhead transmission lines. CAN/CSA-C22.3 No. 60826-10, CSA, Toronto, Canada.

Davenport, A.G. (1964). "The relationship of wind structure to wind loading." *Proc. of the Symp. on Wind Effects on Buildings and Structures*, National Physical Laboratory, Teddington, UK.

Davenport, A.G. (1967). "The dependence of wind loads on meteorological parameters." *Proc. of the Int. Research Seminar on Wind Effects on Buildings and Structures*, University of Toronto Press, Toronto.

Fajfar, P. and Fischinger, M. (1988). “N2 – a method for non-linear seismic analysis of regular structures.” *Proc. 9th World Conf. Earthq. Engng*., Vol. 5, 111-116.

He, W.X. and Hong, H.P. (2012). “Probabilistic characterization of roof panel uplift capacity under wind loading.” *Can. J. Civ. Eng*., 39(12), 1285-1296.

Hong, H.P., Hong, P. and Wang, W. (2010). “Reliability of steel frames designed in accordance with the National Building Code of Canada seismic provisions and its implication in codified design.” *Eng. Struct*., 32, 1284-1291.

International Electrotechnical Commission (IEC) (2003). Design criteria of overhead transmission lines. IEC Standard 60826:2003, 3rd edition.

Kaimal, J.C., Wyngaard, J.C., Izumi, Y. and Coté, O.R. (1972). “Spectral characteristics of surface-layer turbulence.” *Quart. J. R. Met. Soc.*, 98, 563-589.

Krawinkler, H. and Seneviratna, G.D.P.K. (1998). “Pros and cons of a pushover analysis of seismic performance evaluation.” *Eng. Struct.*, 20(4-6), 452-464.

Lawson, R.S., Vance, V. and Krawinkler, H. (1994). “Nonlinear static pushover analysis – why, when and how?”. *Proc. 5th US Conf. Earthq. Engng*, Vol. 1, 183-292.

Lee, K.H. and Rosowsky, D.V. (2006). “Fragility curves for woodframe structures subjected to lateral wind load.” *Wind Struct*., 9(3), 217-230.

Lee, P.-S. and McClure, G. (2007). “Elastoplastic large deformation analysis of a lattice steel tower structure and comparison with full-scale tests.” *J. Constr. Steel Res*., 63(5), 709-717.

Samaras, E., Shinozuka, M. and Tsurui, A. (1985). “ARMA representation of random processes.” *J. Eng. Mech.*, 111(3), 449-461.

Vamvatsikos, D. and Cornell, C.A. (2002). “Incremental dynamic analysis.” *Earthquake Engng Struct. Dyn.*, 31, 491-514.

Chapter 4

4 Capacity of a transmission tower under ABL and downburst wind loading

The wind velocity profile over the height of a structure in high intensity wind (HIW) events such as downbursts differs from that associated with atmospheric boundary layer (ABL) winds. Current design codes for lattice transmission towers contain only limited advice on the treatment of HIW effects, and structural design is carried out using wind load profiles and response factors derived for ABL winds based on elastic response. This chapter assesses the load-deformation relation (capacity curve) of a transmission tower under downburst wind loading, and compares it with that obtained for an ABL wind loading profile. The analysis considers nonlinear inelastic response under simulated downburst wind fields. The capacity curve is represented by the relationship between the total applied horizontal wind load (base shear) and the maximum tip displacement. The results indicate that the capacity curve remains relatively consistent between different downburst scenarios and an ABL loading profile. The use of the capacity curve avoids difficulty associated with defining a reference wind speed and corresponding wind profile that are adequate and applicable for downburst and ABL winds, thereby allowing a direct comparison of the capacity under synoptic and downburst events. Uncertainty propagation analysis is carried out to evaluate the tower capacity by considering the uncertainty in material properties and geometric variables. The results indicate the coefficient of variation of the tower capacity is small compared to those associated with extreme wind speeds.

4.1 Introduction

Transmission structures play a vital role in society as components of electrical transmission networks and distribution systems. Electrical transmission networks span great distances while transporting electricity to the end user. Transmission structures may experience strong synoptic wind events (e.g., winter storms) or localized high intensity wind (HIW) events such as thunderstorm gust fronts, downbursts or tornadoes. Wind loads on structures resulting from synoptic events are considered to be

characterized by a traditional atmospheric boundary layer (ABL) wind speed profile, while the wind speed profile in HIWs varies among events. Though different in both meteorological and loading characteristics, each type of wind has been documented as the cause of failure in certain cases. A notable example was the failure of 19 towers in the southern portion of the Manitoba Hydro power transmission corridor due to multiple downburst events (McCarthy and Melsness 1996). The social and economic fallout of this event served as the impetus to better understand the characteristics of HIWs (Hangan et al. 2008, Banik et al. 2008), their loading on transmission structures (Mara et al. 2010, Lin et al. 2012), and the response of transmission towers to HIWs (Shehata et al. 2005, Shehata and El Damatty 2008, Banik et al. 2010).

The term ‘downburst’ was coined by Fujita (1976) to describe a strong convective downdraft which impinges on the surface of the earth, resulting in an outburst of strong winds close to ground level. Downbursts are further classified into macrobursts (outburst winds extending to distances greater than 4 km) and microbursts (outburst winds limited to distances of 4 km or less). Time histories of wind speed and direction of a microburst were recorded at Andrews Air Force Base (AAFB) on 1 August 1983; the record shows a peak wind speed of approximately 67 m/s (130+ kts) on the front side of the outflow at a height of 4.9 (Fujita 1985). This was the most intense microburst observed during the NIMROD and JAWS projects (described in Fujita (1985)), although it is expected that the probability of occurrence of microbursts of this magnitude is low. Two HIW events bearing resemblance to a downburst, a derecho and rear flank downdraft (RFD), were observed during the Texas Tech Thunderstorm Outflow Experiment (TTTOE) (Orwig and Schroeder 2007). The records include mean velocity profiles, turbulence intensity profiles, and information regarding the integral length scales and spatial correlation of the outflows. Spectral and correlation characteristics of the RFD were discussed by Holmes et al. (2008) with regards to the span reduction factor for transmission line design.

While the field studies by Fujita shed light on downburst occurrence and damage capability, and the measurements of the TTTOE provided valuable wind profile characteristics, instances of full-scale downburst observation and measurement remain quite rare. As a result, the majority of work in the structural engineering community has

progressed adopting a numerical approach to downburst wind fields, while using the few full-scale examples as references for model validation. Holmes and Oliver (2000) developed an empirical model of a downburst based on an impinging jet to be used for the simulation of damage footprints. The impinging jet approach was also used by Wood et al. (2001) to investigate the downburst wind speed profiles over various topography; they found the maximum horizontal velocity to occur at a distance of approximately 1.5 jet diameters from the center of impingement. Savory et al. (2001) modelled the time history of a translating microburst using an impinging jet combined with a previously developed wind velocity profile in order to apply transient loading to a transmission tower. It was found that the displacement of the tip of the tower was proportional to the applied wind loading throughout the duration of the microburst passage, which implies the response is quasi-static. A transient downburst wind field was modelled using a stationary axisymmetric impinging jet by Hangan et al. (2003), which provided a spatio-temporal flow model that could be applied to structures. Kim and Hangan (2007) compared the time series of the wind speed in the simulated outflow to the full-scale measurements obtained in the TTTOE, showing good agreement. The downburst wind fields generated in the Hangan et al. (2003) simulation are applied to a structural model in the present study. This downburst wind field model was selected due to its capability to model the primary and secondary vortex rings, which is necessary to adequately characterize the shape of the downburst wind speed time history. It is important to note unlike the case of ABL wind, where it is considered to have a fixed wind speed profile with height, the wind speed profile in a downburst outflow is transient. Specifically, the profile is a function of many parameters, including the size and strength of the downburst, and the distance between the downburst center (point of touchdown) to the point of interest. This makes a meaningful definition of a reference wind speed, or maximum wind speed, resulting from a particular downburst challenging. This has implications for the development and application of design codes. Therefore, a solution to this problem through simplification of design verification for structures is worth exploring.

Few studies directed at the assessment of structural response to downburst winds are available in the literature. An analysis of a transmission tower-line system having guyed

towers under simulated downburst wind was carried out by Shehata et al. (2005). In the analysis, the forces on the conductors and ground wires were calculated using geometric nonlinear analysis, and were applied in combination with quasi-static wind loads on the tower. The use of quasi-static wind forces on the tower was justified based on a frequency comparison showing that the fundamental frequency of vibration of the tower is much lower than the predominant frequency content of the downburst, thereby making the resonant component negligible. This is consistent with the approach taken in the development of gust factors for transmission lines (e.g., Davenport 1979). The use of quasi-static analysis for the tower was also applied by Darwish et al. (2011). An attempt to identify the failure mechanisms of a tower during a microburst event is presented by Shehata and El Damatty (2008). For the identification, a linear elastic analysis is carried out; members are removed from the structural model if their capacity is exceeded, and failure is assumed to occur at numerical divergence. It is notable that these studies considered the geometric nonlinearity of the conductor and ground wire response, and that linear quasi-static analysis of the overall structure was carried out.

Based on the application of the nonlinear incremental dynamic and nonlinear static pushover (NSP) methods to wind loads on a 2-D numerical model of a self-supported transmission tower, Banik et al. (2010) observed that the capacity curve, defined in terms of the total horizontal force (analogous to the total reacting base shear force in inertial forces are negligible) versus the tip displacement, can be adequately assessed using the NSP method. This was verified for a 3-D model of a self-supported transmission tower in Chapter 3. Furthermore, it was found that the capacity of the tower at the incipient of yield and of collapse is influenced by the wind speed profile over the height of the tower. As the failure and reliability of a tower depend directly on its capacity curve, the evaluation of these quantities under downburst loading is relevant and important for both the design of new towers and the evaluation of existing towers.

The present study is focused on the parametric investigation of the tower capacity curve, providing the yield and maximum capacity (i.e., capacity at incipient of collapse), of a self-supported transmission tower under multiple scenarios of downburst wind loading. Evaluation of the difference between the tower capacity curve under ABL and downburst

wind is made, as well as an assessment of the effect of uncertainty in material properties. The goal of the work is to develop a simple practical solution which can be directly used to evaluate the performance of a tower under downburst wind loading. Both material and geometric nonlinearity is considered in the analysis of the 3-D transmission tower model.

4.2 Modeling of the transmission tower, ABL wind loads and effects

4.2.1 Numerical model of transmission tower

A self-supported lattice transmission tower design was provided by Manitoba Hydro and modelled in ANSYS Multiphysics 9.0 (ANSYS 2007). The tower members are modelled using 2-node nonlinear 3-D frame elements assuming rigid connections (representative of multi-bolted moment-resisting connections). The masses of the conductors and ground wire are applied as lumped masses to the structure at the corresponding nodes. A 3-D view of the numerical model is shown in Figure 4.1. The material nonlinearity of the tower members is modelled using bilinear elastoplastic material properties, and the geometric nonlinearities (e.g., buckling effects) are accounted for through the use of a large deformation analysis. The section properties of the structural members of the tower and wires, along with the nominal dimensions of the structural steel and distribution by panel, are shown in Table 4.1.

A total of 959 elements and 405 nodes are used in the modelling of the tower. A modal analysis was carried out on the numerical model, showing that the first and second modes of vibration correspond to sway in the transverse and longitudinal directions, respectively. The fundamental frequencies of vibration for the transverse and longitudinal directions are 1.167 Hz and 1.232 Hz, respectively. The third mode of vibration is torsion, having a fundamental frequency of 1.556 Hz. Plots of the first three modes of vibration are provided in Figure 4.2.

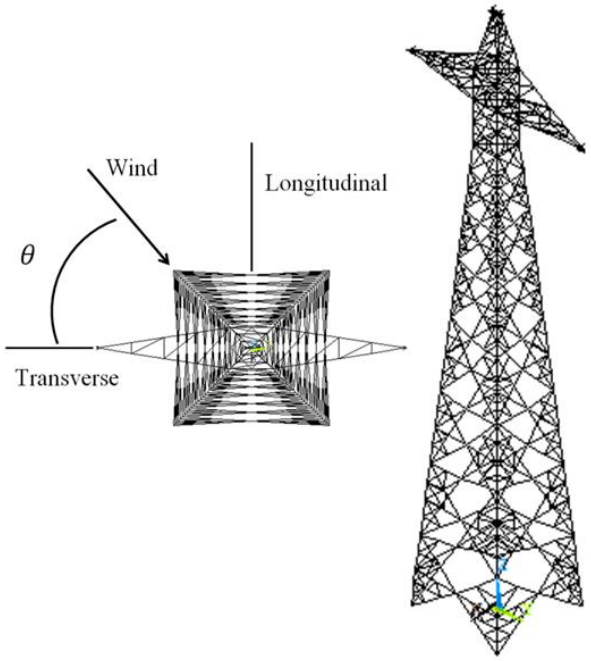

a)

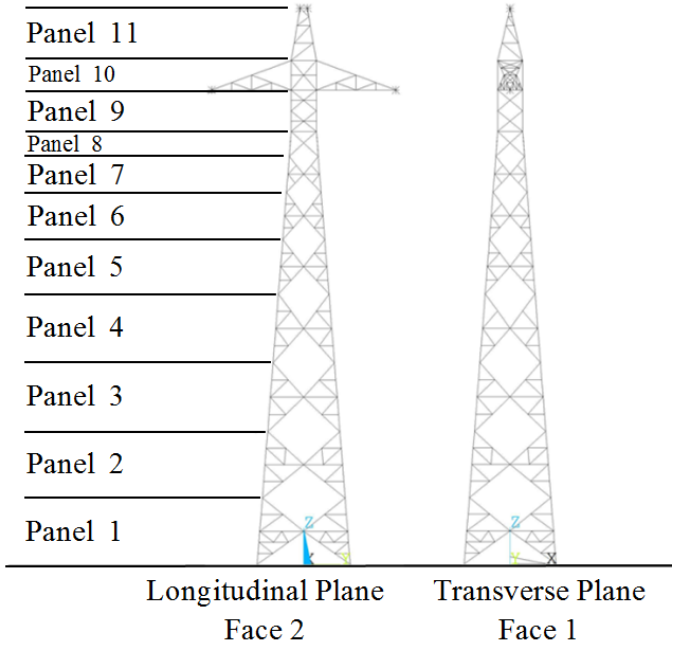

b)

Figure 4.1. Transmission tower: a) 3-dimensional view, b) definition of loading panels according to code-based design procedure.

Table 4.1.a) Nominal section properties of the structural members of the tower and wires, b) structural steel distribution by panel, c) nominal section properties of the conductors, and d) properties and uncertainty associated with structural steel.

a)

	SI Units (m)		Customary Units (in)		
	Angle	Thickness	Angle	Thickness	Member Key
Chords and Horizontals	0.0445 x .0445	0.125	(1 3/4)" x (1 3/4)"	(1/8)"	a
	0.0445 x .0445	0.375	(1 3/4)" x (1 3/4)"	(3/8)"	b
	0.0508 x 0.0508	0.125	2" x 2"	(1/8)"	c
	0.0508 x 0.0508	0.1875	2" x 2"	(3/16)"	d
	0.0635 x 0.0635	0.1875	(2 1/2)" x (2 1/2)"	(3/16)"	e
	0.0762 x 0.0762	0.1875	3" x 3"	(3/16)"	f
Diagonals and Legs	0.0762 x 0.0762	0.125	3" x 3"	(1/4)"	D1
	0.0889 x 0.0635	0.125	(3 1/2)" x (2 1/2)"	(1/4)"	D2
	0.0889 x 0.0889	0.125	(3 1/2)" x (3 1/2)"	(1/4)"	D3
	0.1016 x 0.1016	0.1875	4" x 4"	(3/16)"	D4
	0.127 x 0.127	0.3125	5" x 5"	(5/16)"	L1
	0.127 x 0.127	0.375	5" x 5"	(3/8)"	L2

b)

	Members in Resisting Direction		Support
Panel	Longitudinal	Transverse	Plan
1	L2, D2, a, c, d	L2, D1, a, c, d	
2	L2, D2, a, b, d	L2, D2, a, b, d	
3	L2, D3, c, e	L2, D2, c, e	
4	L2, D3, a, e	L2, D2, a, e	
5	L1, D3, a, d	L1, D2, a, d	
6	L1, D3, a, b	L1, D2, a, b	
7	L1, D3, a, c	L1, D3, a, c	
8	L1, D4, d	L1, D3, d	
9	D3	D3, a	a
10	D3, e	D3, D4, a, d, f	L1, D1, a, b, d, e
11	a, e	D1, a, b, c	

c)

Property	Conductor	Ground wire
Diameter (m)	0.0381	0.0184
Density (kg/m)	2.354	1.046
Modulus of Elasticity (GPa)	58.6	125.3
Design Span (m)	488	488

d)

Random Variable	Mean	COV	Distribution Type
Density	7.8 kg/m^3	0.05	Lognormal
Modulus of elasticity	2E+8 kN/m^2	0.1	Lognormal
Ratio of post-yield stiffness to initial stiffness	0.05	0.1	Lognormal
Section dimensions	Varies with section[1]	0.025	Lognormal
Yield strength	3.3E+5 kN/m^2	0.1	Lognormal

Note: The mean of section dimension is considered to be equal to nominal section dimension shown in Table 4.1a.

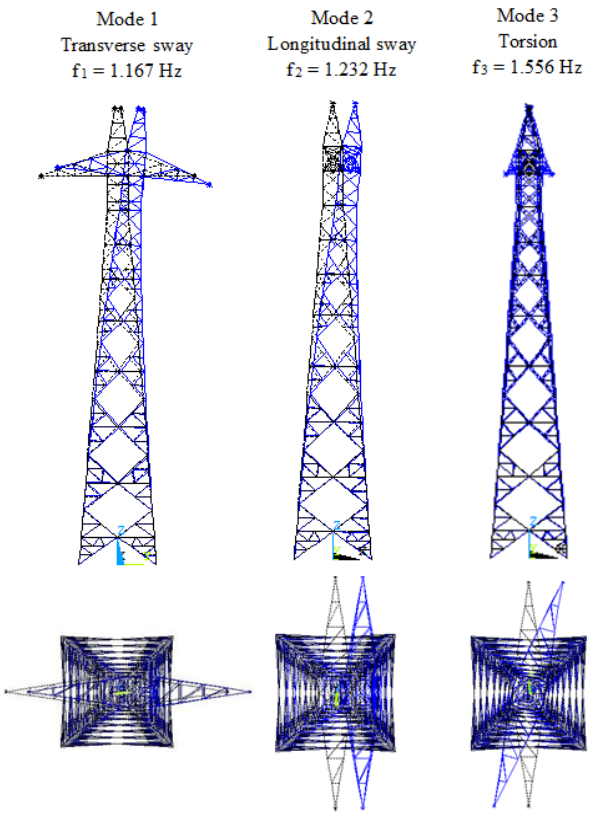

Figure 4.2. Mode shapes and frequencies of the analytical tower model.

4.2.2 Loads under synoptic wind

Wind loads on structures resulting from synoptic events are considered to be characterized by a traditional ABL (i.e., power law) wind speed profile. Design wind loads for transmission towers are specified in CAN/CSA C22.3 No. 60826-10 (referred to herein as CSA-2010) (CAN/CSA 2010), as well as ASCE Manual No. 74 (referred to herein as ASCE-74) (ASCE 2010). CSA-2010 adopts the International Electrotechnical Commission (IEC) Standard 60826:2003 for design criteria of overhead transmission lines (IEC 2003), which is used throughout the world for the design of transmission structures. As the current analysis is carried out on a structure designed and built in Canada, it is prudent to invoke the specifications in CSA-210 for later comparison. The prototype tower was divided into 11 representative sections, referred to as panels, along its height as shown in Figure 4.1. An exposure based on open country terrain was used, which corresponds to a roughness length of 0.03 m and a power law coefficient of 0.16. It should be noted that the reference wind speed in CSA-2010 is referenced to a 10-minute mean average wind speed at a height of 10 m in open country terrain; the implications of this on the results obtained through numerical analysis will be discussed later.

In accordance with CSA-2010, the wind loads on a single panel are calculated by

$$A_t = 0.5\tau\mu V_R^2 G_t \,(1 + 0.2\sin^2(2\theta))\,(S_{t1}C_{xt1}\cos^2\theta + S_{t2}C_{xt2}\sin^2\theta) \tag{4.1}$$

where A_t (N) is the total wind loading on the panel in the direction of the wind; τ is an air density correction factor taken to be 1; μ is the density of air taken to be 1.225 kg/m^3; V_R (m/s) is the reference wind speed based on a 10-minute averaging period at 10 m height in open country terrain; θ is the angle of attack (yaw angle) illustrated in Figure 4.1; S_{ti} (m^2) is the total surface area projected normally on the corresponding i-th face, i = 1 and 2 (see Figure 4.1); C_{xti} is the drag coefficient for the corresponding i-th face; and G_t is a combined wind factor accounting for roughness of terrain and height of the panel. In this case, faces 1 and 2 correspond to the transverse and longitudinal faces of the tower, respectively.

The wind loads on the conductors and ground wire are calculated by

$$A_c = 0.5\tau\mu V_R^2 G_c G_L d L C_{xc} \sin^2\Omega \quad (4.2)$$

where A_c (N) is the total load on the line; C_{xc} is the drag coefficient of the line taken to be 1.0; G_c is the combined wind factor for the line; G_L is the span factor based on the length of the span; d (m) is the diameter of the line; L (m) is the wind span of the wires; and Ω is the angle of attack (yaw angle) between the wind direction and the wires. If there is no line angle between consecutive towers, Ω equals (90-θ).

The values of each parameter for each of the panels and wires are listed in Table 4.2, along with the calculation of the wind load on each panel, wire, and overall structure. For the calculation, the height dependent values of G_t and G_c required for Eq. (4.1) and (4.2) are directly obtained from the equations supplied in CSA-2010. It is shown that the total wind load in the longitudinal and transverse directions are $128.8V_R^2$ N and $220.4V_R^2$ N, respectively. The load in the transverse direction is much greater due to the contributions of the conductors and ground wire.

4.2.3 Capacity curves for ABL and rectangular wind

The NSP method is a widely used analysis technique for evaluating the performance and capacity of structures under seismic loading (e.g., Krawinkler and Seneviratna 1998), and more recently has been applied to point loading (Lee and McClure 2007) and wind loading (e.g., Banik et al. 2010). The procedure is used to evaluate the nonlinear force-deformation relationship and identify the yield and maximum capacities of a structure by monotonically increasing the applied forces while maintaining a constant loading profile. A force deformation curve, or capacity curve, showing the behaviour of a nonlinear inelastic system is shown in Figure 4.3. In this case, the force represents the total applied horizontal wind load (which is equivalent to the resultant base shear), and the deformation represents the displacement of the tip of the tower. The curve is approximated by a bilinear system; the yield capacity of the system is defined by the point of intersection of the elastic and post-yield tangents (as shown in Figure 4.3), while the maximum capacity is defined by the incipient of collapse of the tower. Note that

Banik et al. (2010) showed that the capacity curve obtained using the NSP method provides a good approximation to that obtained from nonlinear incremental dynamic analysis, and that the curves determined in such a manner represent the effect of a peak wind load on the tower. The estimated capacities can therefore be viewed as representative of response under short-duration gust (i.e., 3-second gust mean wind speed). This consideration and procedure are also applied in the following analysis.

Table 4.2. a) Nominal wind load calculated using CSA-2010 for the tower shown in Figure 4.1 and b) nominal wind load calculated using CSA-2010 for the conductor.

a)

		Longitudinal direction				Transverse direction			
Panel	Height (m)	Area (m^2)	C_d	G_t	F_d (N)/V^2_R	Area (m^2)	C_d	G_t	F_d (N)/V^2_R
1	2.8	4.51	3.39	1.76	16.48	4.51	3.39	1.76	16.48
2	8.5	3.88	3.42	1.9	15.44	3.88	3.42	1.9	15.44
3	14.3	3.74	3.36	2.03	15.62	3.74	3.36	2.03	15.62
4	20.1	3.46	3.29	2.15	14.99	3.46	3.29	2.15	14.99
5	25.3	2.75	3.16	2.25	11.98	2.75	3.16	2.25	11.98
6	29.6	2.27	3.05	2.32	9.84	2.27	3.05	2.32	9.84
7	33.1	1.76	2.85	2.37	7.28	1.76	2.85	2.37	7.28
8	35.65	1.1	2.8	2.4	4.53	1.1	2.8	2.4	4.53
9	38.45	1.7	2.8	2.44	7.11	1.52	2.91	2.44	6.61
10	41.45	4.73	2.89	2.47	20.68	0.89	3.08	2.47	4.15
11	44.9	1.17	2.71	2.51	4.87	1.17	2.71	2.51	4.87
			Longitudinal		128.83 V^2_R		Transverse		111.79 V^2_R

b)

Cable	Height (m)	d (m)	L (m)	C_d	Number	G_L	G_w	F_d (N)/V^2_R
Conductor	35.65	0.076	488	1	2	0.919	2.31	96.44
Ground wire	44.9	0.0184	488	1	1	0.919	2.4	12.13
					Transverse (wires)			108.60 V^2_R
					Transverse including those on tower (total)			220.39 V^2_R

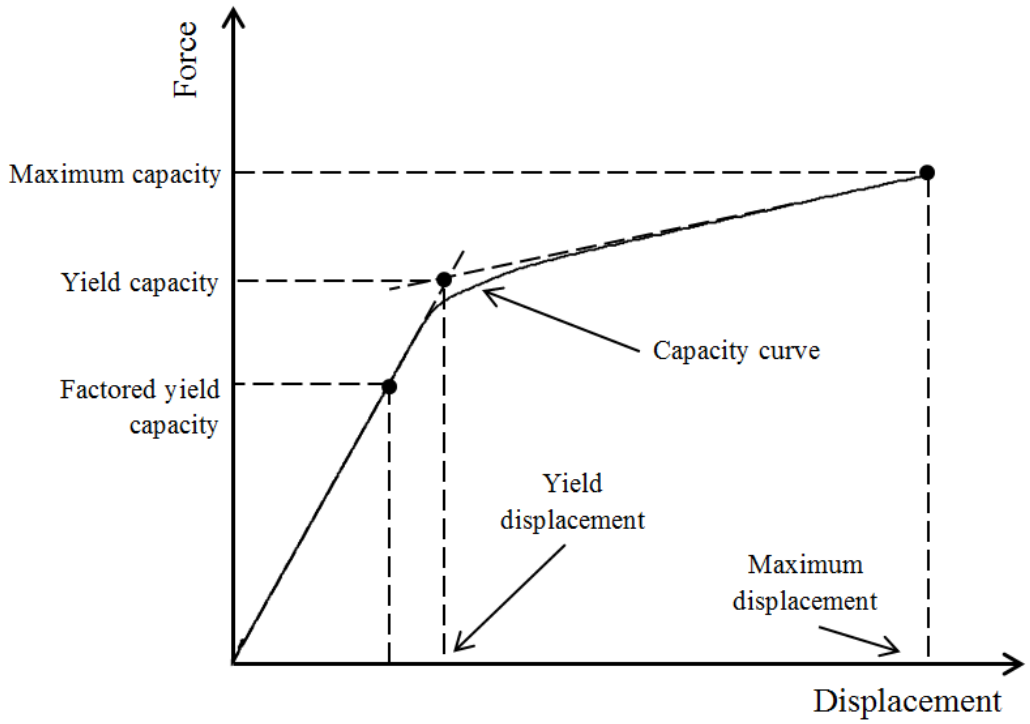

Figure 4.3. Force-deformation or capacity curve for an inelastic system.

To establish a basis for comparison of capacity curves resulting from wind profiles representative of downburst outflow winds, the capacity curves for two basic wind profiles were initially evaluated. For this, the mean values of the structural material properties and geometric variables are employed, and the effect of their uncertainty is neglected. The first wind profile represents a traditional ABL wind profile based on the power law in open country terrain (power law exponent of α). Assuming that the wind speed is fully correlated spatially, or coherent (for this or any other wind profile considered in this study), the adopted power law suggests that the 3-second gust mean wind speed at a height z (m) above the ground, $V_{3s}(z)$, is given by

$$V_{3s}(z) = (z/10)^{\alpha} V_{3s,10m} \tag{4.3}$$

where $V_{3s,10m}$ represents the 3-second gust mean wind speed at a height of 10 m. A value of α equal to (1/9.5) is suggested in ASCE-74 for a 3-second gust mean wind speed profile in open country terrain, while a value of 0.16 is specified by CSA-2010 for the 10-minute mean wind speed profile. The latter results in a greater increase in wind speed

over the height of a structure than the former. As it will be shown, the consideration of the ABL wind profile is directed at developing a lower bound for the capacity curve of the tower, and a larger value of α leads to a lower capacity curve. A power law coefficient of α = 0.16 is therefore applied in the remaining part of this study, which results in a slightly conservative estimate of the lower bound of the capacity curve if gust mean wind speed averaging times are considered.

The second profile is rectangular in shape, which represents a uniform wind profile over the height of the tower (i.e., $V_{3s}(z)$ equals $V_{3s,10m}$ over the height). This profile is selected, as it will be shown, since it resembles the downburst wind profile for the range of parameters considered in this study within the height range of interest (5 to 50 m above the ground).

The wind load at the height of each structural connection (represented as nodes in the numerical model) is calculated based on the wind profile described in Eq. (4.3) and the corresponding panel characteristics, and is distributed equally among the nodes within each panel. That is, while aerodynamic properties are only considered for 11 unique panels, the wind speed is calculated at 45 heights (corresponding to the node heights in the numerical model shown in Figure 4.1) along the height of the tower to account for intra-panel variation in wind speed. The wind loads on the conductors and ground wire are calculated according to Eq. (4.2) and are based on half the wind span of the lines on each side of the tower, resulting in a total loading span for each wire of 488 m (2 x 244 m). The values used for the tower dimensions and aerodynamic coefficients of each panel are shown in Table 4.1. The wind loads on the conductors and ground wire are transferred to the tower as point loads at the nodes representing the wire-structure connections.

Based on the above considerations, the wind load on each panel along the height of the tower in terms of $V^2_{3s,10m}$ were calculated and are shown in Table 4.3. As the variation of wind speed over height is considered using $V_{3s}(z)$, and that the wind speeds are gust wind speeds, G_t and G_c in Eq. (4.1) and (4.2) are set to unity. Note that the wind load in CSA-2010 is specified based on a 10-minute mean wind speed at 10 m height, $V_{10\text{-min},10m}$, and

those shown in Table 4.3 are estimated in terms of $V_{3s,10m}$. As well, a more detailed description of the wind loading profile was utilized in the analysis, in comparison to the piecewise approach applied when using the code. To facilitate the discussion of the tower capacity in the context of the codified design, the capacity in terms of $V_{3s,10m}$ are converted to in terms of $V_{10\text{-min},10m}$. For the conversion, the ratios $V_{3s,10m}$ /$V_{10\text{-min},10m}$ = 1.43 for open country terrain (Durst 1960) is used. The wind loads in terms $V_{10\text{-min},10m}$ are $145.8V^2_{10\text{-min},10m}$ for the longitudinal direction and $286.3V^2_{10\text{-min},10m}$ for the transverse direction. Comparison of these values to those shown in Table 4.2 indicates that the use of the procedure described previously leads to 11% greater wind load (i.e., 5.7% greater wind speed) in the longitudinal direction and 23% greater wind load (i.e., 12.3% greater wind speed) in the transverse direction. The differences are attributed to the use of the ABL profile and more detailed wind load variation over height in the above procedure, compared to the use of G_t and panel approach in the design code. In all cases, the procedure and considered ABL profile lead to more conservative estimated wind load.

Table 4.3. Yield and maximum capacities and corresponding wind speed for the tower in the longitudinal and transverse directions.

	ABL profile		Rectangular	
	Longitudinal	Transverse	Longitudinal	Transverse
Wind load (N) in terms of $V^2_{3s,10m}$ and of ($V^2_{10\text{-min},10m}$)	$71.3V^2_{3s,10m}$ ($145.8V^2_{10\text{-min},10m}$)	$140\ V^2_{3s,10m}$ ($286.3V^2_{10\text{-min},10m}$)	$58.9V^2_{3s,10m}$ ($120.4V^2_{10\text{-min},10m}$)	$102.9V^2_{3s,10m}$ ($210.9V^2_{10\text{-min},10m}$)
Yield capacity (kN)	515.3	442.5	559.4	487.7
Maximum capacity (kN)	665.6	649.8	637.8	699.9
Critical $V_{3s,10m}$ ($V_{10\text{-min},10m}$) for yield (m/s)	85 (59.4)	56.2 (39.3)	97.5 (68.2)	68.8 (48.1)
Critical $V_{3s,10m}$ ($V_{10\text{-min},10m}$) for collapse (m/s)	96.6 (67.6)	68.1 (47.6)	104.1 (72.8)	82.5 (57.7)

The NSP method is carried out for the ABL and rectangular wind profiles, and the obtained capacity curves are shown in Figures 4.4a and 4.4b for wind in the longitudinal and transverse directions, respectively. For the longitudinal or transverse loading cases, the total applied horizontal force and tip displacement are in place with the applied load. Figure 4.4a shows that the yield capacities of the tower in the longitudinal direction are

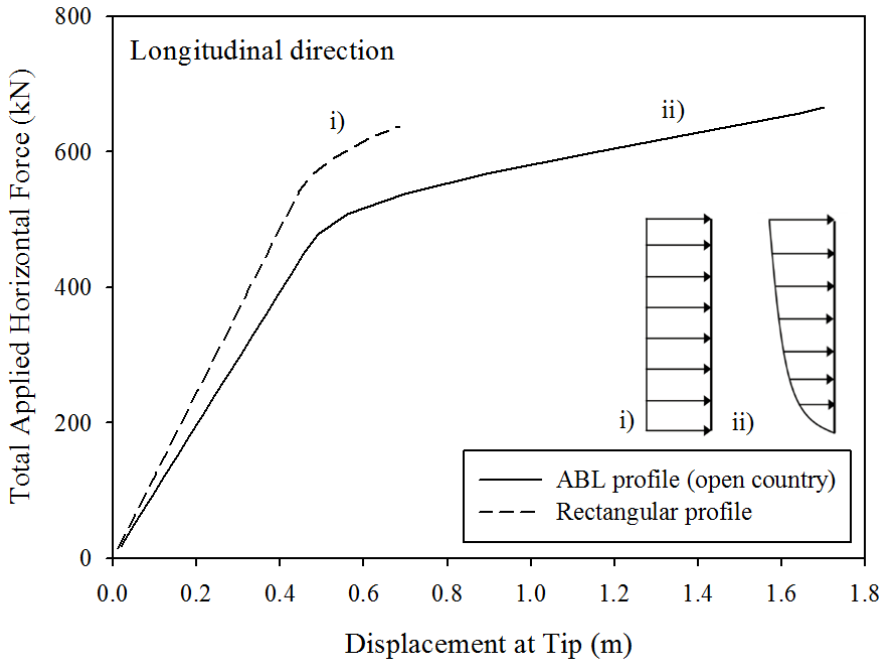

a)

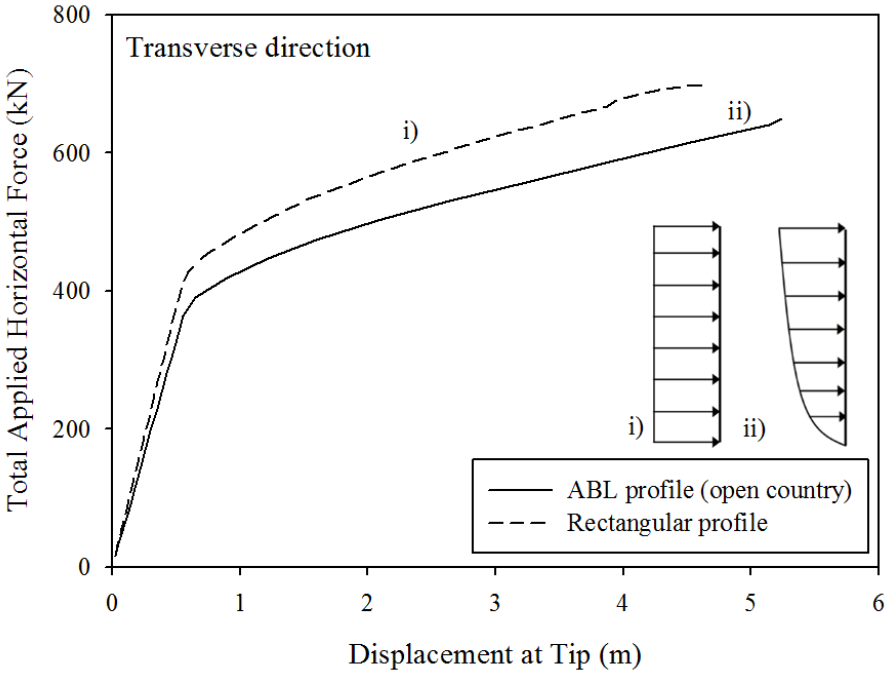

b)

Figure 4.4. Capacity curves for ABL and rectangular wind distributions in a) longitudinal direction, b) transverse direction.

approximately 515.3 kN and 559.4 kN for the ABL and rectangular wind profiles, respectively. The capacity of the tower at incipient of yield for the rectangular wind profile is greater than for the ABL wind profile. However, this trend is reversed if the incipient of collapse is of concern, and a large horizontal deformation is associated with the ABL profile. In this case, the capacities at incipient of collapse, or the maximum capacities, of the tower in the longitudinal direction are approximately 665.6 kN and 637.8 kN for the ABL and rectangular wind profiles, respectively. Using the calculated wind load shown in Table 4.3, and the estimated capacity at incipient of yield or of collapse, the corresponding $V_{3s,10m}$ values are calculated and shown in the same table. The values indicate that the tower can sustain a $V_{3s,10m}$ of 85 (m/s) without yield in the longitudinal direction if the ABL wind profile is considered, while this value becomes 97.5 (m/s) if the rectangular wind profile is considered. Similar magnitude of difference between the critical wind speed for incipient of collapse can also be observed from the table; this difference indicates the potential influence of the shape of the wind profile on estimated capacity of the tower.

Comparison of the results in Figures 4.4a and 4.4b indicates that the yield capacities of the tower in the transverse direction are significantly lower than those in the longitudinal direction, although the capacities at incipient of collapse in the transverse direction are comparable to those in the longitudinal direction. This translates to a lower maximum wind speed due to the loaded area in the transverse direction. The tower can withstand a greater (total) horizontal wind load for the rectangular wind load distribution due to the lower load contributions of the cross-arm of the tower in the longitudinal direction and the wires in the transverse direction. However, it is shown that if the ABL profile is applied, more deformation occurs in the post-yield range. This is again attributed to the load concentration in the upper portion of the tower. Similar to the case for longitudinal wind loading, the estimated capacity at incipient of yield and collapse, as well as their corresponding $V_{3s,10m}$ wind speeds, are summarized in Table 4.3. The table indicates that the critical wind speed that the tower can withstand is governed by the critical wind speed, or capacity, in the transverse direction. In all cases, the critical values in terms of $V_{10\text{-min},10m}$ are also calculated (using $V_{3s,10m}$ /$V_{10\text{-min},10m}$ = 1.43) and shown in the table to facilitate the reader.

4.2.4 Uncertainty propagation analysis

The geometric and material variables of structures are uncertain; this uncertainty influences the calibration of load and resistance factors in the codification process (Ellingwood et al. 1980, Bartlett et al. 2003). To assess the effects of these uncertainties on the tower capacity under ABL wind loading, the simple Monte Carlo technique is used to sample the values of material properties and geometric variables from their probability distribution models (shown in Table 4.1). Capacity curves of the tower for simulated sets of structural and geometric properties are developed; the properties sampled for each element were consistent within each simulated tower. The adopted probabilistic models shown in Table 4.1 are based on those provided by Manitoba Hydro, as well as those found in the literature and used for code calibration (Ellingwood et al. 1980, Bartlett et al. 2003, Haukaas and Der Kiureghian 2006). 50 samples of capacity curves based on the ABL profile are obtained and shown in Figures 4.5a and 4.5b for wind loading in the longitudinal and transverse directions, respectively. The mean and coefficient of variation (cov) of the yield and maximum tower capacities from these samples are calculated and shown in Table 4.4. In all cases, the estimated cov values are within 0.083 and 0.096. This range of cov is slightly lower than the highest cov values of 0.10 considered for material properties, while much less than the cov encountered for extreme wind load effects (i.e., Bartlett et al. 2003) of about 0.25 to 0.4.

Since the cov of the capacity curve is relatively small as compared to that of the wind load effect, its accurate estimation and its impact on reliability analysis and design code calibration are likely to be less important than those of the wind load effect. Therefore, no further analysis of the uncertainty of the capacity curve was carried out in the remaining part of this study.

Table 4.4. Statistics of tower capacity under longitudinal and transversal loading (based on 50 simulations).

	Yield capacity (kN)		Maximum capacity (kN)	
Direction	Mean	cov	Mean	cov
Longitudinal	508.3	0.094	664.5	0.083
Transverse	436.2	0.096	618.5	0.095

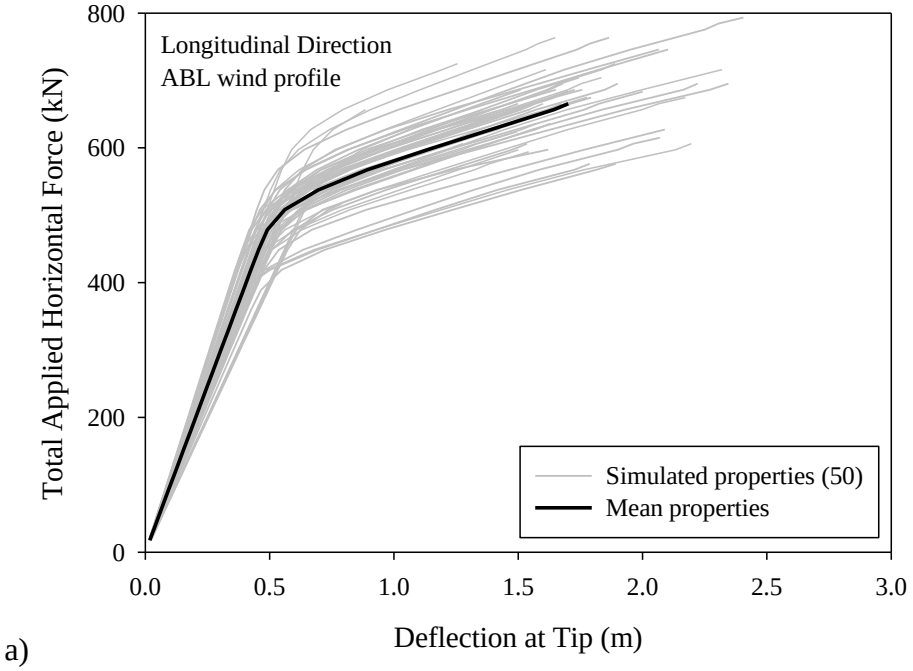

a)

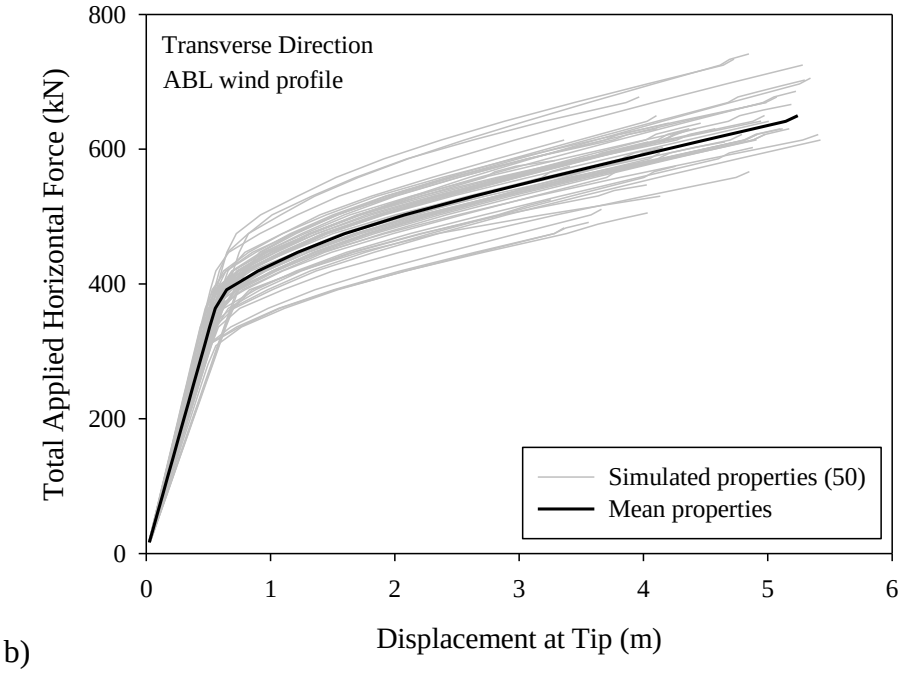

b)

Figure 4.5. Capacity curves resulting from uncertainty analysis (50 simulations) for the structural properties of the tower for ABL wind distribution in the a) longitudinal direction, and b) transverse direction.

4.3 Downburst wind loads

4.3.1 Application of a numerical stationary downburst simulation

The strong winds in a downburst outflow are the result of a cool air mass descending from the upper atmosphere coming into contact with the surface of the earth. This phenomenon results in a rolling vortex which translates outward from the center of the downburst (described as the point of touchdown), characterized by a gust front with strong winds over the height range of most man-made structures. Spatio-temporally varying wind fields from a simulation of a stationary downburst event (Hangan et al. 2003) were obtained and processed. As the downburst simulation was carried out at small scales, the simulation and output parameters were first converted to full-scale dimensions based on values describing the size and strength of the event. Figure 4.6 illustrates the size denoted by jet diameter, D_{jet}, the strength denoted by the jet velocity, V_{jet}, and the distance from the center of the downburst to a point of interest, r. The horizontal wind speed in the downburst outflow profile is provided from the simulation as a ratio to V_{jet}, and is notated as V_{hor}. The simulation time scale, t_s, representing the time step used in downburst simulation, differs from the time scale t for the full-scale; the conversion from t_s to t depends on the values of V_{jet} and D_{jet} (Hangan et al. 2003). A ratio, r/D_{jet}, is used for parametric investigation of downburst effects between different sizes of downbursts, rather than using a specific value of r, as the use of a specific value would not incorporate scaling with D_{jet}. Further description of the numerical downburst simulation can be found in Kim and Hangan (2007).

The use of a maximum wind speed at a reference height to describe the strength of a downburst event presents a difficulty in interpretation, as the shape of the wind speed profile with height varies with time, the size of the downburst, and the distance from downburst touchdown. A constant reference height selected to describe peak downburst winds will neither reflect the maximum wind speeds nor the relationship of wind speed with height for all downburst scenarios. This is in contrast to the approach taken for synoptic winds, as the widely-accepted ABL profile facilitates the use of a reference mean or gust wind speed at a height of 10 m in prescribed terrain to fully describe the magnitude and statistics of the wind load. Thus, direct comparison between a downburst

wind speed and ABL wind speed at identical heights cannot provide a meaningful description of the overall differences that may exist in wind loading on a structure. A parametric investigation of the effect of downburst parameters D_{jet} and V_{jet} on the structural response of the tower is therefore carried out in the following section and compared to those obtained for a traditional ABL wind profile.

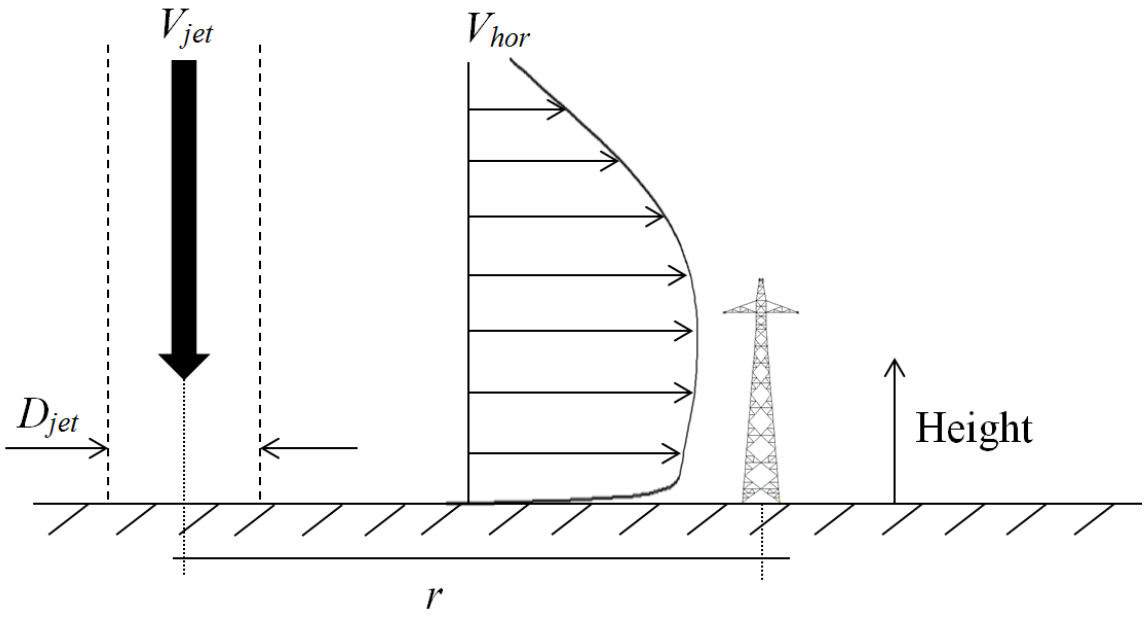

Figure 4.6. Elevation plot showing the parameters in the numerical downburst simulation (downburst outflow profile is scaled to r/D_{jet} = 1.3, D_{jet} = 500m).

The simulated downburst wind fields (Hangan et al. 2003) over the height of the tower are used to evaluate the downburst wind loading. Upon analyzing the entire set of simulated wind fields, it was found that the strongest horizontal wind speed (for the range of parameters considered over the height range of the tower) occurs at a distance from touchdown of r/D_{jet} = 1.3 at simulation time step t_s = 31; while other parameters are varied, this time step is used for all further parametric downburst scenario comparisons. Based on this position and time, the effect of D_{jet} on the horizontal wind profile normalized with respect to V_{jet} is shown in Figure 4.7a. It is shown that as D_{jet} increases, the curvature in the wind speed profile increases, resulting in a distribution resembling more of an ABL-type wind speed profile. The effects of r/D_{jet} on V_{hor}/V_{jet} for D_{jet} = 500

m are shown in Figure 4.7b, where it can be seen that while the magnitude of the wind speed is greatly affected, the variation in the shape of the profile is less.

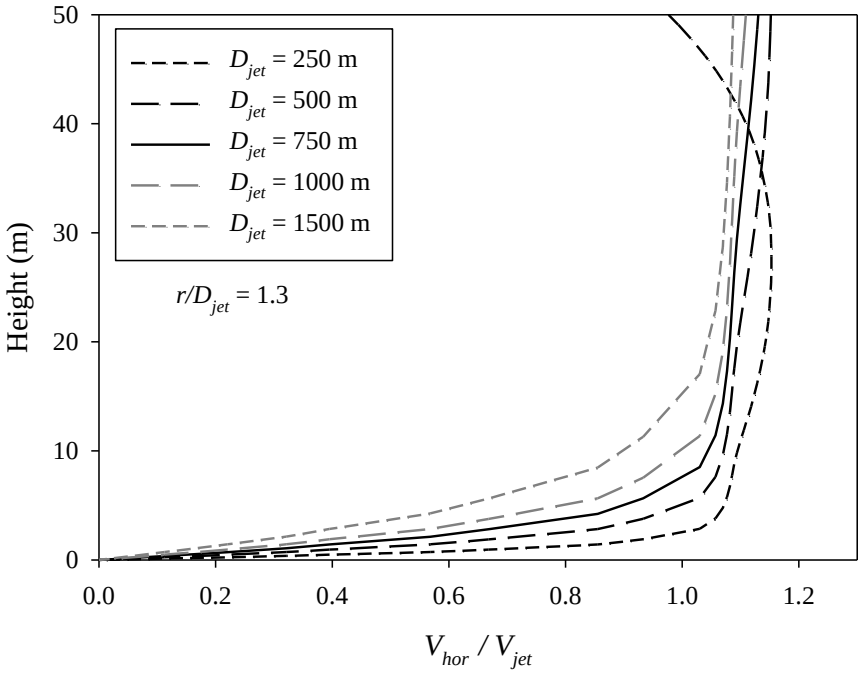

a)

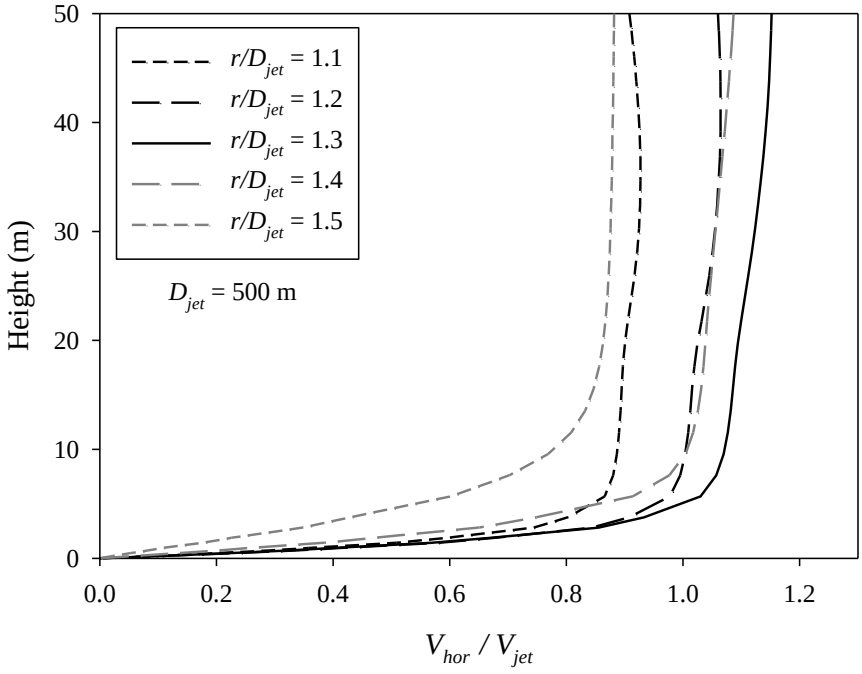

b)

Figure 4.7. Variation of horizontal velocity wind profiles with a) D_{jet}, and b) r/D_{jet}.

The numerical downburst simulation can also be used to compile a time history of wind speed at any height. The time histories of the horizontal wind speed at various heights are plotted in Figure 4.8 for a downburst defined by r/D_{jet} = 1.3, D_{jet} = 500 m, and V_{jet} = 70 m/s. The abscissa represents the time scale t for the full-scale which is calculated based on the values of t_s, V_{jet} and D_{jet} (Hangan et al. 2003); each time step (i.e., increment of t_s) for this set of parameters corresponds approximately to an increment of 3.5 s, with t_s = 0 representing the incipient of downburst touchdown. It is shown that the peak horizontal wind speeds at each of the heights occur at t approximately equal to 109 s. Figure 4.8 indicates that the downburst outflow maintains a constant speed following the passage of the gust front; this is due to the assumption of steady outflow in the numerical simulation which is a limitation of the downburst simulation and does not affect the estimation of peak responses. The wind speeds generated from the numerical downburst simulation are representative of mean peak wind speed, and accordingly gust effects are not considered in the analysis.

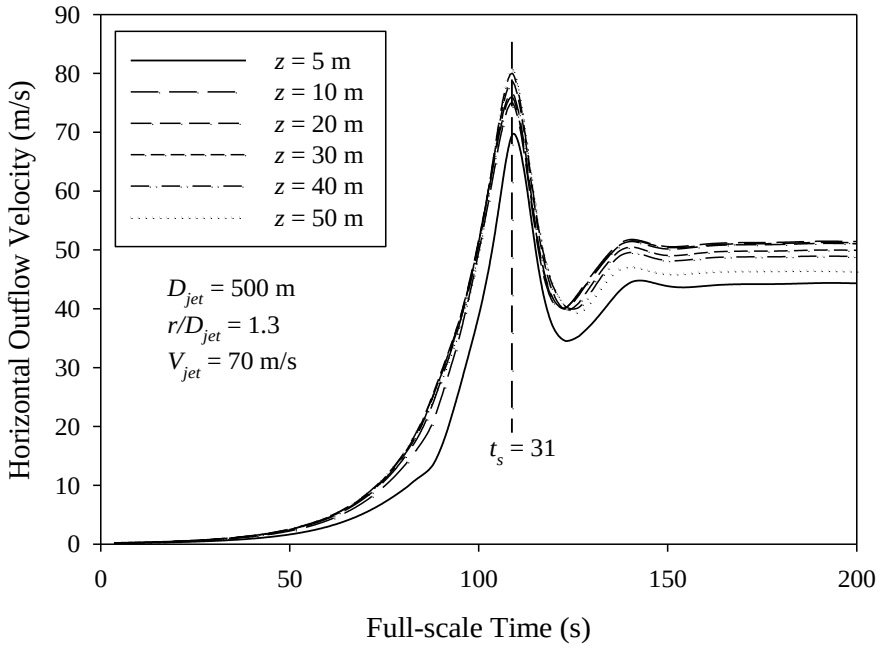

Figure 4.8. Horizontal outflow velocity time history at various heights in a downburst outflow.

4.3.2 Applied horizontal force due to downburst

It is considered that, by assigning values of 1.0 to G_t and G_c, that Eqs. (1) and (2) are applicable for calculating the downburst wind forces on the tower, although no advice on the treatment of wind loads resulting from HIW events is provided in CSA-2010. This approach is consistent with that taken in ASCE-74 for extreme wind loading. The wind load at each node in the structural model is calculated based on the horizontal component of the downburst wind profile, and are applied to the tower model in a similar fashion to the ABL and rectangular wind loads. The variation in the downburst wind speed along the length of the wires is included in the analysis, although the effects of this for the combination of downburst parameters and wind directions investigated here is quite small.

Based on the above consideration and by adopting the simulated downburst wind speed profile, the time history of the total applied horizontal force in the longitudinal direction due to downburst is evaluated as the sum of the applied downburst wind loads over the height of the tower. The total applied horizontal force is shown in Figure 4.9 for varying downburst parameters (i.e., D_{jet}, V_{jet}, and r/D_{jet}). The total horizontal applied force equals the base shear of the tower if the inertia force is negligible. It is shown in Figure 4.9a that for D_{jet} ranging from 250 m to 1500 m (commonly used to characterize microburst events), the peak of the total applied horizontal force experienced by the tower during a downburst passage decreases with increasing D_{jet}. This is due to the change in the wind speed profile over the height of the tower. The variation of the total applied horizontal force for varying r/D_{jet} is shown in Figure 4.9b, indicating that the peak load attains its maximum value for $r/D_{jet} = 1.3$; this is consistent with the examination of the wind speed profiles discussed for Figure 4.7a. It is therefore expected that the tower is likely to experience the greatest load effect for such a downburst scenario. The relation between the time history of the total applied horizontal force and V_{jet} shown in Figure 4.9c, which illustrates that the peak force varies directly with V_{jet}.

Similar plots of the total applied horizontal force in the transverse direction are shown in Figures 4.9d through 4.9f. For the calculation of these total applied horizontal forces, the wind loads on different portions of the wires were weighted by projected area and

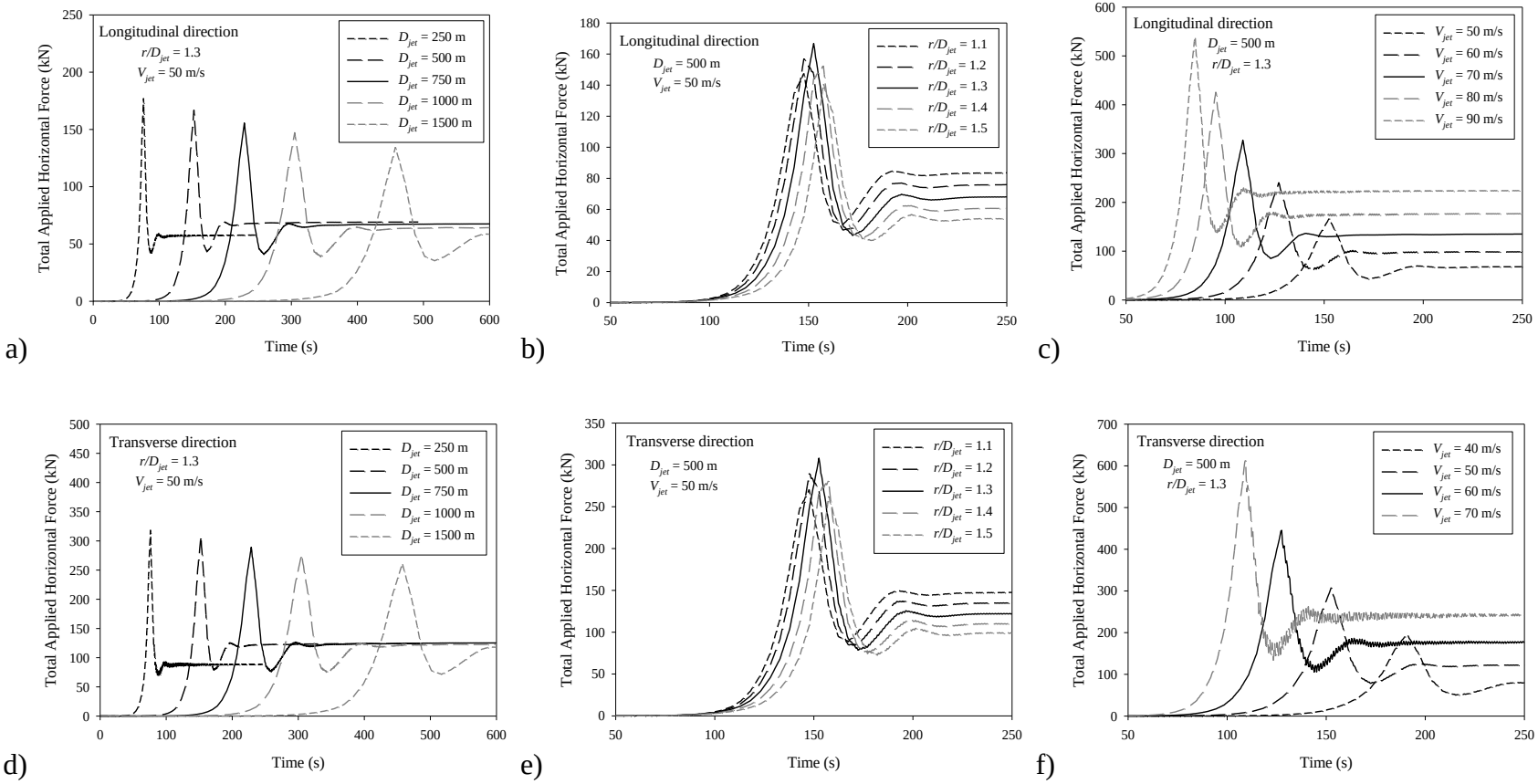

Figure 4.9. Time history of the total applied horizontal force due to downburst passage varying with a) effect of D_{jet} in the longitudinal direction, b) effect of r/D_{jet} in the longitudinal direction, c) effect of V_{jet} in the longitudinal direction, d) effect of D_{jet} in the transverse direction, e) effect of r/D_{jet} in the transverse direction, f) effect of V_{jet} in the transverse direction.

superimposed to generate a time history of loading on the entire wire, and were applied at the wire-tower connections. The trends shown in Figures 4.9d through 4.9f are consistent with those shown in Figures 4.9a through 4.9c, although the magnitude of loading for the transverse direction is much greater due to the contributions of the conductors and ground wire.

4.4 Capacity curves for downburst wind loading

4.4.1 Capacity curves from transient and NSP analyses

A nonlinear dynamic structural analysis for the tower is first carried out considering a transient downburst passage for a downburst scenario defined by parameters D_{jet} = 500 m, r/D_{jet} = 1.3. These parameters were selected as to reflect what is believed to be a common downburst size (D_{jet} = 500 m) and the distance r/D_{jet} at which the outflow exerts the most wind load on the structure (see Figure 4.9). The tower was loaded for various V_{jet} in the longitudinal and transverse directions. The obtained time history of the response in each direction is used to construct the force-deformation curves shown in Figure 4.10, where the ordinate represents the total applied horizontal force (wind load) and the abscissa denotes the displacement at the tip of the tower. The figures show the linear behaviour, the incipient of yield, the post-yield behaviour, and the unloading response provided the tower did not fail. The jaggedness on the unloading branch is due to both the vibration of the tower and the oscillation of the applied wind force (see Figure 4.10). The fact that the unloading does not result in total applied force equal to zero is because there is a sustained wind load following the passage of the downburst gust front, a consequence of the limitation of the downburst model discussed in Figure 4.8. Figure 4.10 shows that for some of the selected V_{jet}, the downburst passage did not initiate collapse, but was strong enough to result in significant amounts of permanent deformation. V_{jet} = 100 m/s resulted in the tower collapse if the tower is loaded longitudinally, while V_{jet} = 75m/s resulted in the tower collapse if the tower is loaded transversally. For the downburst parameters illustrated in Figure 4.10, it was found that yield occurs for a V_{jet} of approximately 86 m/s and 61 m/s in the longitudinal and

transverse directions, respectively, and that collapse occurred for a V_{jet} of approximately 100 m/s and 75 m/s in the longitudinal and transverse directions, respectively.

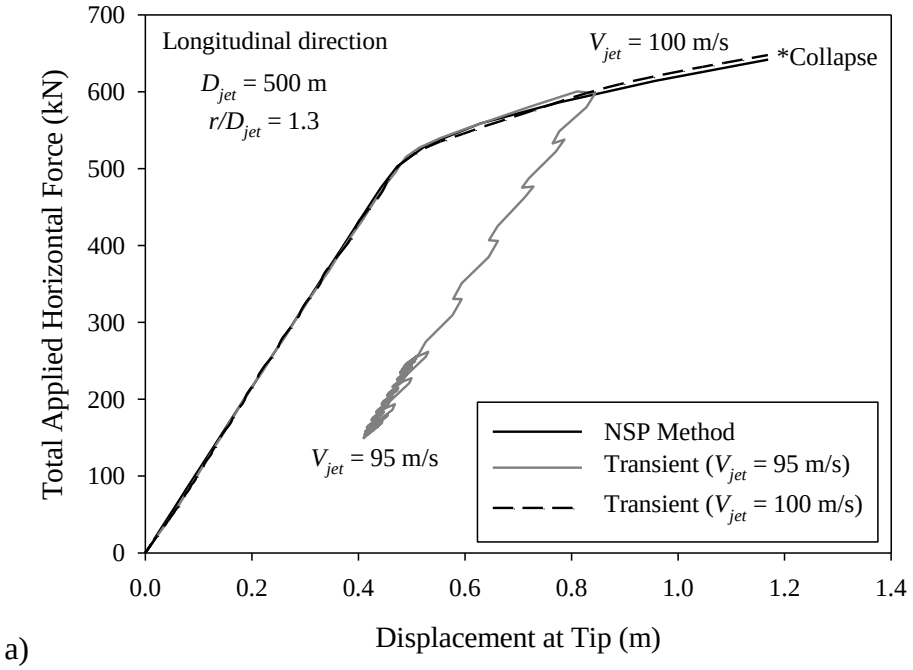

a)

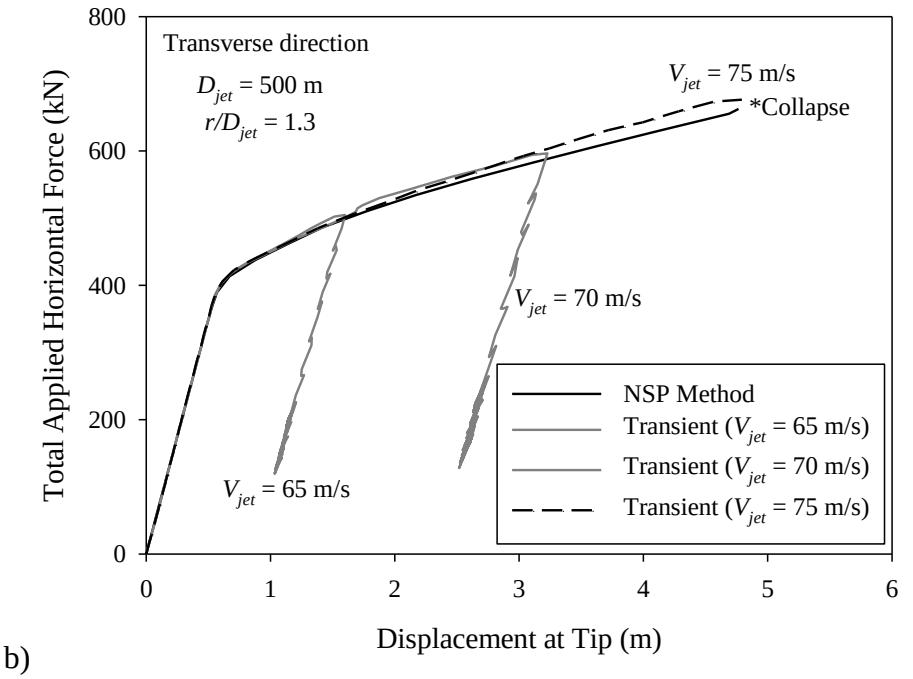

b)

Figure 4.10. Force-deformation curves for transient downburst passage with varying V_{jet} and results from NSP method for a) longitudinal direction, and b) transverse direction.

Rather than carrying out the transient analysis, which requires the knowledge of the time-varying wind speed profile, it is advantageous to carry out the NSP analysis for a single fixed wind profile if the obtained capacity curve for the latter approximates the force-deformation curve of the former. For such a purpose, the wind profile corresponding to the peak total applied horizontal force is considered, and the obtained capacity curves are compared for various downburst parameters in Figure 4.10. The last point on the curves represents the analysis result obtained before nonconvergence was observed in the NSP analysis. Comparison of the results shows that the use of the NSP analysis with the selected wind speed profile to evaluate the capacity curve for each direction of loading provides a good approximation. Based on the results shown in Figure 4.10, it was deemed acceptable to proceed using the NSP method to carry out a parametric investigation of capacity curves of the tower to the downburst parameters.

4.4.2 Sensitivity of capacity curves to downburst parameters

Capacity curves, such as those shown in Figure 4.10, are a convenient way of comparing the effects of various stages of downburst outflow on the tower. Wind speeds are traditionally referenced to a height of 10 m, which is an appropriate method when the mean wind profile is constant over the duration of an event. However, as was shown in Figure 4.7, the wind profile and duration in a downburst event depends on both the size of the event, D_{jet}, and the distance between the structure and the downburst touchdown, r/D_{jet}. Thus, reference to wind speed at a single height alone is insufficient to characterize its potential effect on a structure.

The same procedure used to evaluate the capacity curves for the ABL and rectangular wind profiles is carried out for the downburst profiles shown in Figures 4.7a and 4.7b; capacity curves in the longitudinal direction for a range of combinations of downburst parameters (r/D_{jet}, D_{jet}) are evaluated and shown in Figures 4.11a and 4.11b. The capacity curves for the ABL and rectangular wind profiles are also included in the figure for comparison. It is shown in Figure 4.11a that the tower experiences yield at similar values of deflection for each D_{jet} examined. However, the amount of deformation which the tower undergoes in the post-yield range is much more dependent on the loading profile. As D_{jet} increases, the loading profile increases in curvature over the lower half of

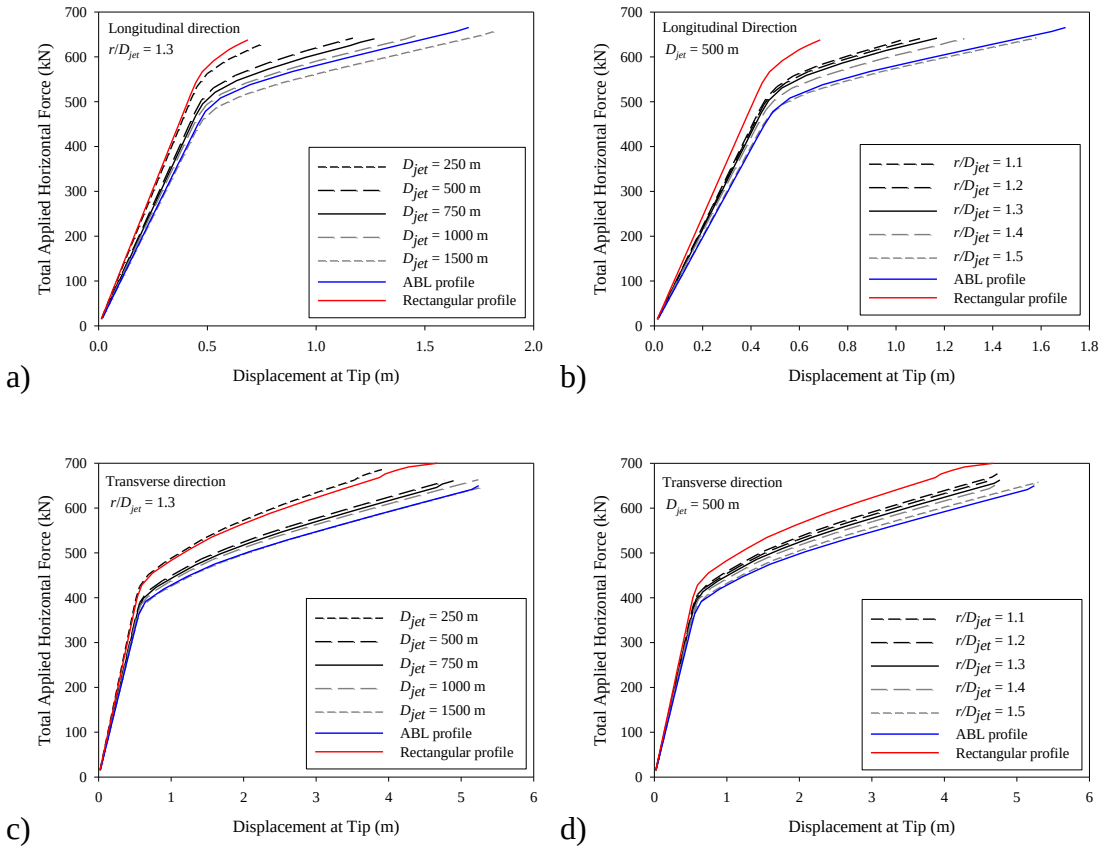

Figure 4.11. Capacity curve showing the a) effect of D_{jet} in the longitudinal direction, b) effect of r/D_{jet} in the longitudinal direction, c) effect of D_{jet} in the transverse direction, d) effect of r/D_{jet} in the transverse direction.

the tower (see Figure 4.7a). That is, outflow profiles characterized by smaller downbursts tend to load the tower in a more uniform fashion at this distance from downburst touchdown. The low amount of post-yield deformation observed in Figure 4.11a for D_{jet} = 250 m is due to the reduction in wind speed in the upper portion of the tower, as illustrated in Figure 4.7a. Similar comparisons are drawn for the capacity curves in Figure 4.11b and the downburst outflow profiles shown in Figure 4.7b, although the loading profiles shown for different r/D_{jet} do not vary as much in shape as those for different D_{jet}. It is shown that for the range of downburst scenarios considered, with the exception of D_{jet} = 1500 m, that the downburst capacity curves in the longitudinal direction are enveloped by those estimated using the ABL and rectangular wind profiles. Generally, the results shown in Figures 4.11a and 4.11b indicate that as

the wind loading profile becomes increasingly uniform in shape, the yield capacity of the tower increases although post-yield deformation decreases significantly. This implies that although the maximum capacity of the tower is relatively consistent (within 4% among all the considered downburst scenarios), the post-yield behaviour of the tower is somewhat sensitive to wind load distribution.

Using the same combinations of downburst parameters (r/D_{jet}, D_{jet}) used for Figures 4.11a and 4.11b, the estimation of the capacity curves in the transverse direction is carried out. The obtained curves are shown in Figure 4.11c and 4.11d and compared to those for the ABL and rectangular wind profiles. Similarly to the longitudinal direction, the tower experiences yield at similar values of displacement in the transverse direction for each D_{jet} examined (see Figure 4.11c), with the case for D_{jet} = 250 m standing out due to the low wind speed at conductor height (see Figure 4.7a). The deflection at maximum capacity for the transverse direction is much less dependent on the shape of the wind load distribution than that for the longitudinal direction, and this is again due to the relatively large contributions from the wires. Due to the loading contributions from the wires, the transverse direction loading, regardless of profile, is characterized by large loads in the upper portion of the tower. This load distribution results in a greater amount of deformation in the post-yield range that is observed in Figures 4.11c and 4.11d. It is shown that for the range of downburst scenarios considered, that the downburst capacity curves in the transverse direction are enveloped by those estimated using the ABL and rectangular wind profiles.

To better appreciate the characteristics of capacities of the tower at incipient of yield and incipient of collapse, their values are estimated based on the capacity curves shown in Figure 4.11. The calculated capacities are used to estimate the ratios of the yield and maximum capacities under downburst loading to the rectangular and ABL wind profiles which are tabulated in Table 4.5. The values suggest that the ABL wind profile provides a conservative (or very close) estimate of the yield capacity of the tower under downburst loading, while the maximum capacity in the longitudinal and transverse directions are slightly underestimated (within 5%) and overestimated (within 6%), respectively. The rectangular wind profile provides good estimates of the yield and maximum capacities for

smaller downburst events, as well as the maximum capacities in the longitudinal direction for each downburst scenario. A conservative estimate of the tower yield capacity under large downburst events, and capacity in the transverse direction in general, is made using the ABL wind profile.

Table 4.5. Ratios of yield and maximum capacities (kN) under downburst wind loading to those associated ABL and rectangular wind profiles.

	r/D_{jet} = 1.3							
	Capacity Ratio: Downburst to ABL				Capacity Ratio: Downburst to Rectangular			
	Longitudinal		Transverse		Longitudinal		Transverse	
D_{jet} (m)	Yield	Maximum	Yield	Maximum	Yield	Maximum	Yield	Maximum
250	1.05	0.95	1.12	1.06	0.96	0.99	1.02	0.98
500	0.97	0.96	1.05	1.02	0.90	1.01	0.96	0.95
750	1.02	0.96	1.05	1.02	0.94	1.00	0.95	0.94
1000	1.00	0.97	1.02	1.02	0.92	1.01	0.93	0.95
1500	0.98	0.99	1.00	0.99	0.90	1.03	0.90	0.92
	D_{jet} = 500 m							
	Longitudinal		Transverse		Longitudinal		Transverse	
r/D_{jet}	Yield	Maximum	Yield	Maximum	Yield	Maximum	Yield	Maximum
1.1	1.02	0.96	1.08	1.04	0.94	1.00	0.98	0.97
1.2	1.00	0.96	1.04	1.02	0.92	1.00	0.94	0.94
1.4	1.03	0.96	1.04	1.00	0.94	1.00	0.94	0.93
1.5	0.99	0.98	1.01	1.01	0.91	1.02	0.92	0.94

4.5 Conclusions

Analyses have been carried out to estimate the nonlinear inelastic response of a self-supported lattice transmission tower under ABL, rectangular (uniform), and downburst wind profiles. For the analysis, the tower is represented by a 3-D numerical model, and the details of the response to wind loading during a simulated downburst passage are assessed. The nonlinear static pushover method is used to develop the capacity curve of the tower, which is represented using the total applied horizontal wind load (base shear) versus the displacement of the tip of the tower. The following conclusions are drawn from the study:

1. The capacities of the tower at incipient of yield and collapse depend on the wind loading profile. Generally, the capacities to sustain wind load for the ABL wind profile are lower than those for the rectangular wind profile. The uncertainty in the capacities due to material properties and geometric variables is not very significant; the coefficient of variation of the capacities is less than 10%, which is significantly smaller than that associated with the total wind load effect.

2. The wind load on the conductors and ground wire significantly affect the capacity curves in the transverse direction (as compared to the longitudinal direction). The critical wind speed for the considered tower is associated with the transverse direction. The capacity curves obtained for the ABL and rectangular wind profiles can be used as approximate lower and upper bounds, respectively, for the capacity curve for important downburst wind profiles.

3. Downbursts which are smaller in size result in the tower experiencing yield at a higher base shear, as well as less deformation with increasing wind speed. Downbursts which are greater in size initiate yield at a lower horizontal wind load, but allow for more deformation in the post-yield range prior to collapse. The characteristics of the capacity curve for the ABL wind load distribution resembles that for a downburst having a jet diameter between 1000 m and 1500 m in terms of yield and maximum capacity. As the size of the downburst increases, the capacity curve becomes steeper in both the elastic and inelastic range.

4. Based on the above observations, it is recommended that the capacity curve estimated under the rectangular wind profile can be used as a proxy for the capacity curve under downburst wind if the downburst size is small, and that the capacity curve estimated under the ABL wind profile can be used as a proxy for the capacity curve under downburst wind if the downburst size is large. The consideration of these conditions in practice simplifies the performance assessment of towers under downburst wind loading, as well as provides advice on the necessary capacity for towers to resist downburst winds in the design process.

4.6 Acknowledgements

The downburst wind fields were made available by Dr. H.M. Hangan of the WindEEE Research Institute and Department of Civil and Environmental Engineering at the University of Western Ontario. The financial support from the National Sciences and Engineering Research Council of Canada (NSERC) is gratefully acknowledged.

4.7 References

American Society of Civil Engineers (ASCE) (2010). "Guidelines for Electrical Transmission Line Structural Loading (3rd edition)." ASCE Manuals and Reports on Engineering Practice No. 74, Reston, VA, USA.

ANSYS® (2007). ANSYS Multiphysics, Release 9.0. ANSYS Inc., Canonsburg, PA.

Banik, S.S., Hong, H.P. and Kopp, G.A. (2008). "Assessment of tornado hazard for spatially distributed systems in southern Ontario." *J. Wind Eng. Ind. Aerodyn*., 96(8-9), 1376-1389.

Banik, S.S., Hong, H.P. and Kopp, G.A. (2010). "Assessment of capacity curves for transmission line towers under wind loading." *Wind Struct*., 13(1), 1-20.

Bartlett, F.M., Hong, H.P. and Zhou, W. (2003). "Load factor calibration for the proposed 2005 edition of the National Building Code of Canada: Statistics of loads and effects." *Can. J. Civ. Eng*., 30(2), 429-439.

Canadian Standards Association (CSA) (2010). "Design criteria of overhead transmission lines." CAN/CSA-C22.3 No. 60826-10, CSA, Toronto, Canada.

Darwish, M.M. and El Damatty, A.A. (2011). "Behaviour of self supported transmission line towers under stationary downburst loading." *Wind Struct*., 14(5), 481-498.

Davenport, A.G. (1979). "Gust response factors for transmission lines." *Proc. of the 5th International Conference on Wind Engineering*, Fort Collins, CO, USA, 899-909.

Durst, C.S. (1960). "Wind speeds over short periods of time." *Met. Mag*. 89, 181-186.

Ellingwood, B.R., Galambos, T.V., MacGregor, J.G. and Cornell, C.A. (1980). "Development of a probability based load criterion for American National Standard A58." National Bureau of Standards, Washington D.C., USA.

Fujita, T.T. (1976). "Spearhead Echo and Downburst near the Approach end of a John F. Kennedy Airport Runway, New York City." SMRP Research Paper No. 137, University of Chicago.

Fujita, T.T. (1985). "The Downburst: Microburst and Macroburst." SMRP Research Paper No. 210, University of Chicago.

Hangan, H., Roberts, D., Xu, Z. and Kim, J.-D. (2003). "Downburst simulations. Experimental and numerical challenges." *Proc. of the 11th International Conference on Wind Engineering*, Lubbock, TX, USA.

Hangan, H., Savory, E., El Damatty, A., Galsworthy, J. and Miller, C. (2008). "Modeling and prediction of failure of transmission lines due to high intensity winds." *Proc. of the 2008 Structures Congress (ASCE)*, Vancouver, BC, Canada.

Haukaas, T. and Der Kiureghian, A. 2006. Strategies for finding the design point in non-linear finite element reliability analysis. *Prob. Eng. Mech*., 21, 133-147.

Holmes, J.D. and Oliver, S.E. (2000). "An empirical model of a downburst." *Eng. Struct*., 22(9), 1167-1172.

Holmes, J.D., Hangan, H.M., Schroeder, J.L., Letchford, C.W. and Orwig, K.D. (2008). "A forensic study of the Lubbock-Reese downdraft of 2002." *Wind Struct*., 11(1), 137-152.

Kim, J. and Hangan, H. (2007). "Numerical simulation of impinging jets with application to downbursts." *J. Wind Eng. Ind. Aerodyn*.,, 95(4), 279-298.

Krawinkler, H. and Seneviratna, G.D.P.K. (1998). "Pros and cons of a pushover analysis of seismic performance evaluation." *Eng. Struct*., 20(4-6), 452-464.

Lee, P.-S. and McClure, G. (2007). "Elastoplastic large deformation analysis of a lattice steel tower structure and comparison with full-scale tests." *J. Constr. Steel Res*., 63(5), 709-717.

Lin, W.E., Savory, E., McIntyre, R.P., Vandelaar, C.S. and King, J.P.C. (2012). "The response of an overhead electrical power transmission line to two types of wind forcing." *J. Wind Eng. Ind. Aerodyn*., 100(1), 58-69.

Lombardo, F.T. (2009). "Analysis and interpretation of thunderstorm wind flow and its effect on a bluff body". Ph.D. Dissertation, Texas Tech University.

Mara, T.G., Galsworthy, J.K. and Savory, E. (2010). "Assessment of vertical wind loads on lattice framework with application to thunderstorm winds." *Wind Struct*., 13(4), 413-431.

Masters, F.J., Vickery, P.J., Bacon, P. and Rappaport, E.N. (2010). "Toward objective, standardized intensity estimates from surface wind speed observations." *Bull. Amer. Met. Soc.*, 12, 1665-1681.

McCarthy, P. and Melsness, M. (1996). "Severe Weather Elements Associated with September 5, 1996 Hydro Tower Failures Near Grosse Isle, Manitoba, Canada." Environment Canada, Winnipeg, Canada.

Orwig, K.D. and Schroeder, J.L. (2007). "Near-surface wind characteristics of extreme thunderstorm outflows." *J. Wind Eng. Ind. Aerodyn*.,, 95(7), 565-584.

Savory, E., Parke, G.A.R., Zeinoddini, M., Toy, N. and Disney, P. (2001). "Modelling of tornado and microburst-induced wind loading and failure of a lattice transmission tower." *Eng. Struct*., 23(4), 365-375.

Shehata, A.Y., El Damatty, A.A. and Savory, E. (2005). "Finite element modeling of transmission line under downburst wind loading." *Fin. Elem. Anal. Des*., 42(1), 71-89.

Shehata, A.Y. and El Damatty, A.A. (2008). "Failure analysis of a transmission tower during a microburst." *Wind Struct*., 11(3), 193-208.

Wood, G.S., Kwok, K.C.S., Motteram, N.A. and Fletcher, D.F. (2001). "Physical and numerical modelling of thunderstorm downbursts." *J. Wind Eng. Ind. Aerodyn*., 89(6), 535-552.

Chapter 5

5 Effect of relative orientation on the capacity of a transmission tower under downburst loading

The wind speed profile over the height of a structure in high intensity wind (HIW) events, such as downbursts and thunderstorm gust fronts, differs from that associated with traditional atmospheric boundary layer (ABL) winds. Current design codes for lattice transmission towers contain only limited advice on HIW, and structural design is often carried out using a procedure developed for ABL winds. Furthermore, the load effects due to the relative orientation of a tower to HIW events are not well understood. This chapter assesses the yield and maximum capacity of a self-supported transmission tower under downburst wind loading, including the effects of geometric and material nonlinear behavior. The force-deformation relation, also known as the capacity curve, for a self-supported transmission tower is obtained for a range of wind directions and represents the relationship between the total base shear force and the displacement of the tip. The capacity curve of a tower is a convenient way to assess a tower design under HIW, as the definition of a reference wind speed between downburst events is cumbersome due to the number of variables involved. Capacity curves based on three downburst scenarios are obtained for oblique wind directions, and their differences are shown to the related to the shape of the loading profile. Therefore, the capacity of a transmission tower is related to the size and location of a downburst. It is shown that the lowest yield capacity tends to occur at a wind direction of approximately 45°, and that the tower has greater yield and maximum capacities when the loading is concentrated at the mid-height height of the tower as opposed to the upper portion.

5.1 Introduction

Transmission structures play an important role in the efficient transmission and distribution of electricity across great distances. Extreme wind events are the most common cause of failure or collapse, which includes strong synoptic events (e.g., strong winds during the winter months) and localized HIW events, which are usually attributed to convection (e.g., thunderstorm gust front, downburst outflow). These winds differ in

both meteorological and structural loading characteristics, however each of them exert high loads on transmission structures. An example of this was the failure of 19 towers in the southern portion of the Manitoba Hydro power transmission corridor due to multiple downburst events (McCarthy and Melsness 1996). Some locations in Manitoba were without power for as much as 5 days following these failures, resulting is significant social and financial implications for this region of Manitoba. In light of this event, an initiative was taken to better understand the characteristics and mechanisms of HIW events (Hangan et al. 2008, Banik et al. 2008), their load effects on towers (Mara et al. 2010, Lin et al. 2012), and the response of transmission structures under downburst winds (Shehata and El Damatty 2008, Banik et al. 2010, Darwish and El Damatty 2011).

The term 'downburst' was coined by Fujita (1976) to describe a strong convective downdraft which impinges on the surface of the earth, resulting in an outburst of strong winds close to ground level. The second characteristic, strong winds close to ground level, results in direct implications to man-made structures. However, due to their relative rarity and localized nature, it is uncommon to observe a downburst event at full scale, let alone have wind speed measurement devices in place to record data. A rare exception to this is the microburst recorded at Andrews Air Force Base on 1 August 1983 (see Fujita 1985), which indicated a peak wind speed of approximately 67 m/s (130+ kts) at a height of 4.9 m on the leading side of the outflow. The runway anemometer records for this event provide a time history of the wind speed and direction throughout the downburst event. This was a benchmark observation which illustrated that downbursts are capable of generating extreme winds close to ground level, and provided a recorded magnitude to accompany forensic damage surveys.

Due to the paucity of full scale downburst data, the majority of work in the wind engineering community has proceeded by adopting a numerical approach to modeling downburst winds, while using the few recorded full scale events (Fujita 1985, Orwig and Schroeder 2007) for model calibration and validation. A numerical downburst simulation based on a stationary impinging jet was carried out by Hangan et al. (2003), and was shown to agree well with full scale downburst wind speed measurements (Kim and Hangan 2007). This was a benchmark simulation, as it provided the first spatio-temporal

downburst outflow model which could be applied to structures. The numerical downburst wind fields generated by Hangan et al. (2003) are used in the present study.

It is important to note that, unlike for ABL winds where the mean wind speed profile increases monotonically over the height of the tower and is consistent in time and space, the wind speed profile in a downburst outflow varies with downburst size, position (relative to a fixed structure), and time. Thus, the wind speed profile experienced by a fixed structure is transient. This complicates a practical definition of a height at which to reference the strength of downburst wind speeds, which has implications for codified design. Therefore, a simplification of design verification for structures under downburst wind loading is worth exploring. One approach that can be taken is the use of the nonlinear static pushover (NSP) method, which was used to evaluate the capacity of a 2-D transmission tower under a variety of wind loading conditions by Banik et al. (2010). It was shown that the capacities of the tower at the incipient of yield and collapse are influenced by the shape of the wind speed profile over the height of the tower. More importantly, it was shown that the capacities estimated through the NSP method are representative of the peak effects of short-duration winds (i.e., 3-second gusts). As the failure of a tower depends directly on the behavior of its force-deformation relationship, or capacity curve, the evaluation of these capacities are of importance to assessment and design.

5.2 Modeling of transmission tower and wind loads

5.2.1 Numerical model of transmission tower

The effects of downburst winds are assessed for a self-supported lattice transmission tower design provided by Manitoba Hydro. The commercial finite element analysis program ANSYS was selected for its capability in dealing with the nonlinear geometric and material properties of the structural steel of the tower. The tower members are modeled as 2-node nonlinear 3-D frame elements, assuming that rigid connections are representative of the multi-bolted moment-resisting connections found in the prototype. The masses of the conductors and ground wires are applied to the tower as lumped masses at the nodes corresponding to the connections. The material nonlinearity of the

tower members is modeled using bilinear elastoplastic material properties, and the geometric nonlinearities (i.e., buckling effects) are accounted for through a large deformation analysis. A total of 959 elements and 405 nodes are used in the numerical model of the tower. An isometric elevation and plan view of the tower model is shown in Figure 5.1.

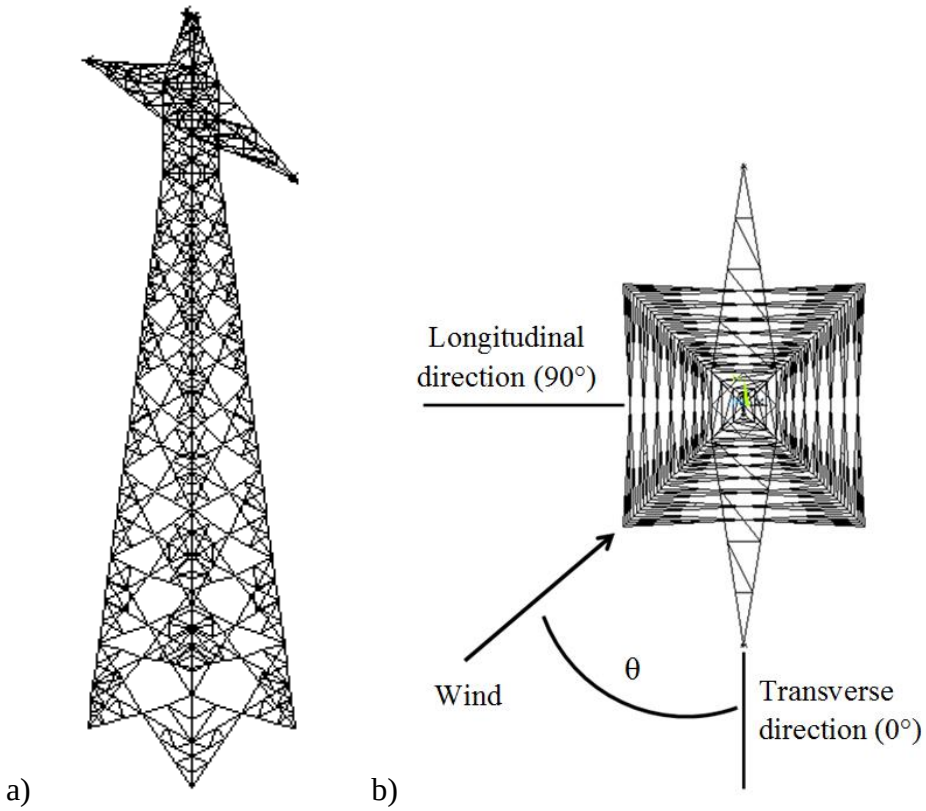

Figure 5.1. Self-supported transmission tower in a) isometric elevation view and b) plan view.

5.2.2 Wind load provisions in codes

Design wind loads for transmission towers under synoptic winds are specified in CAN/CSA C22.3 No. 60826-10 (referred to herein as CSA-2010) (CAN/CSA 2010), as well as ASCE Manual No. 74 (referred to herein as ASCE-74) (ASCE 2010). CSA-2010 adopts the International Electrotechnical Commission (IEC) Standard 60826:2003 (IEC 2003) for design criteria of overhead transmission lines. The loading application used in this analysis reflects that recommended in CSA-2010.

The prototype tower is divided into 11 representative sections, or panels, over which the aerodynamic parameters do not significantly change. As transmission structures are often located in open terrain, an exposure representative of open country (as specified in CSA-2010) is considered, which corresponds to a power law coefficient of 0.16 for mean wind speed. It should be noted that the CSA-2010 reference wind speed corresponds to a 10-minute mean wind speed at 10 m height in open country terrain.

The wind loads on each of the panels are calculated as

$$A_t = 0.5\tau\mu V_R^2 G_t \left(1 + 0.2\sin^2(2\theta)\right)\left(S_{t1}C_{xt1}\cos^2\theta + S_{t2}C_{xt2}\sin^2\theta\right) \quad (5.1)$$

where A_t (N) is the total wind loading on the panel in the direction of the wind; τ is an air density correction factor taken to be 1; μ is the density of air taken to be 1.225 kg/m^3; V_R (m/s) is the reference wind speed based on a 10-minute averaging period at 10 m height in open country terrain; θ is the angle of attack (yaw angle) illustrated in Figure 5.1; S_{ti} (m^2) is the total surface area projected normally on the corresponding i-th face, i = 1 and 2 (see Figure 5.1); C_{xti} is the drag coefficient for the corresponding i-th face; and G_t is a combined wind factor accounting for roughness of terrain and height of the panel. In this case, faces 1 and 2 correspond to the transverse and longitudinal faces of the tower, respectively. The wind loading on the conductor and ground wire lines are calculated such that

$$A_c = 0.5\tau\mu V_R^2 G_c G_L d L C_{xc}\sin^2\Omega \quad (5.2)$$

where A_c (N) is the total load on the line; C_{xc} is the drag coefficient of the line taken to be 1.0; G_c is the combined wind factor for the line; G_L is the span factor based on the length of the span; d (m) is the diameter of the line; L (m) is the wind span of the wires; and Ω is the angle of attack (yaw angle) between the wind direction and the wires. If there is no line angle between consecutive towers (i.e., consecutive towers are parallel), Ω equals (90-θ)°. As there are no commonly accepted equations available for the evaluation of wind loads under downburst, Eq. (5.1) and (5.2) are used in conjunction with a simulated downburst wind profile over the height of the tower as described in the following section.

5.2.3 Downburst wind loads

Downbursts are characterized by strong winds at low levels, which are a result of a cool mass of air descending from the upper atmosphere impinging on the surface of the earth. This results in a gust front radiating outwards from the center of downburst touchdown. The spatio-temporally varying wind fields simulated by Hangan et al. (2003) were obtained and processed, and the simulated downburst wind field described in Kim and Hangan (2007) is used in this study. The downburst wind field is characterized by the jet diameter, D_{jet}, the jet velocity, V_{jet}, and the distance from touchdown to the point of interest, r. Based on these parameters, a horizontal wind profile having speeds V_{hor} is defined. As the spatial characteristics of the simulated wind fields are a function of D_{jet} and r, it is convenient to express the distance from touchdown to the point of interest as r/D_{jet}. The magnitude of the wind speed is a function of V_{jet}. The parameters relevant to the downburst simulation are shown in Figure 5.2.

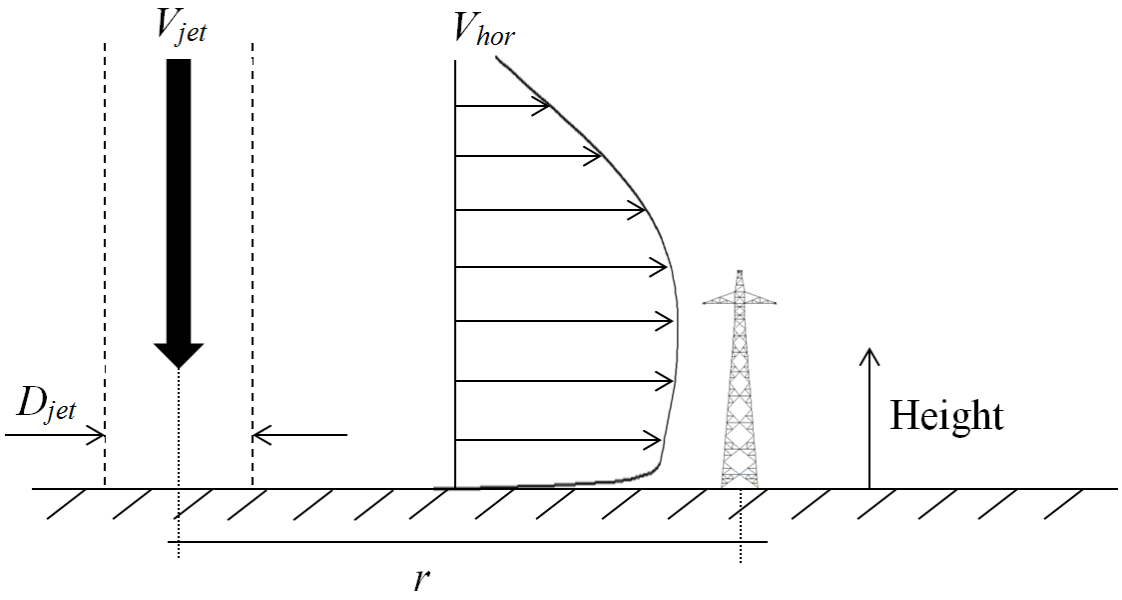

Figure 5.2. Elevation view of tower showing downburst touchdown and outflow (outflow profile is scaled relative to downburst having D_{jet} = 500 m).

The simulated downburst outflow profiles over the height of the tower are used to evaluate the capacity of the tower under downburst wind loading. The position of the downburst was selected by identifying the position at which the horizontal wind speed

was the greatest. Following an analysis of the simulated wind fields, it was found that the strongest horizontal wind speed occurs at a distance from touchdown of r/D_{jet} = 1.3 at the (simulation) time step 31. At this time, the wind loads on the tower-line system are the greatest (see Figure 4.8). This time step in the downburst outflow provides the base configuration for comparison of the capacity of the tower under downburst winds to that under ABL and rectangular winds. Based on this r/D_{jet} position and time step of the outflow, the wind profile over the height of the structure was extracted and plotted in Figure 5.3 for various D_{jet}. Note that Figure 5.3 is to scale.

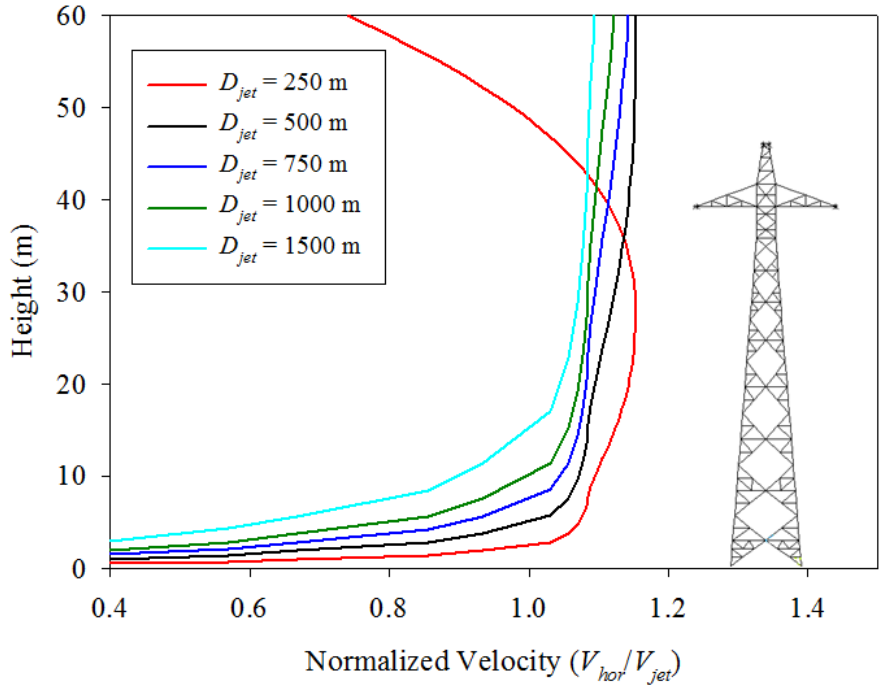

Figure 5.3. Downburst profiles for varying D_{jet} with tower shown for scale.

In each analysis case, the response of the tower corresponds to the time step at which the peak outflow wind speed is acting on the tower structure. The position parameter corresponding to the downburst acting on the tower is defined as $(r/D_{jet})_T$. The wind loads on the wires vary with wind direction and downburst location, and the distance between any point i on the wire is defined as $(r/D_{jet})_{Ci}$. The contributions of the wind on the wires were considered over half the wind span from the tower of interest, which results in a loading span of 244 m on either side of the tower. The sign convention is

shown in Figure 5.4, which is not depicted to scale in the interest of showing the details of the towers and wires.

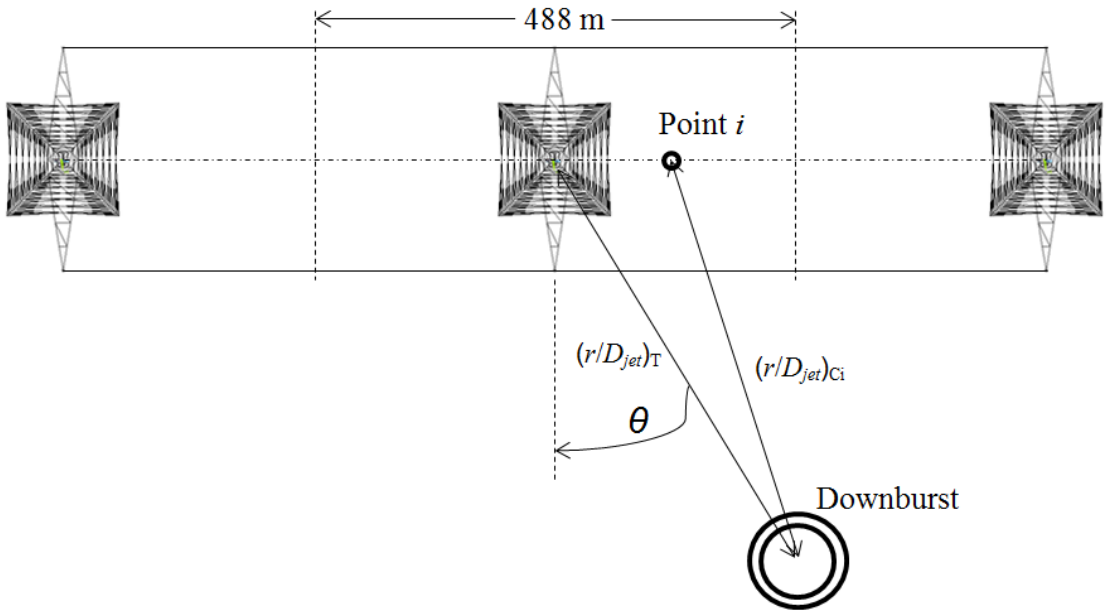

Figure 5.4. Plot of transmission tower and lines showing the naming convention for downburst profiles used in the analysis.

As the wind profile during a downburst is heavily dependent on the size of the downburst, D_{jet}, the profiles corresponding to several D_{jet} are shown in Figure 5.3. The results presented later in this chapter focus on three downburst scenarios: scenario 1 is defined by D_{jet} = 250 m at $(r/D_{jet})_T$ = 1.3; scenario 2 is defined by D_{jet} = 500 m at $(r/D_{jet})_T$ = 1.3; and scenario 3 is defined by D_{jet} = 1000 m at $(r/D_{jet})_T$ = 1.3. The wind profiles for each location *i* along the wires are taken from the wind profiles at the spacing intervals available in the numerical spacing (i.e., $0.05D_{jet}$). For example, for downburst scenario 1 at θ = 0°, $(r/D_{jet})_T$ = 1.3 while $(r/D_{jet})_{Ci}$ at mid-span =1.6; this results in a lower wind speed on portions of the wires further from the tower. The same value of $(r/Djet)_{Ci}$ is used for each set of wires (windward conductors and leeward conductors) as their separation is negligible compared to the spatial dimensions of the downburst. The downburst scenarios are notated as DB1, DB2 and DB3 for scenarios 1, 2, and 3, respectively.

5.3 Capacity curves for the transmission tower

5.3.1 Capacity curves using the NSP method

The NSP method is a widely used analysis technique to evaluate the performance and capacity of structures under seismic loading (e.g., Krawinkler and Seneviratna 1998), and more recently has been used for horizontal point load (Lee and McClure 2007) and wind load (Banik et al. 2010) applications. Banik et al. (2010) showed that the capacity curve obtained using the NSP method provides a good approximation of that obtained through nonlinear incremental dynamic analysis, and that the resulting capacity curves represent the peak wind load effects on the structure. Therefore, the responses of the tower can be viewed as representative of the peak wind load effects for short-duration (i.e., 3-second gust) wind speeds. Through the NSP method, the applied forces are monotonically increased, while a constant loading profile, in this case a wind loading profile, is maintained. An example capacity curve for a nonlinear inelastic system is shown in Figure 5.5.

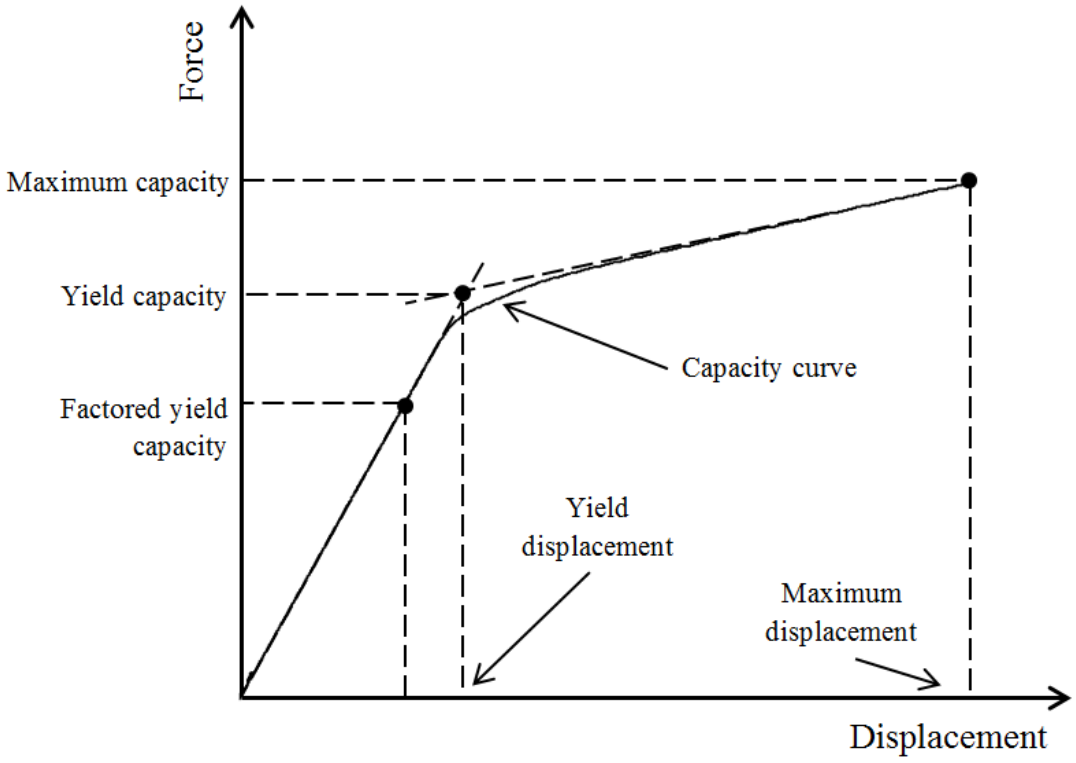

Figure 5.5. Example capacity curve for a nonlinear inelastic system.

The NSP method is applied here to evaluate the capacity curve of the tower, which identifies the yield and maximum (or ultimate) capacities of the tower. The capacity curves presented reflect the relationship of the total applied horizontal wind load to the displacement of the tip of the tower. The total applied horizontal wind load equals the base shear if it is assumed that inertial forces are negligible. The capacity curves are approximated as a bilinear system to estimate the yield capacity, which is defined as the point of intersection of the tangents to the elastic and post-yield behavior (as indicated in Figure 5.5). This approximation results in very similar estimates of the yield capacity to the equal energy method, which is explained further in Chapter 6. The maximum capacity is defined by the incipient of collapse of the tower, which is the point of nonconvergence in the numerical model. Mean values of the structural material properties and geometric variables, as supplied by Manitoba Hydro, are used for the evaluation of the capacity curves. An uncertainty propagation analysis for the material properties and geometric variables was carried out in Chapter 4 and is not repeated here, as the effects of material uncertainty on tower capacity were found to not vary significantly with wind direction.

5.3.2 Capacity curves for downburst wind profiles

The capacity curves for each downburst scenario are evaluated for 11 wind directions: 0° (transverse direction), 90° (longitudinal direction), and at increments of 10° in between, as well as for wind at 45°. The wind profiles for each downburst scenario are evaluated using the methodology described earlier. The NSP method is used to carry out the analysis for each downburst scenario, and the obtained capacity curves are shown for selected wind directions in Figure 5.6. It is shown that for DB1, which is characterized by the strongest winds over the mid-height of the tower (see Figure 5.3), the yield capacity is the lowest for wind at 45°. Also note that the capacity curve for wind at 45° is lower than for any other wind direction. The yield capacities for wind at 30° and 60° fall between their respective adjacent yield capacities, which is expected due to the expression for wind loading with wind direction (Eq. (5.1) and (5.2)).

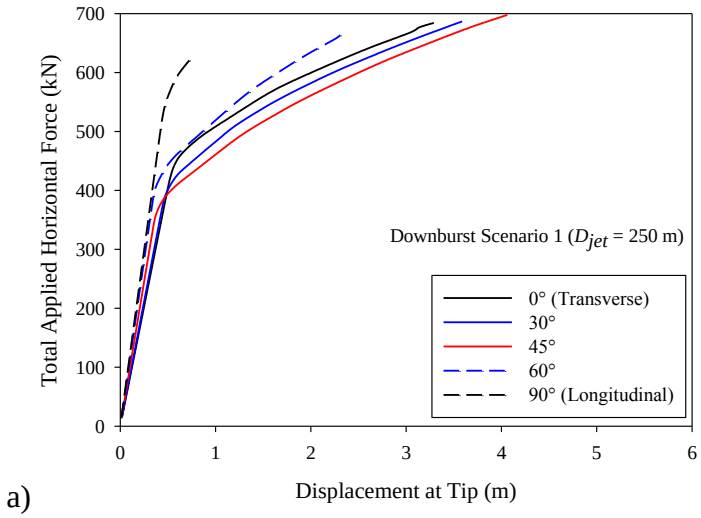

a)

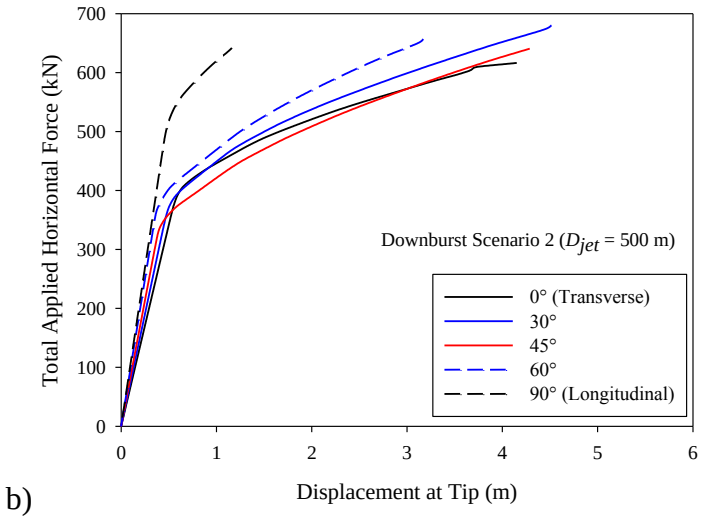

b)

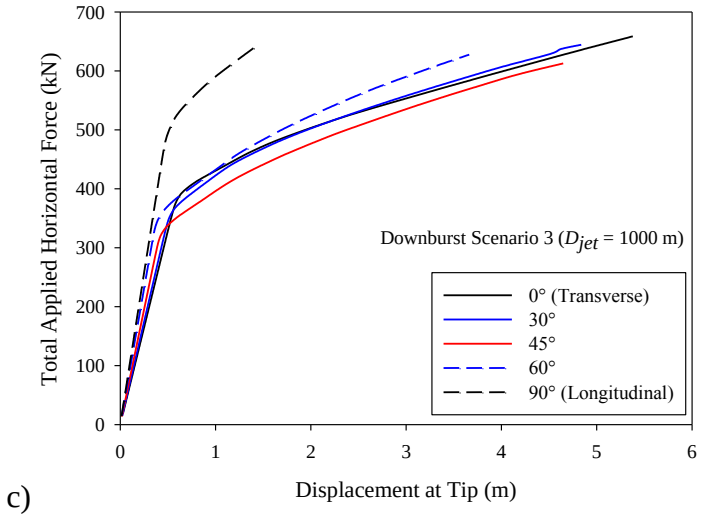

c)

Figure 5.6. Capacity curves for selected wind directions for a) downburst scenario 1, b) downburst scenario 2 and c) downburst scenario 3.

The capacity curves for DB3 are characterized by a lower yield capacity and greater post-yield deformation when compared to those for DB1 and DB2. This is true even for wind at 90°, where there is significantly more post-yield deflection than was observed for DB1. In each case, this is due to the loading distribution of DB1 having lesser impact over the upper portion of the tower. For the transverse direction, the greater wind load at the top of the tower is more important as the wires are in this zone, which results in the relatively large amount of post-yield deflection. The same effect is shown for the longitudinal direction due to the asymmetry of the tower cross-arm, but to a lesser extent as the cross-arm feature does not impact the overall load as much as the wires (note the wires are not loaded for wind at 90°). Similarly to DB1 and DB2, the lowest yield capacity was observed for wind directions in the 45° to 50° range, and the yield capacity to maximum capacity ratio at the other wind directions is approximately the same. That is, the yield and maximum capacities for different wind directions follow similar trends between downburst sizes. The maximum capacity is shown to reduce as downburst size increases for each wind direction, except for wind at 90°, and this is again attributed to the increased loading on the wires with respect to the rest of the tower. The capacity curve for wind at 60° follows that for wind at 90° closely in the elastic range, which implies that the loading on the wires does not have much effect on the elastic behavior of the tower for this set of downburst scenarios. However, once yield is initiated, the loading on the wires plays a more significant role, and the capacity curve at 30° deviates from that for 90° where no load on the wires is present. In all cases, the capacity curves resulting from DB2 fall in between those obtained for DB1 and DB3.

In general, the capacity curves for DB1 are characterized by greater yield and maximum capacities, in addition to less post-yield deformation. This trend is observable for wind at all directions, with the single exception being for 90°, where there is a slightly lower maximum capacity for DB1. It is also shown that there is a greater difference in the capacity curve between wind directions as downburst size increases; this is attributed to the greater loading on the wires which results in a loading distribution concentrate in the upper portion of the tower rather than around mid-height (see wind speed profiles in Figure 5.3). The capacity curves for each respective downburst scenario have a similar shape, with the exception of wind at 90°, which implies that although the yield capacity

varies between wind directions, the tower exhibits similar behavior in the post-yield range for each wind direction.

The yield capacity and tip deflection at yield for each wind direction were estimated from the capacity curves using the method described earlier. The relationship of the yield capacity and tip displacement at yield for each downburst scenario are shown as a function of wind direction in Figure 5.7. It is shown that the capacity curves based resulting from DB1 provide the greatest yield capacities and lowest tip deflections at yield for the downburst configurations, while those for DB3 provide the lowest yield capacities and tip deflections at yield for each wind direction. The values for DB2 fall in between those for DB1 and DB3, which is in agreement with the findings presented in Chapter 4 for the transverse and longitudinal directions.

To further investigate the effect of downburst size, D_{jet}, on the capacity curve, the analysis is carried out D_{jet} from 250 m to 1500 m considering the transverse and longitudinal directions only. The obtained capacity curves are shown in Figure 5.8. It is shown that as the downburst size decreases, the yield capacity of the tower is increased. This can be explained by noting that as the downburst size decreases, the horizontal loads tend to be concentrated at the mid-height of the tower, and the overturning moment is decreased for an equivalent total applied wind load. In other words, for an equal total horizontal wind load, the stress in the structural members is decreased as the downburst size decreases.

In Chapter 6, the capacity curves developed for the selected downburst scenarios are compared to those obtained for ABL and rectangular wind loading. As it will be shown, the capacity curve for the ABL wind profile serves as an approximate lower bound for the capacity curves associated with downburst wind loads. This is expected, as the wind load due to the ABL wind profile is concentrated in the upper portion of the tower. Furthermore, the capacity curve obtained by the rectangular load profile is likely to serve as an approximate upper bound for the capacity curves associated with downburst wind loads. This can be explained by noting that the use of the rectangular load over the height further increases the loading on the lower portion of the tower, at least for $D_{jet} > 500$ m.

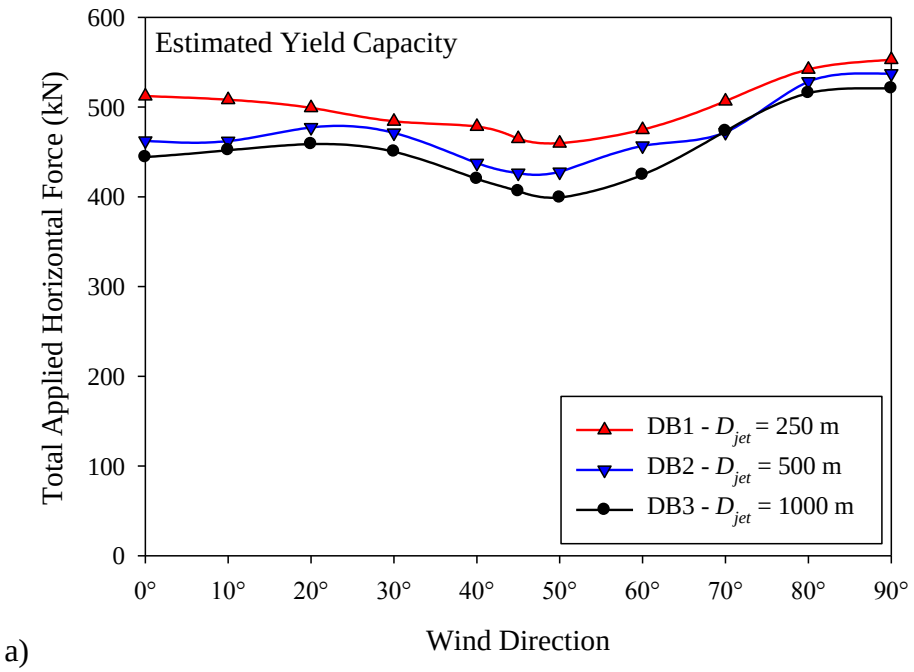

a)

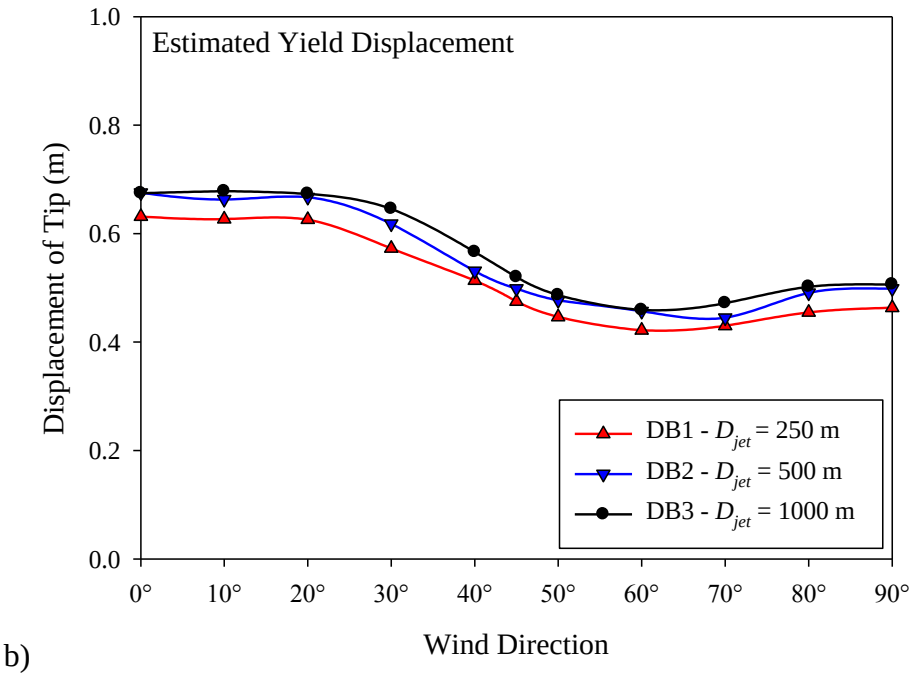

b)

Figure 5.7. Variation with wind direction of a) yield capacity and b) tip displacement.

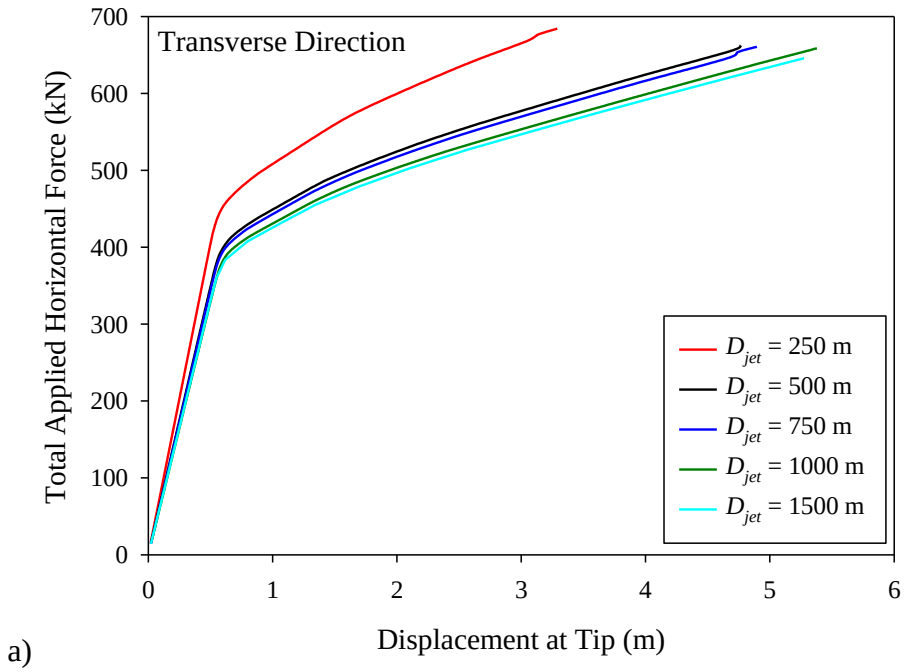

a)

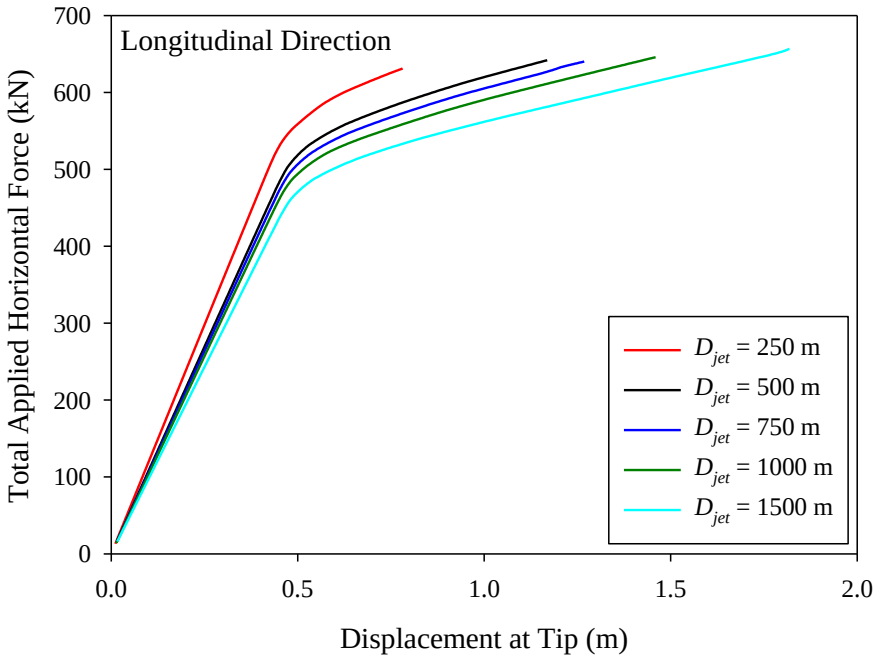

b)

Figure 5.8. Capacity curves for the transverse and longitudinal wind directions showing variation with D_{jet}.

5.4 Conclusions

The capacity curve of a self-supported lattice transmission tower has been obtained for three downburst scenarios at many orientations relative to the tower using the NSP method. The tower is represented as a 3-D numerical model, and both inelastic material and geometric properties are considered in the analysis. The resulting capacity curves are presented as the force-deformation relationship between the total applied horizontal wind load and the displacement of the tip of the tower. The capacity curves are obtained for three downburst sizes and their differences are discussed. The following conclusions are drawn from the study:

1. The capacity curve of the tower is dependent on the shape of the wind profile with which it is loaded. The capacity curves obtained for the downburst scenario characterized by a smaller D_{jet} result in higher yield capacity and less post-yield deformation. The shape of the wind profile has a greater effect on the capacity curve for wind directions where the wires are loaded, which is due to the load concentration in the upper portion of the tower.

2. The shape of the capacity curves for wind directions at which the wires are significantly loaded (i.e., greater than 30°) are quite similar in shape for each downburst scenario. The distribution of applied loads for these directions contributes to a greater amount of post-yield deformation of the tower compared to wind directions where the wires are not loaded.

3. The capacity curves for the tower vary with wind direction, which is primarily due to the asymmetric loading of transmission structures (i.e., different areas in the transverse and longitudinal directions, contribution of wind loading on the wires). For this particular tower design, the lowest yield capacity for each downburst scenario is observed in the 45° to 50° range of wind direction.

4. Multiple downburst sizes (D_{jet}) were investigated for the transverse and longitudinal directions. It is shown that as the downburst size decreases, the horizontal loads tend to

be concentrated at the mid-height of the tower rather than the upper portion. Thus, for an equal horizontal wind load, the stress in the structural members decreases with D_{jet}.

5.5 Acknowledgements

The downburst wind fields were made available by Dr. H.M. Hangan of the WindEEE Research Institute and Department of Civil and Environmental Engineering at the University of Western Ontario. The authors are grateful for many useful discussions with Dr. T.C.E. Ho over the course of this work. The financial support from the National Sciences and Engineering Research Council of Canada (NSERC) is greatly appreciated.

5.6 References

American Society of Civil Engineers (ASCE) (2010). "Guidelines for Electrical Transmission Line Structural Loading (3rd edition)." ASCE Manuals and Reports on Engineering Practice No. 74, Reston, VA, USA.

ANSYS® (2007). ANSYS Multiphysics, Release 9.0. ANSYS Inc., Canonsburg, PA.

Banik, S.S., Hong, H.P. and Kopp, G.A. (2008). "Assessment of tornado hazard for spatially distributed systems in southern Ontario." *J. Wind Eng. Ind. Aerodyn*., 96(8-9), 1376-1389.

Banik, S.S., Hong, H.P. and Kopp, G.A. (2010). "Assessment of capacity curves for transmission line towers under wind loading." *Wind Struct*., 13(1), 1-20.

Canadian Standards Association (CSA) (2010). "Design criteria of overhead transmission lines." CAN/CSA-C22.3 No. 60826-10, CSA, Toronto, Canada.

Darwish, M.M. and El Damatty, A.A. (2011). "Behaviour of self supported transmission line towers under stationary downburst loading." *Wind Struct*., 14(5), 481-498.

Durst, C.S. (1960). "Wind speeds over short periods of time." *Met. Mag*. 89, 181-186.

Fujita, T.T. (1985). "The Downburst: Microburst and Macroburst." SMRP Research Paper No. 210, University of Chicago.

Hangan, H., Roberts, D., Xu, Z. and Kim, J.-D. (2003). "Downburst simulations. Experimental and numerical challenges." *Proc. of the 11th International Conference on Wind Engineering*, Lubbock, TX, USA.

Hangan, H., Savory, E., El Damatty, A., Galsworthy, J. and Miller, C. (2008). "Modeling and prediction of failure of transmission lines due to high intensity winds." *Proc. of the 2008 Structures Congress (ASCE)*, Vancouver, BC, Canada.

Kim, J. and Hangan, H. (2007). "Numerical simulation of impinging jets with application to downbursts." *J. Wind Eng. Ind. Aerodyn.*,, 95(4), 279-298.

Krawinkler, H. and Seneviratna, G.D.P.K. (1998). "Pros and cons of a pushover analysis of seismic performance evaluation." *Eng. Struct.*, 20(4-6), 452-464.

Lee, P.-S. and McClure, G. (2007). "Elastoplastic large deformation analysis of a lattice steel tower structure and comparison with full-scale tests." *J. Constr. Steel Res.*, 63(5), 709-717.

Lin, W.E., Savory, E., McIntyre, R.P., Vandelaar, C.S. and King, J.P.C. (2012). "The response of an overhead electrical power transmission line to two types of wind forcing." *J. Wind Eng. Ind. Aerodyn.*, 100(1), 58-69.

Mara, T.G., Galsworthy, J.K. and Savory, E. (2010). "Assessment of vertical wind loads on lattice framework with application to thunderstorm winds." *Wind Struct.*, 13(4), 413-431.

McCarthy, P. and Melsness, M. (1996). "Severe Weather Elements Associated with September 5, 1996 Hydro Tower Failures Near Grosse Isle, Manitoba, Canada." Environment Canada, Winnipeg, Canada.

Orwig, K.D. and Schroeder, J.L. (2007). "Near-surface wind characteristics of extreme thunderstorm outflows." *J. Wind Eng. Ind. Aerodyn.*,, 95(7), 565-584.

Shehata, A.Y. and El Damatty, A.A. (2008). "Failure analysis of a transmission tower during a microburst." *Wind Struct.*, 11(3), 193-208.

Chapter 6

6 Effect of wind direction on the response and capacity surface of a transmission tower

Electrical transmission towers play a vital role in power transmission networks throughout the world and are often subject to strong wind loads. This chapter investigates the inelastic response of a self-supported lattice transmission tower under different wind events, including traditional atmospheric boundary layer (ABL) wind and downburst wind, and for wind loading at different directions relative to the tower. The nonlinear static pushover (NSP) method is used to obtain the capacity curve of the tower, defined by the force-deformation relation, at each considered wind direction. The results show that the yield and maximum capacities of the tower vary with wind direction. The deformation trajectory is projected on the horizontal plan for each wind direction, illustrating the out-of-plane loading deformation. Since the trajectories are sufficiently smooth and do not overlap for closely spaced wind directions (i.e., 10°), it is suggested that the capacity curves obtained for different wind directions can be used to develop the capacity surface of the tower. Moreover, the results indicate that the capacity for ABL and rectangular (uniform) winds could provide an approximate envelope for the capacity under different sizes of downburst events. These findings could assist in the evaluation of the adequacy of existing towers under downburst events, as well as in the design of new towers.

6.1 Introduction

Overhead electrical transmission systems are critical infrastructure for electrical power transmission and used throughout the world. The primary environmental load considered in the design of transmission structures is the wind load, although the ice load may govern design for cold regions. The scope of this chapter is limited to wind loads. Requirements for wind loads are specified in the design codes CAN/CSA C22.3 No. 60826-10 (herein referred to as CSA-2010) (CAN/CSA 2010) and ANSI National Electric Safety Code (NESC) (ANSI 2006), as well as recommended in ASCE Manual No. 74: Guidelines for Electrical Transmission Line Structural Loading (ASCE 2010).

CSA-2010 adopts the International Electrotechnical Commission (IEC) Standard 60826:2003 (IEC 2003) for design criteria of overhead transmission lines. These codes and guidelines assume a linear elastic response under wind loading and do not discuss the inelastic behavior of transmission towers. As a result, nonlinear inelastic analysis of towers is not frequently carried out in design practice, but becomes necessary for the assessment of ultimate behavior and the estimation of reliability of the tower under wind load.

The nonlinear inelastic force-deformation relation of a tower (described using a capacity curve) for this work is obtained using the nonlinear static pushover (NSP) method, which has most commonly been used for the evaluation of the nonlinear inelastic response of structures to earthquake-induced ground motion (Krawinkler and Seneviratna 1998). It has also been used for steel lattice towers considering point loading representative of full-scale pushover test conditions (Lee and McClure 2007), wind loading for transmission towers (Banik et al. 2010) and woodframe structures (Lee and Rosowsky 2006), and roof panel uplift under wind load (He and Hong 2012). The capacity curve obtained from the NSP method can be used to identify the yield capacity and maximum capacity (i.e., capacity at the incipient of collapse) of a structure. Lee and McClure (2007) provide a comparison of a nonlinear finite element model to full-scale pushover data, which shows good agreement in the estimation of the maximum capacity of the tower. Banik et al. (2010) found that the capacity curve, as defined by the total applied horizontal wind load (which is equivalent to the base shear if the inertia force is negligible) versus the displacement of the tip of the tower, can be adequately estimated using the NSP method, and that the capacity curve obtained through the NSP method provides a good approximation of that obtained from nonlinear incremental dynamic analysis. A comparison of the NSP method to the incremental dynamic analysis method for a 3-D model of this particular transmission tower was carried out in Chapter 3.

There are many instances of transmission tower failure under both extreme synoptic and convective wind events. Synoptic wind refers to wind generated by large-scale pressure differences in the atmosphere, and is characterized by a traditional atmospheric boundary layer (ABL) mean speed and turbulence intensity profile (e.g., Harris and Deaves 1980).

Convective events refer to meso- or micro-scale disturbances, including thunderstorm gust fronts and downbursts, and are characterized by different wind profiles than ABL winds (e.g., Orwig and Schroeder 2007). Furthermore, transmission structures are sensitive to the direction of wind loading due to the contributions of the wind load on the wires, as well as asymmetries in tower geometry. Depending on the tower height and wire span length, the wind loading on the wires may be in the same order as the wind load on the tower itself. The evaluation of wind loads on a tower is often carried out using the geometric characteristics of the tower in the transverse direction (wind perpendicular to the wires) and the longitudinal direction (wind parallel to the wires). It was shown in Chapter 4 that by considering the horizontal wind acting in the transverse or longitudinal direction, the capacity curves obtained based on a rectangular and ABL wind profile provide approximate upper and lower bounds of the capacity curve for a transmission tower under downburst wind loading. However, the applicability of the observations and the behavior of the capacity curve under oblique wind directions are unknown.

This chapter investigates the inelastic response of a self-supported lattice transmission tower under different wind events, including traditional ABL winds and downburst winds, for many directions relative to the tower. Wind at directions in between the transverse and longitudinal directions are referred to as oblique wind directions. The capacity surface of a transmission tower under wind loading is developed based on a series of capacity curves obtained for oblique wind directions. For the analysis, a 3-D numerical model of a self-supported high voltage direct current (HVDC) tower supplied by Manitoba Hydro is modeled in ANSYS® (ANSYS 2007). Two profiles are considered for the wind loading: a rectangular profile, which is uniform with height; and a traditional ABL profile based on open country terrain. The analysis considers 11 wind directions: the transverse direction (wind at 0°); the longitudinal direction (wind at 90°); and wind at oblique directions at increments of 10° in between the transverse and longitudinal directions, as well as wind at 45°. The nonlinear behavior of the tower is modeled by considering both nonlinear geometric variables and nonlinear material properties. More specifically, the structural members are considered to have elastic-perfect-plastic behavior. Capacity curves are obtained for the tower at each of the wind

loading directions and are used to develop the capacity surface of the tower. The results are compared to the wind loads specified in CSA-2010. The differences between the capacity curves obtained for the ABL wind profile, rectangular wind profile and downburst wind loading are discussed.

6.2 Modeling of the transmission tower and wind loads

6.2.1 Numerical model of transmission tower

A self-supported lattice transmission tower design was provided by Manitoba Hydro and modeled in ANSYS® Multiphysics 9.0 (ANSYS 2007). An isometric view of the numerical tower model is shown in Figure 6.1. The tower members are modelled using 2-node nonlinear 3-D frame elements, accounting for bilinear elasto-plastic behaviour, and assuming rigid connections for the multi-bolted moment resisting connections between the tower elements. The self-weight of the tower is included, and the self-weight of the wires are applied as lumped masses at the nodes corresponding to the physical connections. The geometric nonlinearity (i.e., buckling effects) is accounted for through a large deformation analysis. The section and material properties of the tower and wires, as well as the mean structural steel dimensions and distribution by panel, are shown in Table 6.1. A total of 959 frame elements and 405 nodes comprise the numerical model. A modal analysis was carried out on the tower model, which showed that the first and second modes of vibration correspond to the transverse direction at a frequency of 1.167 Hz and the longitudinal direction at a frequency of 1.232 Hz. The third mode of vibration is torsion, having a frequency of 1.556 Hz.

a)

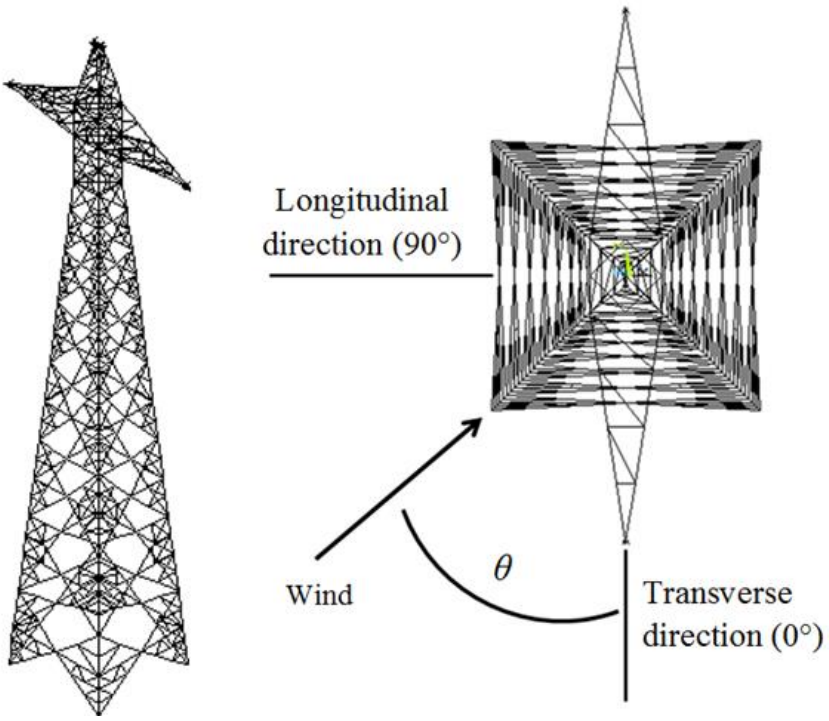

b)

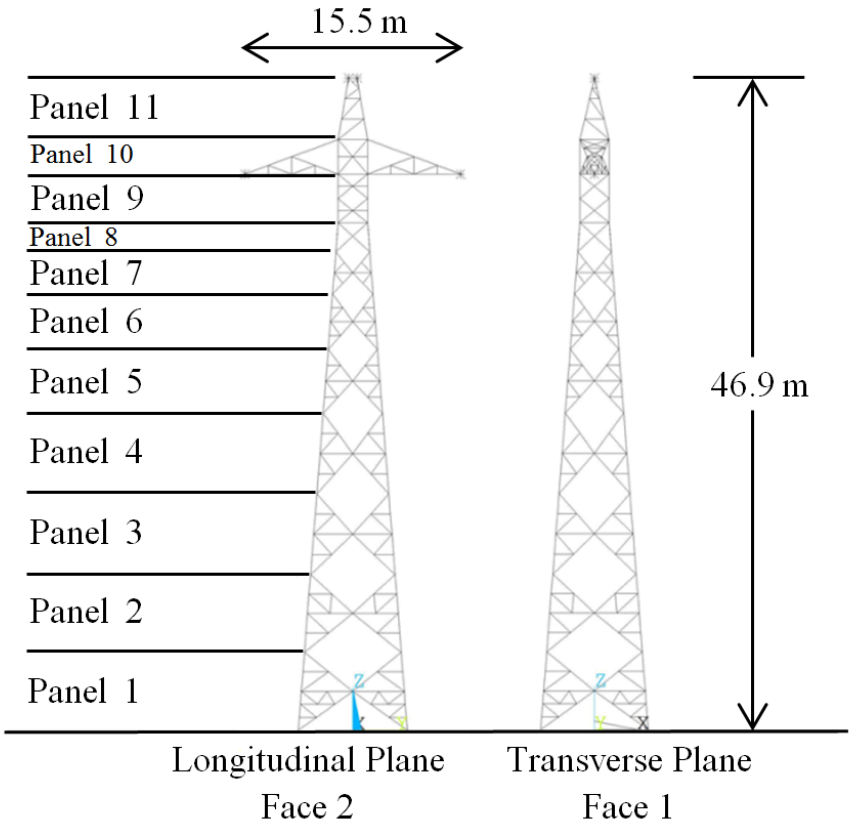

Figure 6.1. Details of transmission tower: a) Isometric and plan views, and; b) definition of loading panels for code-based design.

Table 6.1. a) Nominal section properties of the structural steel member of the tower and wires, b) structural steel distribution by panel and c) nominal section properties of the conductors.

a)

	SI Units (m)		Customary Units (in)		
	Angle	Thickness	Angle	Thickness	Member Key
Chords and Horizontals	0.0445 x .0445	0.125	(1 3/4)" x (1 3/4)"	(1/8)"	a
	0.0445 x .0445	0.375	(1 3/4)" x (1 3/4)"	(3/8)"	b
	0.0508 x 0.0508	0.125	2" x 2"	(1/8)"	c
	0.0508 x 0.0508	0.1875	2" x 2"	(3/16)"	d
	0.0635 x 0.0635	0.1875	(2 1/2)" x (2 1/2)"	(3/16)"	e
	0.0762 x 0.0762	0.1875	3" x 3"	(3/16)"	f
Diagonals and Legs	0.0762 x 0.0762	0.125	3" x 3"	(1/4)"	D1
	0.0889 x 0.0635	0.125	(3 1/2)" x (2 1/2)"	(1/4)"	D2
	0.0889 x 0.0889	0.125	(3 1/2)" x (3 1/2)"	(1/4)"	D3
	0.1016 x 0.1016	0.1875	4" x 4"	(3/16)"	D4
	0.127 x 0.127	0.3125	5" x 5"	(5/16)"	L1
	0.127 x 0.127	0.375	5" x 5"	(3/8)"	L2

b)

	Members in Resisting Direction		Support
Panel	Longitudinal	Transverse	Plan
1	L2, D2, a, c, d	L2, D1, a, c, d	
2	L2, D2, a, b, d	L2, D2, a, b, d	
3	L2, D3, c, e	L2, D2, c, e	
4	L2, D3, a, e	L2, D2, a, e	
5	L1, D3, a, d	L1, D2, a, d	
6	L1, D3, a, b	L1, D2, a, b	
7	L1, D3, a, c	L1, D3, a, c	
8	L1, D4, d	L1, D3, d	
9	D3	D3, a	a
10	D3, e	D3, D4, a, d, f	L1, D1, a, b, d, e
11	a, e	D1, a, b, c	

c)

Property	Conductor	Ground wire
Diameter (m)	0.0381	0.0184
Density (kg/m)	2.354	1.046
Modulus of Elasticity (GPa)	58.6	125.3
Design Span (m)	488	488

6.2.2 Wind loads specified in CSA-2010

Wind loads for the overhead transmission towers are specified in CAN/CSA C22.3 No. 60826-10, which adopts the criteria recommended in the IEC Standard 60826:2003 for design of overhead transmission lines (IEC 2003). CSA-2010 also contains climatic information (i.e., wind speed, ice thickness) for Canadian locations. In compliance with the CSA-2010 procedure, the tower was divided into 11 representative sections, referred to as panels, as shown in Figure 6.1. The wind load on each of the panels are calculated as

$$A_t = 0.5\tau\mu V_R^2 G_t \left(1 + 0.2\sin^2(2\theta)\right) \left(S_{t1}C_{xt1}\cos^2\theta + S_{t2}C_{xt2}\sin^2\theta\right) \quad (6.1)$$

where A_t (N) is the total wind loading on the panel in the direction of the wind; τ is an air density correction factor taken to be 1; μ is the density of air taken to be 1.225 kg/m^3; V_R (m/s) is the reference wind speed based on a 10-minute averaging period at 10 m height in open country terrain; θ is the angle of attack (yaw angle) illustrated in Figure 6.1; S_{ti} (m^2) is the total surface area projected normally on the corresponding i-th face, i = 1 and 2 (see Figure 6.1); C_{xti} is the drag coefficient for the corresponding i-th face; and G_t is a combined wind factor accounting for roughness of terrain and height of the panel. In this case, faces 1 and 2 correspond to the transverse and longitudinal faces of the tower, respectively. The wind loading on the conductor and ground wire lines are calculated such that

$$A_c = 0.5\tau\mu V_R^2 G_c G_L d L C_{xc}\sin^2\Omega \quad (6.2)$$

where A_c (N) is the total load on the line; C_{xc} is the drag coefficient of the line taken to be 1.0; G_c is the combined wind factor for the line; G_L is the span factor based on the length of the span; d (m) is the diameter of the line; L (m) is the wind span of the wires; and Ω is the angle of attack (yaw angle) between the wind direction and the wires. If there is no line angle between consecutive towers (i.e., consecutive towers are parallel), Ω equals (90-θ)°.

As can be seen in Eq. (6.1) and (6.2), the wind loading in the longitudinal direction is based on the loading of the tower alone, while the wind loading in the transverse direction contains significant contributions from the wires. The geometric and aerodynamic parameters (as recommended in CSA-2010) for each panel, as well as the conductors and ground wire, are listed in Table 6.2. An open country exposure was considered in the calculation of G_t, G_c, and G_L, which corresponds to a power law exponent, α, of approximately 0.16. The resultant wind loads are shown for the 11 directions considered (0° through 90° at increments of 10°, as well as the 45° case) in Table 6.3 in terms of V_R^2. The wind loads in the transverse and longitudinal directions, as well as the resultant load, are plotted in Figure 6.2. The greatest resultant wind load on the tower alone occurs for a wind direction of 50°, while the greatest total load on the tower and wires occurs for a wind direction of 0°. The latter is referred to as the fully transverse wind direction.

6.2.3 Application of wind loads to the tower model

The NSP method is based on the total load being proportional to the loading profiles, and that the loading profile is time invariant. In the case of wind, the horizontal wind load profile is proportional to the square of the wind speed profile. The first wind speed profile used for the numerical analysis represents a traditional mean ABL wind profile in open country terrain, based on a power law exponent, α, of 0.16. It is assumed that the wind speed is spatially fully correlated, or coherent, and that the adopted power law leads to a 3-second gust wind speed at height z (m) above ground, $V_{3s}(z)$, defined by

$$V_{3s}(z) = (z/10)^{0.16} V_{3s,10m} \tag{6.3}$$

where $V_{3s,10m}$ represents the 3-second gust wind speed at a height of 10 m. The second wind profile is rectangular in shape, and represents a uniform wind profile along the height of the tower (i.e., $V_{3s}(z) = V_{3s,10m}$ over the height of the tower). The latter profile is selected as it has been shown in Chapter 4 that the associated capacity curve provides an approximate upper bound to the capacity curves assessed for downburst wind profiles in the cases of the transverse and longitudinal wind directions.

Table 6.2. Tabulation of values for use of CSA-2010 for the transmission tower.

		Transverse (Face 1)		Longitudinal (Face 2)		
Panel	Height (m)	S_{xt1} (m^2)	C_{xt1}	S_{xt2} (m^2)	C_{xt2}	G_t
1	2.8	4.51	3.39	4.51	3.39	1.76
2	8.5	3.88	3.42	3.88	3.42	1.90
3	14.3	3.74	3.36	3.74	3.36	2.03
4	20.1	3.46	3.29	3.46	3.29	2.15
5	25.3	2.75	3.16	2.75	3.16	2.25
6	29.6	2.27	3.05	2.27	3.05	2.32
7	33.1	1.76	2.85	1.76	2.85	2.37
8	35.65	1.1	2.8	1.1	2.8	2.40
9	38.45	1.52	2.91	1.7	2.8	2.44
10	41.45	0.89	3.08	4.73	2.89	2.47
11	44.9	1.17	2.71	1.17	2.71	2.51
	Height (m)	C_{xc}	G_c	G_L	d (m)	L (m)
Conductor	35.65	1.0	2.31	0.919	0.076	488
Ground wire	44.9	1.0	2.40	0.919	0.0184	488

Note: There are 2 conductors, and 1 ground wire in the assembly.

The wind loads are applied to the numerical model at each connection height, represented as nodes in the model. This results in the application of wind loading to nodes at 45 heights along the model (there are multiple nodes at every height), which accounts for intra-panel variation in wind speed. Note that the approach in CSA-2010 applies a constant wind pressure over the entirety of each panel, and thus does not account for intra-panel variation in wind speed. The geometric and aerodynamic parameters used to calculate the wind forces correspond to those shown in Table 6.2; accordingly 11 unique sets of geometric and aerodynamic parameters are represented in the calculated wind loads. This approximation is valid, as the geometric and aerodynamic parameters do not change significantly over the height extent of each panel.

Table 6.3. Calculated wind loads using CSA-2010 for oblique wind directions.

	Wind Direction (θ)										
Panel	0°	10°	20°	30°	40°	45°	50°	60°	70°	80°	90°
1	16.5	16.9	17.8	19.0	19.7	19.8	19.7	19.0	17.8	16.9	16.5
2	15.4	15.8	16.7	17.8	18.4	18.5	18.4	17.8	16.7	15.8	15.4
3	15.6	16.0	16.9	18.0	18.7	18.7	18.7	18.0	16.9	16.0	15.6
4	15.0	15.3	16.2	17.2	17.9	18.0	17.9	17.2	16.2	15.3	15.0
5	12.0	12.3	13.0	13.8	14.3	14.4	14.3	13.8	13.0	12.3	12.0
6	9.8	10.1	10.7	11.3	11.7	11.8	11.7	11.3	10.7	10.1	9.8
7	7.3	7.5	7.9	8.4	8.7	8.7	8.7	8.4	7.9	7.5	7.3
8	4.5	4.6	4.9	5.2	5.4	5.4	5.4	5.2	4.9	4.6	4.5
9	6.6	6.8	7.2	7.7	8.1	8.2	8.2	8.0	7.6	7.3	7.1
10	4.1	4.8	6.6	9.5	13.1	14.9	16.5	19.0	20.3	20.7	20.7
11	4.9	5.0	5.3	5.6	5.8	5.8	5.8	5.6	5.3	5.0	4.9
Conductor	96.4	93.5	85.2	72.3	56.6	48.2	39.9	24.1	11.3	2.9	0.0
Ground wire	12.1	11.8	10.7	9.1	7.1	6.1	5.0	3.0	1.4	0.4	0.0
Total - Tower	111.8	114.9	123.2	133.5	141.9	144.4	145.4	143.3	137.3	131.3	128.8
Total - Wires	108.6	105.3	95.9	81.4	63.7	54.3	44.9	27.1	12.7	3.3	0.0
Total - Tower and wires	220.4	220.2	219.1	214.9	205.6	198.7	190.3	170.4	150.0	134.6	128.8

Note: All values shown $*V_R^2$

Table 6.4. Loads and critical wind speeds for ABL and rectangular wind profiles.

	Wind Load (N)		Critical Speed for Yield (km/h)		Critical Speed for Collapse (km/h)	
Wind Direction	$*(V^2_{3sec,10m})$	$*(V^2_{10min,10m})$	$V_{3sec,10m}$	$V_{10min,10m}$	$V_{3sec,10m}$	$V_{10min,10m}$
ABL Wind Profile						
0°	140.2	286.8	200	140	242	169
10°	139.6	285.4	202	141	238	166
20°	137.3	280.7	202	141	248	174
30°	132.5	270.9	202	141	249	174
40°	124.4	254.3	203	142	252	176
45°	118.9	243.2	203	142	255	178
50°	112.8	230.6	206	144	258	180
60°	98.8	202.1	227	159	282	197
70°	85.2	174.2	261	182	316	221
80°	75.1	153.5	297	207	342	239
90°	71.3	145.8	307	215	348	243
Rectangular Wind Profile						
0°	102.9	210.4	246	172	294	205
10°	102.8	210.2	247	173	296	207
20°	102.1	208.8	248	173	297	208
30°	99.9	204.4	247	173	304	212
40°	95.4	194.9	245	171	304	213
45°	91.9	188.1	246	172	307	215
50°	87.9	179.8	251	176	313	219
60°	78.5	160.4	272	190	333	233
70°	68.8	140.7	305	214	351	246
80°	61.6	125.9	343	240	368	257
90°	58.9	120.4	351	246	374	262

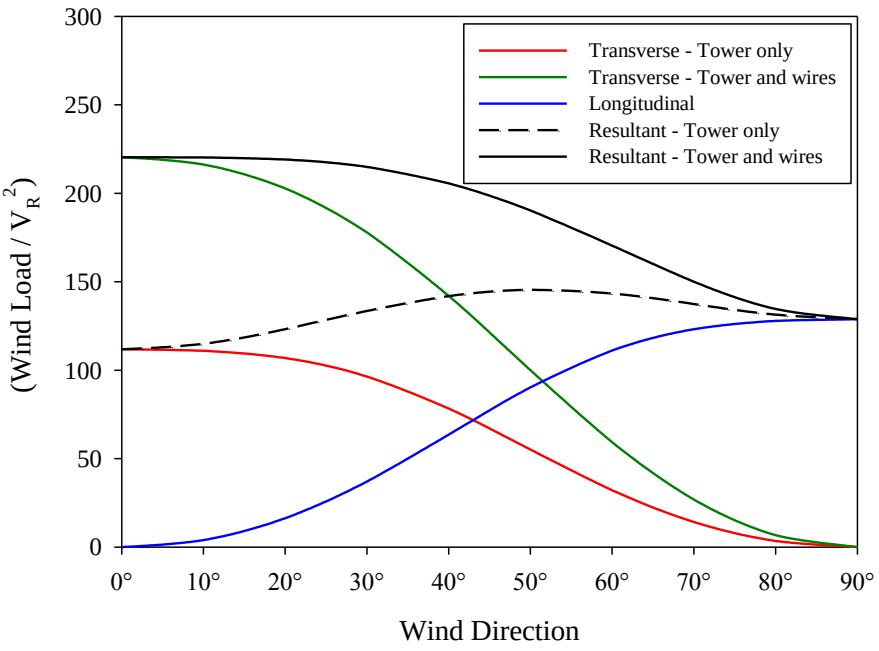

Figure 6.2. Transverse, longitudinal and resultant wind loads for the transmission tower as calculated with CSA-2010.

The wind forces on the wires (2 conductors, 1 ground wire) are based on half the wind span of the wires on each side of the tower, which corresponds to a loading span of 488 m (2 x 244 m). The resulting wind forces are applied to the tower as point loads at each of the nodes corresponding to the wire-structure connections. The total wind loads at each node were calculated using Eq. (6.1) and (6.2) for the tower structure and wires, respectively, without the contributions of the combined gust factors G_t and G_c, or the span factor G_L. This approach was taken as the variation of the wind speed over height is considered by using the wind speed profile for $V_{3s}(z)$, and it was assumed that the wind profile is coherent over the height of the structure.

The wind load in CSA-2010 is based on a 10-minute mean wind speed at 10 m height in open country terrain, and for a specified return period of 50 years; this corresponds to the wind speed V_R. Therefore, a conversion of the analytical results is required in order for a direct comparison to be made to the values calculated using the code. For this conversion, the ratio ($V_{3s,10m}$ / $V_{10min,10m}$) = 1.43 for open country terrain (Durst 1960) is used, where $V_{10min,10m}$ is used to denote the 10-minute mean wind speed at 10 m height,

but without referring to a specific return period. The wind loads resulting from the numerical analysis are shown in Table 6.4 in terms of both $V^2_{3s,10m}$ and $V^2_{10min,10m}$. Comparison of these values to those shown in Table 6.3 (as calculated by CSA-2010) indicate that the use of the described wind load application procedure leads to 23% and 11% greater wind loads in the transverse and longitudinal directions, respectively. The differences are attributed to the use of a fully coherent mean ABL wind profile in the NSP method, and a more detailed description of the wind speed variation over the height compared to the CSA-2010 approach. In all cases the numerical procedure and wind speed profile considered result in a more conservative estimate of the wind load.

6.3 Capacity curves and surfaces for the tower under ABL and rectangular wind profiles

6.3.1 Effect of wind direction on the capacity curve

The NSP method is often applied to evaluate the performance and capacity of structures under seismic loading (Krawinkler and Seneviratna 1998). More recently, it has been applied to wind loading on a 2-D transmission tower (Banik et al. 2010), which showed that the obtained capacity curves represent the peak wind load effects on a structure. Thus, they could be viewed as representative of the response to short-duration gust wind speeds, for example, 3-second gusts. The procedure is used to evaluate the force-deformation relation, and to identify the yield and maximum capacities of the tower. A capacity curve showing the behavior of a nonlinear inelastic system approximated by a bilinear system is illustrated in Figure 6.3. Through the NSP method, the applied forces are monotonically increased while a constant loading profile is maintained. In this particular case, the applied forces reflect the total applied horizontal wind load with the loading profile corresponding to the wind speed profiles described earlier. The results are plotted as capacity curves, which describe the relationship of the resultant applied wind load (which is equivalent to the resultant base shear if the inertia force is negligible) to the resultant displacement of the tip of the tower. The capacity curves are approximated as a bilinear system for the estimation of the yield capacity, which is defined by the equal energy method (i.e., the point of intersection of the elastic stiffness and the post-yield stiffness for which the energy bounded by the mentioned lines and the capacity curves are

equal). In the majority of previous work, the equal energy method is used (e.g., Krawinkler and Seneviratna 1998), although here estimates of the yield capacity were also made considering the tangents of the elastic and post-yield stiffness. Based on a comparison of two methods, it was found that the latter resulted in yield capacity estimates approximately 4% greater than the former, which varies slightly with wind direction. The maximum capacity is defined by the incipient of collapse of the tower, at which the solution to the numerical model does not converge. For the evaluation of the following capacity curves, the mean values of the structural material properties and geometric variables, as provided by Manitoba Hydro, are used.

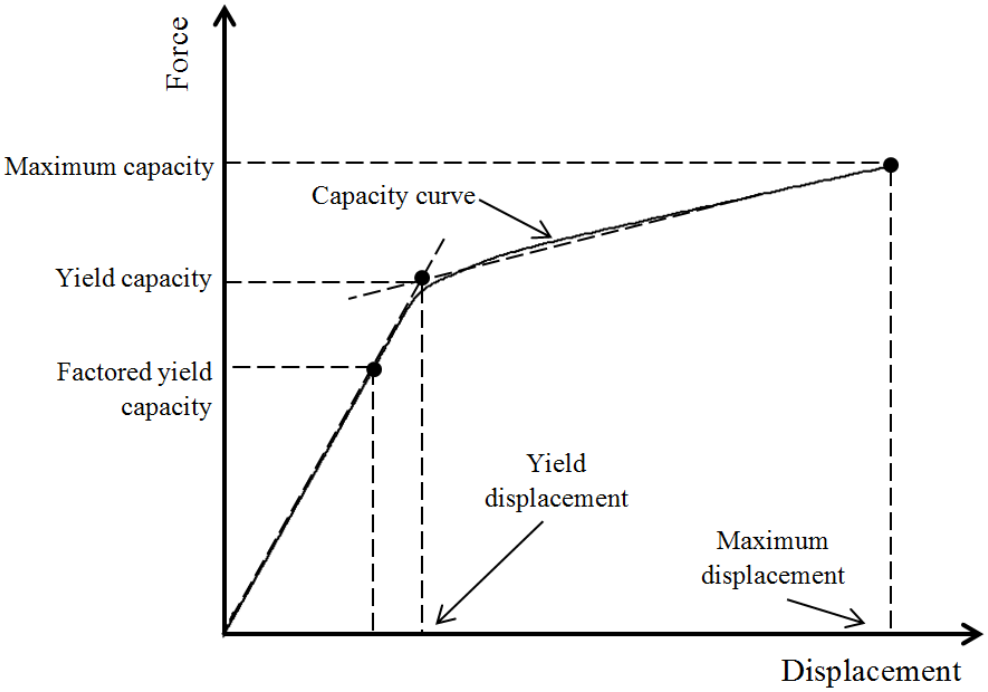

Figure 6.3. Force-deformation (capacity) curve for an inelastic system showing equal energy method.

The NSP method is used to obtain capacity curves for the tower at various wind directions. The analysis is carried out for wind direction θ from 0° through 90° at increments of 10°, as well as for wind at 45°. The resulting capacity curves are shown for the ABL and rectangular wind profiles in Figure 6.4. The yield and maximum capacities identified from the capacity curves and their corresponding wind speeds ($V_{10\text{min},10\text{m},\text{YLD}}$ for yield capacity and $V_{10\text{min},10\text{m},\text{MAX}}$ for the maximum capacity) are listed

a)

b)

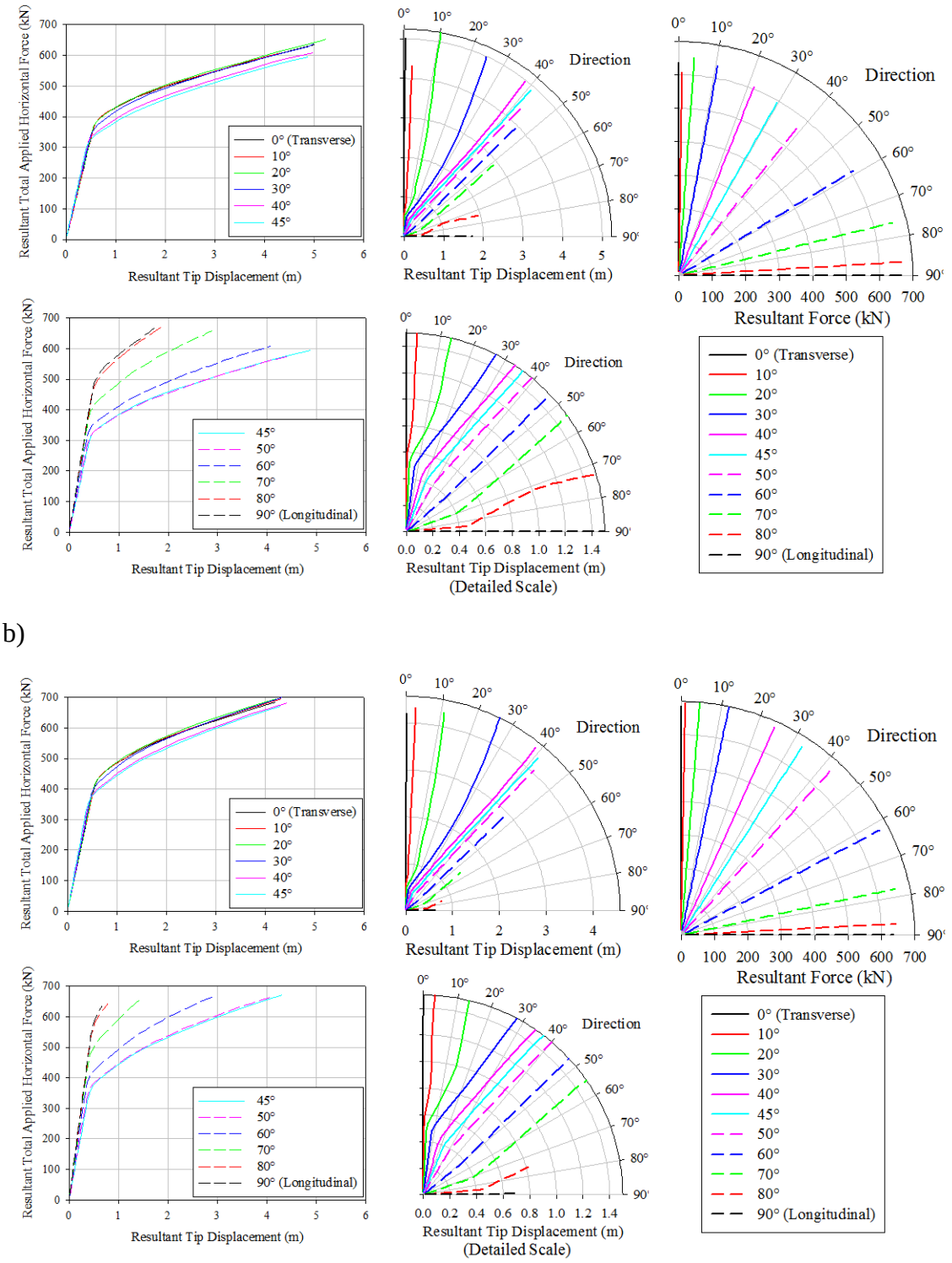

Figure 6.4. Capacity curves and direction of resultant total applied horizontal force and corresponding tip deflection for a) ABL wind profile, and b) rectangular wind profile.

in Table 6.5. The results shown in Table 6.5 indicate that the lowest yield and maximum capacities for the tower occur at a wind direction of 50°, while the highest yield and maximum capacities occur for a wind direction of 90°. There is approximately 28% variation in the yield capacity (370 kN to 517.8 kN) and approximately 13% variation in the maximum capacity (577.5 kN to 666.7 kN) for the ABL wind profile. These values are 24% (427.4 kN to 561 kN) and 10% (636.4 kN to 712 kN) for the rectangular wind profile. However, it is found that although the lowest capacity of the tower is for wind at 50°, the critical wind speed ($V_{10\text{min},10\text{m}}$) initiating yield occurs for the transverse direction (i.e., wind at 0°) and is approximately 140 km/h (38.9 m/s) for the ABL wind profile. This is due to the wind load on the wires being a maximum for wind at 0°. Note that the wind speed at yield for the wind direction within the sector 0° through 50° is within 3% of the critical wind speed. The trends for the maximum capacity for each wind direction are similar to those for the yield capacity, and the critical wind speed ($V_{10\text{min},10\text{m}}$) initiating collapse is approximately 166 km/h (46.1 m/s).

To better understand and explain the above behavior, the resultant direction of the wind force and the resultant tip displacements are projected in the horizontal plane for each considered wind direction in Figure 6.4. It is shown that the direction of the resultant wind force is predominantly transverse (i.e., the resultant wind force is in a direction less than 45°, for which most of the load is resisted in the transverse plane) for wind directions 0° through 50°. This explains the similarity between capacity curves over this azimuth range. For wind at 60°, the resultant wind load on the tower becomes predominantly in the longitudinal direction, which is indicated by the increased yield capacity and lower post-yield deformation at this wind direction. The decrease in post-yield deformation is more significant for the rectangular wind profile. Similar trends are observed for wind directions 70° through 90°, and the resultant wind load and resultant tip displacements are purely in the longitudinal direction for wind at 90°.

It is also worthwhile to note the elastic and post-yield behaviour of the resultant displacements. In the elastic range, the direction of the resultant tip displacement is always less than the direction of the resultant wind load, and much less than the true direction of the wind (with the exception of wind at 70°). This is due to the differences in

Table 6.5. Yield and maximum capacities of the tower under ABL and rectangular wind profiles.

Wind Direction	Direction of Resultant Wind Load	Direction of Resultant Tip Displacement (elastic range)	Yield Capacity (kN)	Maximum Capacity (kN)
ABL Wind Profile				
0°	0.0°	0.0°	430.7	635.2
10°	0.9°	0.7°	439.0	607.6
20°	4.1°	2.8°	432.1	653.3
30°	10.5°	7.3°	416.8	636.1
40°	21.7°	15.5°	393.8	607.5
45°	29.6°	21.5°	379.5	594.7
50°	38.8°	29.1°	370.0	577.5
60°	59.0°	48.9°	392.6	607.0
70°	76.2°	70.0°	447.1	656.9
80°	86.6°	84.9°	509.8	676.5
90°	90.0°	90.0°	517.8	666.7
Rectangular Wind Profile				
0°	0.0°	0.0°	481.2	684.9
10°	3.0°	0.7°	484.5	695.0
20°	12.2°	3.0°	484.4	696.4
30°	27.9°	7.7°	469.7	712.0
40°	47.7°	16.4°	440.9	682.1
45°	57.3°	22.7°	429.5	670.2
50°	65.7°	30.6°	427.4	663.1
60°	78.1°	50.5°	446.9	672.3
70°	85.4°	71.1°	495.6	655.4
80°	88.9°	85.2°	559.8	643.8
90°	90.0°	90.0°	561.0	636.4

loading area between the transverse and longitudinal directions. Once yield is initiated, the resultant tip displacement is marked by a shift in direction; this occurs at a fairly low tip displacement compared to the amount of post-yield deformation that the tower undergoes. It is shown that following yield, the direction of the resultant tip displacement tends towards 45° for each oblique wind direction. However, after significant deformation has occurred in the post-yield range, the resultant tip displacements for wind directions 10° through 30° tend toward the transverse direction. Note that the paths of the resultant tip deflections do not intersect in the elastic or post-yield range.

6.3.2 Capacity surfaces and comparison to the capacity surface under downburst wind load

To define a capacity surface for the tower based on the resultant total applied horizontal wind load, it is desirable that the resultant displacements for each wind direction do not overlap in either the elastic or post-yield range. This condition ensures that the same resultant displacement corresponds to only a single value of total applied horizontal wind load from a particular direction. It is shown in Figure 6.4 that although the direction of the resultant tip displacement does indeed change once yield occurs, the paths of the resultant tip displacement for each considered wind direction between yield and collapse do not intersect. As a result, it was deemed acceptable that the surface formed by a series of capacity curves obtained for each wind direction (as shown in Figure 6.4) represents the capacity surface of the tower.

Based on this consideration and the capacity curves developed in the previous section, 3-D plots defining the capacity surfaces of the tower under ABL and rectangular wind profiles are constructed and shown in Figure 6.5. In Figure 6.5, the horizontal axes represent the tip displacements along the transverse and longitudinal directions, and the vertical axis denotes the total applied horizontal wind load (or base shear). In other words, the horizontal axes describe the resultant tip displacement and the vertical axis describes the resultant applied horizontal wind load. The capacity surface is interpolated from the capacity curves for the considered wind directions in the previous section. The plots indicate that the capacity curves conditioned on the wind direction θ do not intersect each other, which is expected as the resultant displacements for each capacity curve projected in the horizontal plan do not cross (as shown in Figure 6.4). The capacity surfaces shown in Figure 6.5 are smooth, which indicates that they may be interpolated and approximated directly from fewer capacity curves; for example, capacity curves for wind at 0°, 50° and 90°, which simplifies the numerical effort. To investigate the adequacy of this approximation, capacity surfaces are developed based on the capacity curves for wind at these directions and are shown in Figure 6.6. Comparison of the results shown in Figures 6.5 and 6.6 indicate that the differences in terms of the total applied wind forces are in the order of approximately 10%. It is worth noting that the

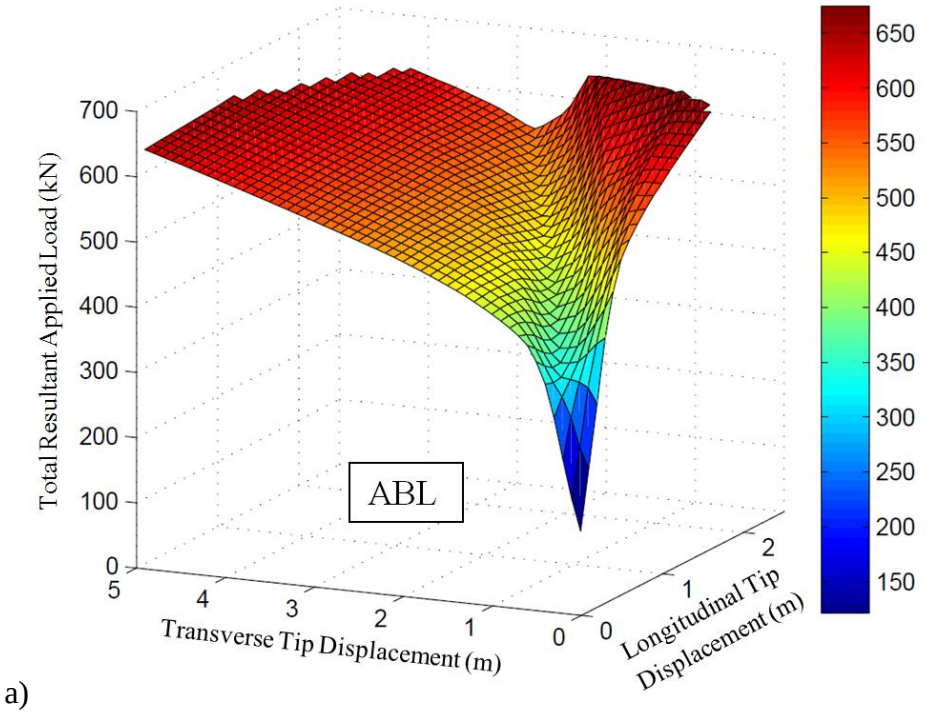

a)

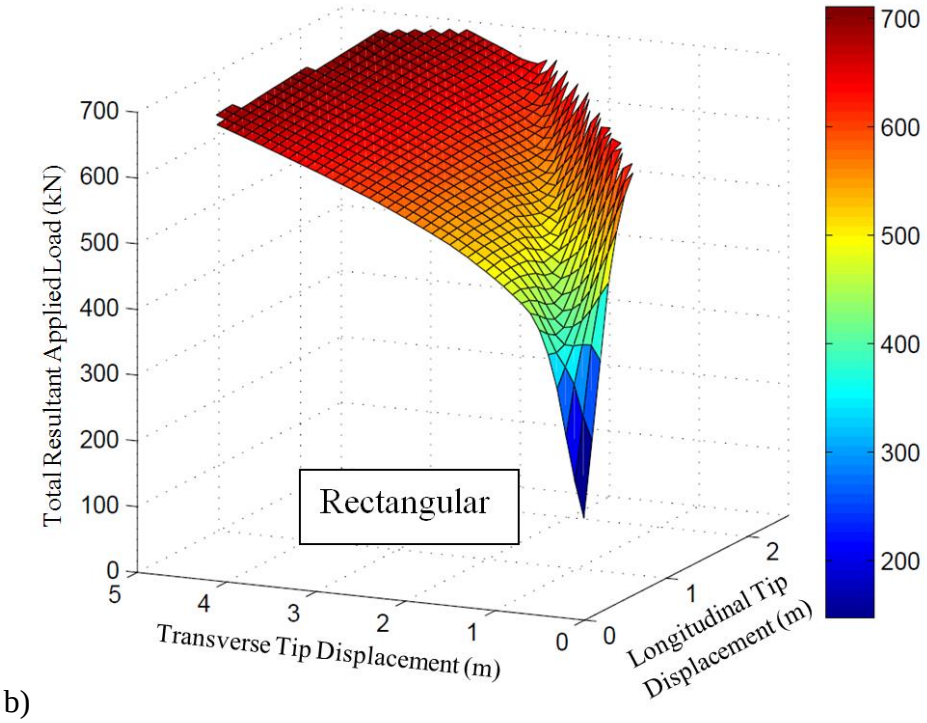

b)

Figure 6.5. 3-D plot of capacity surface of the tower under a) ABL wind profile and b) rectangular wind profile.

interpolation of the subset of curves follows that of the full set of curves for wind directions ranging 0° through 60°, while the former tends to underestimate the capacity over the remainder of wind directions for the ABL wind profile and overestimate the capacity for the rectangular wind profile.

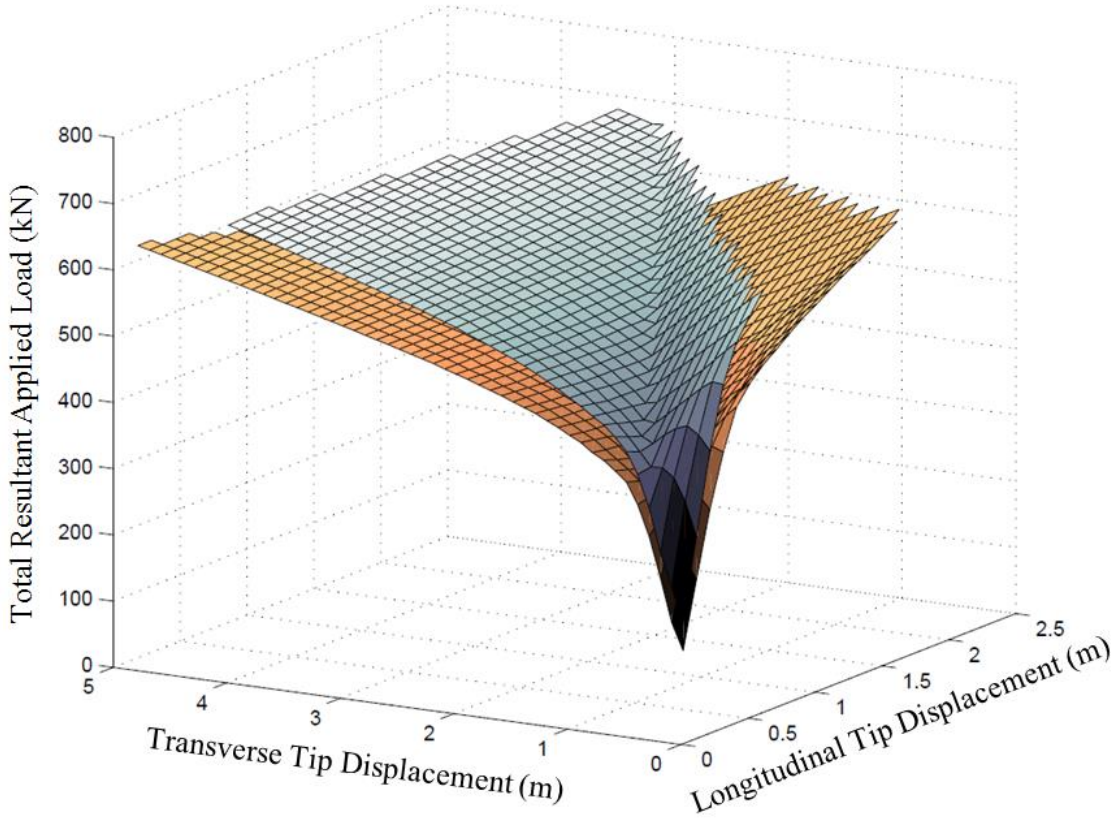

Figure 6.6. 3-D plot of capacity surface of the tower interpolated from capacity curve subset (wind at 0°, 50°, and 90°) under ABL wind profile (lower surface) and rectangular wind profile (upper surface).

The results presented in Figures 6.5 and 6.6 also indicate that the capacity surface for the ABL wind profile does not intersect the capacity surface for the rectangular wind profile. That is, for any given resultant displacement, the total applied wind load identified from the ABL capacity surface is always less than that from the rectangular capacity surface. This is in agreement with the conclusions of Chapter 4 for the transverse and longitudinal wind directions, indicating that the capacity curves obtained for the rectangular and ABL wind profiles form approximate upper and lower bounds of the capacity curve for downburst wind loading, respectively. To see if this trend can be extended to the

capacity surface, the capacity curves obtained for the three downburst scenarios discussed in Chapter 5 are used to develop capacity surfaces for the tower. The calculation procedure is similar to that for the ABL wind profile and is described in detail in Chapter 5; the wind fields for the considered downburst scenarios are those developed by Hangan et al. (2003) and validated in Kim and Hangan (2007). The obtained results are shown as the middle surface (green) in Figure 6.7. The majority of microburst events (downbursts with outflows affecting 4 km or less) are believed to be within this range of jet diameters, which is a key parameter for defining the downburst wind speed profile (Kim and Hangan 2007). It is shown that the surface resulting from each downburst scenario is approximately bound by the rectangular capacity surface on the top and the ABL capacity surface on the bottom.

For very small downburst events (i.e., D_{jet} = 250 m), the resulting capacity surface slightly exceeds (in the order of 1-5% depending on wind direction) that developed using the rectangular wind profile, which is shown in Figure 6.8. Downbursts events characterized by a jet diameter of 250 m are small and localized events, and likely represent a significantly low bound for downburst size. The exceedence is due to the distinct shape of the wind profile for this size and location of downburst, which results in a greater loading of the lower portion of the tower than the upper (see Figure 5.3). While the capacity curves for only three downburst scenarios are presented here, additional capacity surfaces for downburst scenarios were found to yield similar results to that for jet diameters ranging from 500 m to 1000 m. That is, the capacity surface for downburst winds was completely bound by those for the ABL and rectangular wind profiles.

The above results indicate that the capacity surface for the tower under typical downburst wind loading can be approximated by those obtained for the ABL and rectangular wind profiles. This makes the structural analysis for downburst wind load unnecessary if approximate results are needed; it largely simplifies the design checking task for downburst wind loads. More importantly, a conservative approximation of tower capacity is made if the surface for the ABL wind profile is used.

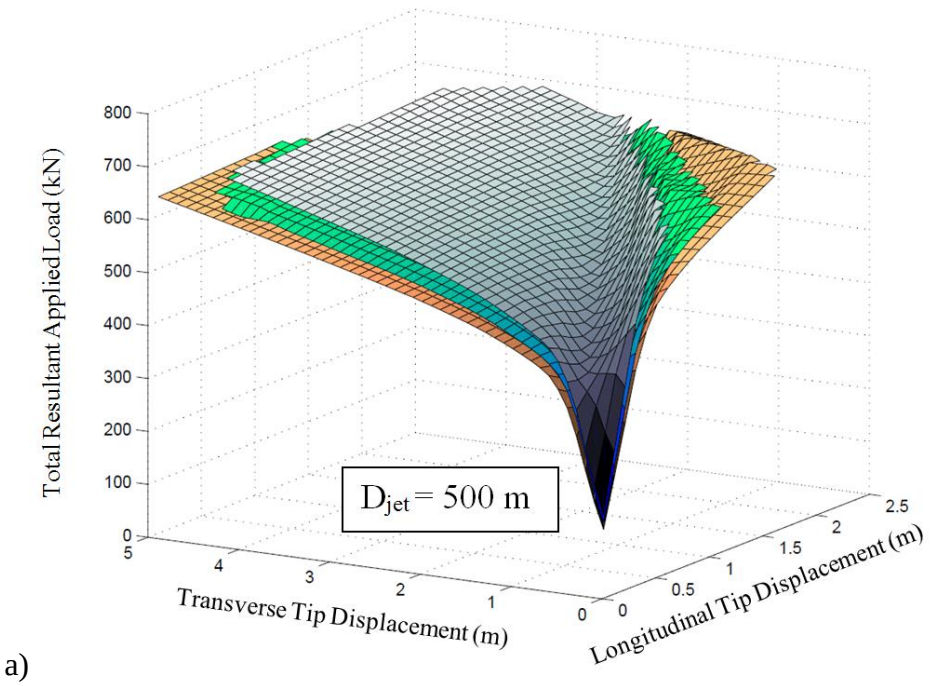

a)

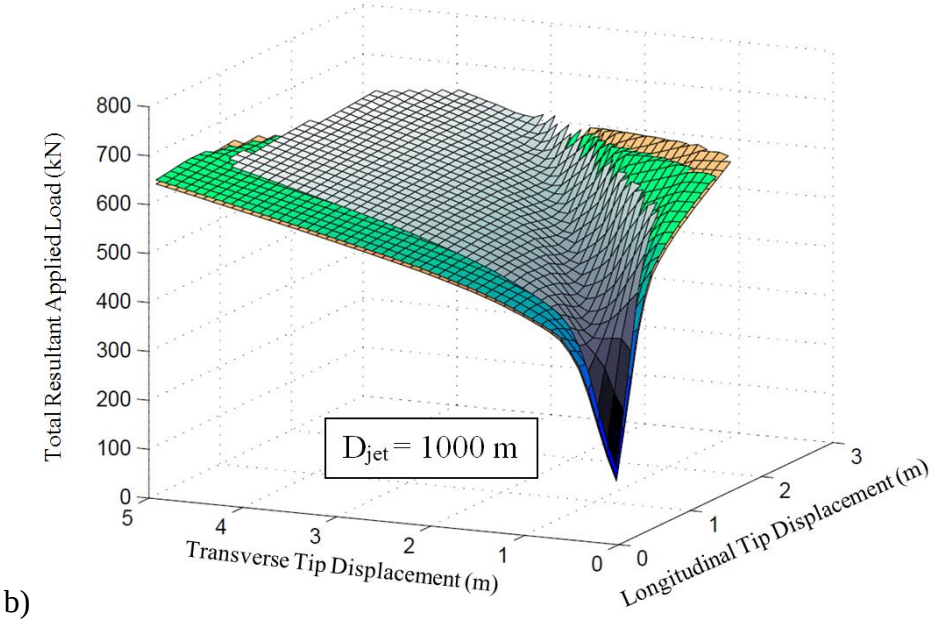

b)

Figure 6.7. 3-D plot of capacity surface for ABL (orange) and rectangular (grey) wind profiles compared with a) downburst with jet diameter of 500 m (green) and b) downburst with jet diameter of 1000 m (green). Capacity surface for ABL wind profile is shown as the lower surface, the downburst capacity surface is shown as the middle surface, and the rectangular capacity surface is shown as the upper surface.

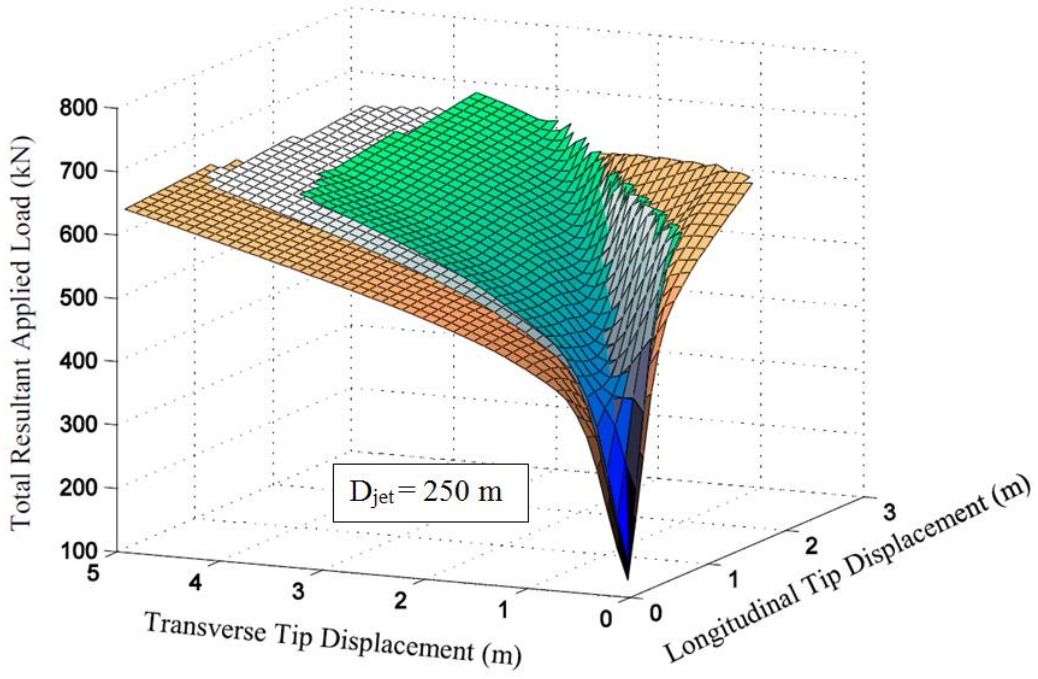

Figure 6.8. 3-D plot of capacity surface for ABL (orange) and rectangular (grey) wind profiles compared with downburst with jet diameter of 250 m (green).

6.4 Conclusions

The NSP method is used to estimate the nonlinear inelastic response of a self-supported transmission tower under traditional ABL winds and rectangular (uniform) winds at various wind directions. The transmission tower and lines are represented by a 3-D numerical model, and wind loads are applied based on the geometric and aerodynamic parameters specified by CSA-2010. Both geometric and material nonlinearity were accounted for in the analysis. The results were used to develop capacity curves for the tower under different wind loading profiles: an ABL wind profile, a rectangular wind profile, and wind profiles resulting from three downburst scenarios. The curves are also used to develop the capacity surface of the tower under wind loading. The following conclusions are drawn from the study:

1. The capacity curve of the tower is dependent on the loading profile applied and wind direction. For any given wind direction, the capacity curves for a scenario downburst are approximately bound by those obtained for the ABL and rectangular wind profiles. The

yield and maximum capacities of the tower for the ABL wind profile are lower than those for the rectangular, or uniform, wind profile. The ratio of yield capacity to maximum capacity for any given wind direction is insensitive to the considered wind profile.

2. The yield capacity of the tower is the lowest for a wind direction of 50° for both the ABL and rectangular wind profiles. However, the critical wind speed initiating yield occurs for the fully transverse wind direction (wind at 0°) for both wind profiles. The wind speed initiating yield for the wind direction within the sector 0° through 50° is within 3% of the critical wind speed.

3. The projection of the resultant tip displacement on the horizontal plan corresponding to the capacity curves for each wind direction do not intersect, and can therefore be used to develop the capacity surface for the tower under wind loading. For a given resultant tip displacement, the total applied wind force for the ABL wind profile is lower than that for the rectangular wind profile; the force for the scenario downburst events is approximately bound by those obtained for the ABL and rectangular wind profiles. This makes the structural analysis for downburst wind load unnecessary if approximate results are desired, and it largely simplifies the task for design checking of new towers and the evaluation of existing towers under downburst wind loads. More importantly, a conservative approximation is made if the capacity curve, or surface, for the ABL wind profile is used.

6.5 Acknowledgements

The first author acknowledges the financial support provided by the National Sciences and Engineering Research Council of Canada (NSERC). Many conversations with Drs. T.C.E. Ho and C.-S. Lee are also greatly appreciated. The authors are grateful to the anonymous reviewers whom provided constructive comments during the review process of the submission of this chapter.

6.6 References

American Society of Civil Engineers (ASCE) (2010). "Guidelines for Electrical Transmission Line Structural Loading (3rd edition)." ASCE Manuals and Reports on Engineering Practice No. 74, Reston, VA, USA.

ANSYS® (2007). ANSYS Multiphysics, Release 9.0. ANSYS Inc., Canonsburg, PA.

Banik, S.S., Hong, H.P. and Kopp, G.A. (2010). "Assessment of capacity curves for transmission line towers under wind loading." *Wind Struct*., 13(1), 1-20.

Canadian Standards Association (CSA) (2010). "Design criteria of overhead transmission lines." CAN/CSA-C22.3 No. 60826-10, CSA, Toronto, Canada.

Durst, C.S. (1960). "Wind speeds over short periods of time." *Met. Mag*., 89, 181-186.

Hangan, H., Roberts, D., Xu, Z. and Kim, J.-D. (2003). "Downburst simulations. Experimental and numerical challenges." *Proc. of the 11th International Conference on Wind Engineering*, Lubbock, TX, USA.

Harris, R.I. and Deaves, D.M. (1980). "The structure of strong winds." Paper 4 of *CIRIA Conference on Wind Engineering in the Eighties*, Construction Ind. Res. and Inf. Assoc., London.

He, W.X. and Hong, H.P. (2012). "Probabilistic characterization of roof panel uplift capacity under wind loading." *Can. J. Civ. Eng*., 39(12), 1285-1296.

International Electrotechnical Commission (IEC) (2003). "Design criteria of overhead transmission lines." CEI/IEC No. 60826:2003.

Kim, J. and Hangan, H. (2007). "Numerical simulation of impinging jets with application to downbursts." *J. Wind Eng. Ind. Aerodyn*., 95(4), 279-298.

Krawinkler, H. and Seneviratna, G.D.P.K. (1998). "Pros and cons of a pushover analysis of seismic performance evaluation." *Eng. Struct*., 20(4-6), 452-464.

Lee, K.H. and Rosowsky, D.V. (2006). "Fragility curves for woodframe structures subjected to lateral wind load." *Wind Struct*., 9(3), 217-230.

Lee, P.-S. and McClure, G. (2007). “Elastoplastic large deformation analysis of a lattice steel tower structure and comparison with full-scale tests.” *J. Constr. Steel Res*., 63(5), 709-717.

Mara, T.G. and Hong, H.P. (2013). “Effect of relative orientation on the capacity of a transmission tower under downburst loading.” *Proc. 3rd Specialty Conference on Disaster Prevention and Mitigation*, CSCE, Montreal, QC.

NESC (2006). National electrical safety code. ANSI C2. IEEE, Piscataway, NJ.

Orwig, K.D. and Schroeder, J.L. (2007). “Near-surface wind characteristics of extreme thunderstorm outflows.” *J. Wind Eng. Ind. Aerodyn*., 95(7), 565-584.

Chapter 7

7 Conclusions and Recommendations

7.1 Summary

The focus of this thesis is on the assessment of the yield and maximum capacity of a prototype self-supported transmission tower under different types of wind loading over a range of wind directions. In order to apply wind loads to the numerical transmission tower model, it was necessary to select an expression which appropriately describes the aerodynamics for all the types of sections present in a transmission tower structure. Wind tunnel test data were analyzed and compared to the expressions provided in multiple wind loading documents, and it was decided to use the expression provided in IEC Standard 60826:2003 for the design of overhead transmission lines (IEC 2003). However, it was noted that differences existed between the specified drag coefficient and that measured experimentally for the cross-arm section; this was attributed to the fact that the drag coefficient is defined solely on the solidity ratio in codes and standards. It was shown through further wind tunnel testing that the definition of the drag coefficient would benefit from the inclusion of additional characteristics, such as member spacing and non-uniform distribution of area, and recommendations for the evaluation the important parameters are made. This approach marks a significant departure from previous approaches to lattice section aerodynamics.

A prototype self-supported transmission tower was modeled in ANSYS®, and mean and fluctuating ABL winds were used to develop the capacity curve of the tower using the incremental dynamic analysis (IDA) and nonlinear static pushover (NSP) methods. Time histories of fluctuating wind were simulated using the ARMA algorithm (Samaras et al. 1985) and were applied to the tower for wind at three directions. The comparison of the capacity curves suggest that the NSP method can be used to approximate the more computationally-intense IDA method, and that the duration of the applied wind has little effect on the capacity curve for the time intervals considered.

Wind loads corresponding to synoptic (i.e., characterized by an atmospheric boundary layer wind profile), rectangular (i.e., uniform loading profile over the height of the tower) and downburst winds (i.e., critical profiles extracted from the numerical downburst simulations by Hangan et al. (2003)) were applied to the transmission tower model. The NSP method was used, which has previously been shown to provide a good approximation of the peak wind load effects (Banik et al. 2010) as well as in Chapter 3. The analysis of the tower considered both geometric and material nonlinearity through the use of a large deformation analysis and the use of bilinear elastoplastic material properties for the structural steel. The effects of geometric and material uncertainty were assessed using the simple Monte Carlo technique, and the coefficient of variation of the tower capacities were shown to be less than that associate with extreme wind loads effects. The NSP analysis provides the force-deformation relation of the tower, referred to as the capacity curve, which is defined based on the total reacting base shear force versus the displacement of the tip of the tower. It was shown that the capacity curves for a realistic range of downburst wind scenarios are approximately bound by those for the rectangular and ABL wind profiles on the upper and lower bounds, respectively, for the transverse and longitudinal wind directions (i.e., perpendicular and parallel to the conductors). It is worth noting that the transverse wind direction is often one of the dominant design cases for the tower design.

The wind loads on transmission towers vary greatly with wind direction, or the yaw angle, due to geometric characteristics. The capacity curves under downburst wind loading were assessed for many oblique wind directions, which resulted in estimates of the yield and maximum capacity for 11 wind directions. The downburst wind fields applied to the tower were selected based on the peak wind speeds experienced by the tower itself, and the analysis considers asymmetric loading on the conductor spans on either side of the tower due to varying distance from downburst location. Notably, it was shown that the tower had the lowest capacity for wind at approximately 45° to 50° for the downburst scenarios considered, although this may vary among tower geometries. The relationship of yield and maximum capacity to tip displacement was shown to be fairly smooth between yaw angles.

A similar series of analyses was performed for the ABL and rectangular wind profiles, which resulted in capacity curves for 11 oblique wind directions for each profile. The trajectories of the capacity curves were projected in plan view, and were shown not to intersect with one another. Based on this, it was proposed to describe the capacity of the tower using a capacity surface, which describes the force-deformation relation of the tower over a 90° sector of wind direction. Note that by mirroring this surface twice, the capacity surface for any wind direction (i.e., full 360°) is described. The capacity surface for a particular wind loading profile was developed through the 3-D interpolation of the capacity curves for the corresponding profile. It was shown, with the exception of very small downburst events, that the capacity surface for the tower under downburst loading is bound by those for the ABL and rectangular wind profiles. This makes the structural analysis for downburst wind load unnecessary if approximate results are needed, and largely simplifies the design checking task for downburst wind loads. Note that a conservative estimate of tower capacity is made if the load effects for an ABL wind profile are considered.

7.2 Conclusions

7.2.1 Experimental investigation of lattice section aerodynamics

Wind tunnel test data for a cross-arm section of a prototype transmission tower was used to assess the relationship of drag wind loads with yaw angle. The experimental data were compared to the calculations for the section based on ASCE Manual No. 74: Guidelines for Electrical Transmission Tower Structural Loading (ASCE 2010) and the International Electrotechnical Commission Standard No. 60826:2003 (IEC 2003). The following conclusions are drawn from the study:

1. Good agreement was found between the experimental data for the cross-arm section and the recommended values in the codes for the drag coefficient in the transverse direction. However, for the longitudinal direction (i.e., when the broad face of the cross-arm is fully exposed), the experimental values indicate a lower drag coefficient than suggested by both ASCE-74 and IEC-2003. This difference is expected to vary among cross-arm geometries, and is likely related to the non-uniform distribution of members.

Note that the recommended drag coefficients in ASCE-74 are not intended to be used for portions of towers such as cross-arms or bridges.

2. The procedure used to calculate the transverse wind load in ASCE-74 results in a lower transverse wind load for oblique wind directions than suggested by the wind tunnel data. This is due to the maximum transverse wind load occurring at a yaw angle of 0° in ASCE-74, while at a yaw angle of approximately 40° for the wind tunnel data. The shape of the experimental effective drag to yaw angle relationship is similar to that suggested by IEC-2003, although the magnitude of the measured drag is lower. This aspect is related to the difference in the drag coefficient for the longitudinal face noted in the above conclusion.

3. It is recommended to use an alternative method in place of the existing ASCE-74 method for the calculation of wind loads on lattice towers, which is especially pertinent to sections such as cross-arms or bridges. The following alternatives are suggested based on the comparison between wind tunnel data for the cross-arm section and the considered design procedures. Ideally, the same approach would be used for all components of the tower for consistency.

i) The IEC-2003 method of calculation of wind loads for lattice frames be reinstated in ASCE-74, at least for the calculation of wind loads on sections which have significantly different geometric and aerodynamic parameters, or aspect ratios, in the transverse and longitudinal directions. These types of sections include cross-arms and bridges.

ii) The calculation of the vector resultant wind load (as calculated from the existing expressions for transverse and longitudinal forces in ASCE-74) on each section is carried out prior to decomposition into transverse and longitudinal forces. This accounts for differences that may exist between the transverse and longitudinal planes in a correct fashion, while maintaining the load calculations currently specified in ASCE-74.

It was observed that the drag coefficient of a 2-D lattice frame varies with member spacing ratio and number of members; this reflects the dependence of the drag coefficient of the frame on a solidity ratio characterized by uniform member spacing. The assessment of the following aerodynamic characteristics of lattice frames would lead to an appropriate technique, and thus a better estimation of the drag coefficient:

1. Identification of the number of members at a defined member spacing ratio that is required to achieve a consistent drag coefficient. This results in a uniform solid area distribution and solidity ratio, and implies that the gross area should be calculated based on the dimensions of the uniform portion of a frame. This is opposed to the gross area defined by the outer boundaries of the frame, as is commonly used when considering geometries having non-uniform member spacing.

2. A relationship describing the difference between: i) the drag coefficient of a geometry based on a fully uniform member spacing (as suggested by point 1), and ii) the drag coefficient of a geometry meeting the criteria suggested by point 1, but having additional members spaced at varying ratios (i.e., percent of original spacing). Aerodynamic data would provide a measure of the difference in the drag based on i) and ii), which shows the impact of member spacing on the drag coefficient.

3. The results from point 2 could be used to adjust the definition of gross area used in the calculation of the solidity ratio to a more appropriate value than would be arrived at using the outer boundaries of the frame. For transmission tower cross-arm geometries, this would lower the considered gross-area, thereby increasing the solidity ratio. If the recommended values of the drag coefficient in codes were then to be used, the selected value would be more representative of a section having a uniform solid area distribution and solidity ratio.

While the experimental work presented here illustrates the issues associated with defining the drag coefficient solely on the solidity ratio, more aerodynamic data needs to be collected to arrive at a better technique for assigning a drag coefficient to geometries characterized by non-uniform distribution of solid area. The points described above may lead to such an improved technique.

7.2.2 Comparison of capacity assessment methods for a lattice transmission tower

Two popular nonlinear inelastic structural analysis for seismic loading, the IDA and NSP methods, are applied to wind loading on a 3-D model of a self-supported lattice transmission tower. The force-deformation relationship, or capacity curve, of the tower is obtained based on the IDA and NSP methods for three wind directions: the transverse and longitudinal directions, as well as for wind at 45° to the tower. It is concluded that the capacity curves from the NSP method can be used to approximate those developed by the more robust IDA, and capacity curves obtained using IDA are not significantly affected by the duration of fluctuating wind. More specifically:

1. For each wind direction considered, the capacity curves obtained by the NSP method are similar to those from the IDA, especially if those for the IDA are defined based on the maximum total reacting base shear force and the corresponding tip deflection. The agreement of curves was better for directions where the wind load on the wires is significant (i.e., transverse direction, wind at 45° to the tower).

2. No appreciable difference was observed for IDA capacity curves resulting from using wind histories of different durations (i.e., 1-minute, 5-minute). This suggests that the capacity curves based on a 1-minute fluctuating time history provide an appropriate description of the force-deformation relation of the structure.

3. If approximate results for the capacity curve of the tower are sought, it is therefore reasonable to use the capacity curve obtained using the NSP analysis. This greatly reduces the computing effort for analysis, which is important if uncertainty propagation analysis is of interest.

7.2.3 Capacity of a transmission tower under ABL and downburst wind loading

The nonlinear static pushover method is used to develop the capacity curve of the tower, which is represented using the total applied horizontal wind load (base shear) versus the displacement of the tip of the tower. The following conclusions are drawn from the study:

1. The capacities of the tower at incipient of yield and collapse depend on the wind loading profile. Generally, the capacities to sustain wind load for the ABL wind profile are lower than those for the rectangular wind profile. The uncertainty in the capacities due to material properties and geometric variables is not very significant; the coefficient of variation of the capacities is less than 10%, which is significantly smaller than that associated with the total wind load effect.

2. The wind load on the conductors and ground wire significantly affect the capacity curves in the transverse direction (as compared to the longitudinal direction). The critical wind speed for the considered tower is associated with the transverse direction. The capacity curves obtained for the ABL and rectangular wind profiles can be used as approximate lower and upper bounds, respectively, for the capacity curve for important downburst wind profiles.

3. Downbursts which are smaller in size result in the tower experiencing yield at a higher base shear, as well as less deformation with increasing wind speed. Downbursts which are greater in size initiate yield at a lower horizontal wind load, but allow for more deformation in the post-yield range prior to collapse. The characteristics of the capacity curve for the ABL wind load distribution resembles that for a downburst having a jet diameter between 1000 m and 1500 m in terms of yield and maximum capacity. As the size of the downburst increases, the capacity curve becomes steeper in both the elastic and inelastic range.

4. Based on the above observations, it is recommended that the capacity curve estimated under the rectangular wind profile can be used as a proxy for the capacity curve under downburst wind if the downburst size is small, and that the capacity curve estimated under the ABL wind profile can be used as a proxy for the capacity curve under downburst wind if the downburst size is large. The consideration of these conditions in practice simplifies the performance assessment of towers under downburst wind loading, as well as provides advice on the necessary capacity for towers to resist downburst winds in the design process.

7.2.4 Effect of relative orientation on the capacity of a transmission tower under downburst loading

The capacity curve of a self-supported lattice transmission tower has been obtained for three downburst scenarios at many orientations relative to the tower using the NSP method. The tower is represented as a 3-D numerical model, and both inelastic material and geometric properties are considered in the analysis. The resulting capacity curves are presented as the force-deformation relationship between the total applied horizontal wind load and the displacement of the tip of the tower. The capacity curves are obtained for three downburst sizes and their differences are discussed. The following conclusions are drawn from the study:

1. The capacity curve of the tower is dependent on the shape of the wind profile with which it is loaded. The capacity curves obtained for the downburst scenario characterized by a smaller D_{jet} result in higher yield capacity and less post-yield deformation. The shape of the wind profile has a greater effect on the capacity curve for wind directions where the wires are loaded, which is due to the load concentration in the upper portion of the tower.

2. The shape of the capacity curves for wind directions at which the wires are significantly loaded (i.e., greater than 30°) are quite similar in shape for each downburst scenario. The distribution of applied loads for these directions contributes to a greater amount of post-yield deformation of the tower compared to wind directions where the wires are not loaded.

3. The capacity curves for the tower vary with wind direction, which is primarily due to the asymmetric loading of transmission structures (i.e., different areas in the transverse and longitudinal directions, contribution of wind loading on the wires). For this particular tower design, the lowest yield capacity for each downburst scenario is observed in the 45° to 50° range of wind direction.

4. Multiple downburst sizes (D_{jet}) were investigated for the transverse and longitudinal directions. It is shown that as the downburst size decreases, the horizontal loads tend to

be concentrated at the mid-height of the tower rather than the upper portion. Thus, for an equal horizontal wind load, the stress in the structural members decreases with D_{jet}.

7.2.5 Effect of wind direction on the response and capacity surface of a transmission tower

The NSP method is used to estimate the nonlinear inelastic response of a self-supported transmission tower under traditional ABL winds and rectangular (uniform) winds at various wind directions. The transmission tower and lines are represented by a 3-D numerical model, and wind loads are applied based on the geometric and aerodynamic parameters specified by CSA-2010. Both geometric and material nonlinearity were accounted for in the analysis. The results were used to develop capacity curves for the tower under different wind loading profiles: the ABL wind profile, the rectangular wind profile, and the wind profile resulting from three downburst scenarios. The curves are also used to form the capacity surface of the tower under wind loading. The following conclusions are drawn from the study:

1. The capacity curve of the tower is dependent on the loading profile applied and wind direction. For any given wind direction, the capacity curves for a scenario downburst are approximately bound by those obtained for the ABL and rectangular wind profiles. The yield and maximum capacities of the tower for the ABL wind profile are lower than those for the rectangular, or uniform, wind profile. The ratio of yield capacity to maximum capacity for any given wind direction is insensitive to the considered wind profile.

2. The yield capacity of the tower is the lowest for a wind direction of 50° for both the ABL and rectangular wind profiles. However, the critical wind speed initiating yield occurs for the fully transverse wind direction (wind at 0°) for both wind profiles. The wind speed initiating yield for the wind direction within the sector 0° through 50° is within 3% of the critical wind speed.

3. The projection of the resultant tip displacement on the horizontal plan corresponding to the capacity curves for each wind direction do not intersect, and can therefore be used to form the capacity surface for the tower under wind loading. For a given resultant tip displacement, the total applied wind force for the ABL wind profile is lower than that for

the rectangular wind profile; the force for the scenario downburst events is approximately bound by those obtained for the ABL and rectangular wind profiles. This makes the structural analysis for downburst wind load unnecessary if approximate results are desired; it largely simplifies the task for design checking of new towers and the evaluation of existing towers under downburst wind loads. More importantly, a conservative approximation is made if the capacity curve, or surface, for the ABL wind profile is used.

7.3 Recommendations for future work

The following recommendations are made for future work which would complement and extend the results presented in this thesis:

1. The data from wind tunnel tests performed on a cross-arm section show that the relationship of transverse and longitudinal wind loads for oblique wind directions may not be accurately predicted by current wind loading expressions. There is very little wind tunnel data available in the literature which focusses on the aerodynamics of cross-arm sections. For some tower designs, the wind loading on these portions of the tower may significantly contribute to the overall loads on the tower, and due to their location at the top of the tower, the stresses in the members near the base. Additional wind tunnel testing for a range of cross-arm geometries is recommended in order to develop a better description of the wind loads on these types of sections.

2. It was suggested that the drag coefficient for sections with non-uniform distribution of solid area is not well predicted through the use of solidity ratio alone. Additional parameters which would contribute to a better description of the drag coefficient for these types of sections are identified as follows: identification of the bounds of the section which results in consistent aerodynamic behavior; the member spacing ratio for which the bounds of uniform aerodynamic behavior are defined; and an adjustment of the method used for the calculation of the effective solidity ratio of the section based on the former two findings. The ability to incorporate these changes into existing wind loading codes remains to be seen.

3. The IDA capacity curves presented in Chapter 3 were developed considering only vertical coherence in the fluctuating wind; that is, the spanwise loading was assumed to be fully correlated. For structures such as transmission lines, the wind load on the conductors provides a significant contribution to the overall wind loads. The numerical values of yield and maximum capacity are likely to represent a lower bound compared to typical synoptic wind loading conditions, and will benefit from the lack of spanwise correlation (i.e., along the length of the conductors) in the dynamic wind loading. While a fully coherent description of wind load is conservative, the extent of the conservatism present in the capacity estimates should be quantified. Note also that this component would ideally be assessed for towers of different heights and wind spans, as coherence is a spatially-varying parameter.

4. Using the NSP procedure it was shown that the yield and maximum capacities of the tower vary with wind direction. The maximum capacity of a tower (i.e., incipient of collapse), and its accompanying uncertainty, is required for the reliability assessment of both a point structure and distributed systems. The results presented is this thesis, along with an appropriate hazard analysis (i.e., Hong et al. 2013), could be used for the reliability assessment of individual towers and transmission line systems. Depending on the characteristics of the hazard analysis, the wind direction resulting in the lowest tower capacity could be used. The reliability assessment for a point structure could also include the joint probability distribution of wind speed and direction for a more accurate description.

5. While the results for this particular tower indicate that the application of loads based on ABL winds result in a conservative estimate of the yield and maximum tower capacities, additional tower designs should be investigated to ensure that there is a trend to this observation. Towers with multiple cross-arms, smaller conductor spans between towers, and towers of varying height would ideally be considered in future analysis. The ratio of wind load on the tower to that on the conductor is important for structural loading and will vary depending on tower configuration.

7.4 References

Banik, S.S., Hong, H.P. and Kopp, G.A. (2010). "Assessment of capacity curves for transmission line towers under wind loading." *Wind Struct*., 13(1), 1-20.

Hangan, H., Roberts, D., Xu, Z. and Kim, J.-D. (2003). "Downburst simulations. Experimental and numerical challenges." *Proc. of the 11th International Conference on Wind Engineering*, Lubbock, TX, USA.

Hong, H.P., Mara, T.G., Morris, R.J., Li, S.H. and Ye, W. (2013). "Basis for recommending an update of wind velocity pressures in Canadian design codes." *Boundary Layer Wind Tunnel Research Report No. BLWT-1-2013*. (A shortened version of this was also submitted to the Canadian Journal of Civil Engineering).

International Electrotechnical Commission (IEC) (2003). "Design criteria of overhead transmission lines." CEI/IEC No. 60826:2003.

Copyright Permissions

Permission to include the following articles has been requested and granted:

Mara, T.G. (2013). "Influence of solid area distribution on the drag of a 2-D lattice frame." Journal of Engineering Mechanics, 10.1061/(ASCE)EM.1943-7889.0000681 (Jun. 7, 2013). http://dx.doi.org/10.1061/(ASCE)EM.1943-7889.0000681

Mr. T.G. Mara, M.ASCE, P.Eng.
Department of Civil & Environmental Engineering
University of Western Ontario
London, ON
Canada
N6A 5B9

June 13, 2013

ASCE
Journals Department
Permissions

To whom it may concern:

I am a University of Western Ontario graduate student completing my Doctoral thesis entitled "Capacity assessment of a transmission tower under wind loading". My thesis will be available in full-text on the internet for reference, study and/or copy. Except in situation where a thesis is under embargo or restriction, the electronic version will be accessible through the Western Libraries web pages, the Library's web catalogue, and also through web search engines. I will also be granting Library and Archives Canada and ProQuest/UMI a non-exclusive license to reproduce, load, distribute, or sell single copies of my thesis by any means and in any form or format. These rights will in no way restrict republication of the materials in any other form by you or others authorized by you.

I would like permission to allow inclusion of the following material in my thesis:
Mara, T. (2013). (2013). "Influence of Solid Area Distribution on the Drag of a 2-D Lattice Frame." *J. Eng. Mech.*, 10.1061/(ASCE)EM.1943-7889.0000681 (Jun. 7, 2013).

The article is available in Preview Manuscript format only, and I do not have access to the Rightslink option available for articles which have appeared in print. The material will be attributed through a citation.

Please confirm in writing or by email that these arrangements meeting with your approval.

Yours sincerely

Thomas G. Mara, M.ASCE, P.Eng.

Dear Thomas Mara:

Thank you for your request. Permission is granted for you to reuse Mara, T. (2013). (2013). "Influence of Solid Area Distribution on the Drag of a 2-D Lattice Frame." *J. Eng. Mech.*, 10.1061/(ASCE)EM.1943-7889.0000681 (Jun. 7, 2013) in your doctoral dissertation under the condition that the paper makes up less than 25% of your new work.

A full credit line must be added to the material being reprinted. For reuse in non-ASCE publications, add the words "With permission from ASCE" to your source citation. For Intranet posting, add the following additional notice: "This material may be downloaded for personal use only. Any other use requires prior permission of the American Society of Civil Engineers.

Regards,

Joann Fogleson
American Society of Civil Engineers
1801 Alexander Bell Drive
Reston, VA 20191
(703) 295-6278-FAX

PERMISSIONS@asce.org

Curriculum Vitae

Name:
Thomas Goodwin Mara
P.Eng., LEED Green Associate

Post-secondary Education and Degrees:

The University of Western Ontario
London, Ontario, Canada
2009-2013 Ph.D.

The University of Western Ontario
London, Ontario, Canada
2005-2007 M.E.Sc.

The University of Western Ontario
London, Ontario, Canada
2001-2005 B.E.Sc. (with distinction)

Honours and Awards:

Postgraduate Scholarship
National Sciences and Engineering Research Council of Canada (NSERC)
2011-2013

1st Place, Graduate Student Civil Seminar Competition (2012)
Department of Civil and Environmental Engineering
University of Western Ontario

Graduate Award in Structural Engineering (2011)
Department of Civil and Environmental Engineering
University of Western Ontario

Graduate Thesis Research Award (2009, 2011, 2012)
University of Western Ontario

Related Work Experience:

Co-supervisor, Master of Engineering (M.Eng.) Project
The University of Western Ontario
2012-2013

Instructor
CEE 4490 – Dynamics of Structures
The University of Western Ontario
2010

Project Manager/Engineer
Boundary Layer Wind Tunnel Laboratory
University of Western Ontario
2007-2010

Teaching Assistant
The University of Western Ontario
2005-2007, 2009-2013

Engineering Research Assistant
Boundary Layer Wind Tunnel Laboratory
University of Western Ontario
May – August 2005

Technical Committees:

ASCE Task Committee, Manual of Practice No. 74: Guidelines for Electrical Transmission Line Structural Loading. Co-chair, Chapter 2: Weather-related loads.

Publications:

Peer-reviewed Journal Articles

Mara, T.G. (2013). Influence of solid area distribution on the drag of a 2-D lattice frame. Journal of Engineering Mechanics.

Hong, H.P., Li, S.H. and **Mara, T.G.** (2013). Performance of the generalized least-squares method for the Gumbel distribution and its application to annual maximum wind speeds. Journal of Wind Engineering and Industrial Aerodynamics, 119, 121-132.

Mara, T.G. (2010). Effects of a construction tower crane on the wind loading of a high-rise building. Journal of Structural Engineering, 136(11), 1453-1460.

Mara, T.G., Galsworthy, J.K. and Savory, E. (2010). Assessment of vertical wind loads on lattice framework with application to thunderstorm winds. Wind and Structures, 13(5), 413-431.

Conference Papers (T.G. Mara is the presenting author unless noted by *)

Mara, T.G. and Lombardo, F.T. (2013). Toward a coherent US-Canada extreme wind climate. *12th Americas Conference on Wind Engineering*, Seattle, WA.

Mara, T.G., Terry, B.K., Ho, T.C.E. and Isyumov, N. (2013). Influence of aerodynamic interference on the performance of tall buildings. *12th Americas Conference on Wind Engineering*, Seattle, WA.

Mara, T.G. and Hong, H.P. (2013). Capacity of a transmission tower under downburst wind loading. *2013 CSCE Annual Conference*, Montréal, QC.

Mara, T.G. and Gatey, D.A. (2013). The role of manual observation in the evaluation of Canadian wind speed data. *2013 CSCE Annual Conference*, Montréal, QC.

Mara, T.G., Hong, H.P. and Morris, R.J. (2013). Effect of corrections to historical wind records on estimated extreme wind speeds for standard conditions. *2013 CSCE Annual Conference*, Montréal, QC.

Mara, T.G. and Vickery, B.J. (2013). Wind effects on four steel stacks in square arrangement. *2013 ASCE Structures Congress*, Pittsburgh, PA.

Mara, T.G. (2012). Influence of solid area distribution on the drag of a 2-D lattice frame. *3rd American Association for Wind Engineering Workshop*, Hyannis, MA.

Mara, T.G., Ho, T.C.E. and Isyumov, N. (2012). Interference and influence of nearby buildings: A discussion of the design approach. *2012 ASCE Structures Congress*, Chicago, IL.

Mara, T.G. and Galsworthy, J.K. (2011). Comparison of model-scale and full-scale wind tunnel test results for a typical 3-dimensional lattice frame. *13th International Conference on Wind Engineering*, Amsterdam, NL.

Mara, T.G. and Ho, T.C.E. (2011). Design loads for transmission towers under skewed wind loading. *2011 ASCE Structures Congress*, Las Vegas, NV.

Mara, T.G. and Case, P.C. (2010). The effects of incremental corner modifications on a 200m tall building. *2010 ASCE Structures Congress*, Orlando, FL.

Isyumov, N., Case, P.*, Hasan, A., Tait, M., Morrish, D., Farquhar, S. and **Mara, T.** (2010). Monitoring of tall buildings to assist the design of supplementary damping systems. *2010 ASCE Structures Congress*, Orlando, FL.

Selected Engineering Research Reports

Hong, H.P., **Mara, T.G.**, Morris, R.J., Li, S.H. and Ye, W. (2013). Basis for recommending an update of wind velocity pressures in the 2010 National Building Code of Canada. *Boundary Layer Wind Tunnel Research Report No. BLWT-1-2013*.

Mara, T.G. (2009). A study of wind effects for a 200m tall square building with incremental corner chamfer configurations. *Boundary Layer Wind Tunnel Research Report No. BLWT-1-2009*.

Mara, T.G. (2009). A study of the mean wind loads on a 200m tall building with adjacent tower crane. *Boundary Layer Wind Tunnel Research Report No. BLWT-3-2009*.

Selected Engineering Reports (Commercial)

Hong, H.P, Ho, T.C.E. **Mara, T.G.**, He, W.X. and Lee, C.-S. (2011). Weather hazard and reliability analysis for Manitoba Hydro proposed Bipole III. *Boundary Layer Wind Tunnel Research Report No. BLWT-SS24-2011*.

Mara, T.G. and Vickery, B.J. (2009). A study of wind effects for Steel Stacks Phase II at Astoria, New York, USA. *Boundary Layer Wind Tunnel Research Report No. BLWT-SS6-2009*.

Mara, T.G., Case, P.C., Morrish, D.P. and Vickery, B.J. (2009). A study of tuned liquid column dampers for One Madison Park, New York City, NY. *Boundary Layer Wind Tunnel Research Report No. BLWT-SS13-2009*.

Mara, T.G., Edey, R.T., Ho, T.C.E. and Isyumov, N. (2009). Analytical study of the wind effects for Trump Tower Spire, Toronto, Ontario. *Boundary Layer Wind Tunnel Research Report No. BLWT-SS32-2009*.

Mara, T.G., Inculet, D. and Isyumov, N. (2008). A study of wind effects for First Canadian Place, Toronto, Ontario, Canada. *Boundary Layer Wind Tunnel Research Report No. BLWT-SS5-2008*.

Mara, T.G., Edey, R.T. and Ho, T.C.E. (2008). A study of the wind effects for King Abdul Aziz Endowment Hotel Tower, Mecca, Saudi Arabia. *Boundary Layer Wind Tunnel Research Report No. BLWT-SS19-2008*.

Mara, T.G. and King, J.P.C. (2008). A study of the wind effects for Anna Maria Bridge design alternatives, Anna Maria Island, FL. *Boundary Layer Wind Tunnel Research Report No. BLWT-SS74-2008*.

Online Publications (Google Scholar) Link:
http://scholar.google.ca/citations?user=tB7Zr6QAAAAJ&hl=en&oi=ao